EINDHOVEN UNIVERSITY OF TECHNOLOGY

A numerical study on the effect of anisotropy and heterogeneity on hydraulic fractures

Citation for published version (APA):
Valliappan, V. (2019). *A numerical study on the effect of anisotropy and heterogeneity on hydraulic fractures*. [Phd Thesis 1 (Research TU/e / Graduation TU/e), Mechanical Engineering]. Technische Universiteit Eindhoven.

Document status and date:
Published: 20/11/2019

Document Version:
Publisher's PDF, also known as Version of Record (includes final page, issue and volume numbers)

Please check the document version of this publication:

• A submitted manuscript is the version of the article upon submission and before peer-review. There can be important differences between the submitted version and the official published version of record. People interested in the research are advised to contact the author for the final version of the publication, or visit the DOI to the publisher's website.
• The final author version and the galley proof are versions of the publication after peer review.
• The final published version features the final layout of the paper including the volume, issue and page numbers.

Link to publication

General rights
Copyright and moral rights for the publications made accessible in the public portal are retained by the authors and/or other copyright owners and it is a condition of accessing publications that users recognise and abide by the legal requirements associated with these rights.

• Users may download and print one copy of any publication from the public portal for the purpose of private study or research.
• You may not further distribute the material or use it for any profit-making activity or commercial gain
• You may freely distribute the URL identifying the publication in the public portal.

If the publication is distributed under the terms of Article 25fa of the Dutch Copyright Act, indicated by the "Taverne" license above, please follow below link for the End User Agreement:

www.tue.nl/taverne

Take down policy
If you believe that this document breaches copyright please contact us at:

openaccess@tue.nl

providing details and we will investigate your claim.

Download date: 08. Feb. 2024

A numerical study on the effect of anisotropy and heterogeneity on hydraulic fractures

Valliappan Valliappan

This work is part of the Industrial Partnership Programme (IPP) 'Computational sciences for energy research' of the former Foundation for Fundamental Research on Matter (FOM), now the Netherlands Organisation for Scientific Research (NWO). This research programme is co-financed by Shell Global Solutions International B.V.

Copyright © 2019 by Valliappan Valliappan. All Rights Reserved.

Printed by Ipskamp Drukkers.

A catalogue record is available from the Eindhoven University of Technology Library.

ISBN 978-90-386-4926-9

Keywords: Hydraulic fracturing, fracking, Anisotropy, Heterogeniety, Extended finite element method, Leak-off

A numerical study on the effect of anisotropy and heterogeneity on hydraulic fractures

PROEFSCHRIFT

ter verkrijging van de graad van doctor aan de Technische Universiteit Eindhoven, op gezag van de rector magnificus prof.dr.ir. F.P.T.Baaijens, voor een commissie aangewezen door het College voor Promoties, in het openbaar te verdedigen op woensdag 20 november 2019 om 11:00 uur

door

Valliappan Valliappan

geboren te Madurai, India

Dit proefschrift is goedgekeurd door de promotoren en de samenstelling van de promotiecommissie is als volgt:

voorzitter:	prof.dr.ir. L.P.H. de Goey
1e promotor:	prof.dr.ir. D.M.J. Smeulders
co-promotor:	dr.ir. J.J.C. Remmers
	dr.ir. A. Barnhoorn
externe leden:	prof.dr.ir. G. Bertotti (Technische Universiteit Delft)
	prof.dr. A. Mikelic (Université Claude Bernard Lyon)
	prof.dr.ir. C.J. van Duijn
	dr.ir. M. Hettema (Energie Beheer Nederland B.V.)

Het onderzoek of ontwerp dat in dit proefschrift wordt beschreven is uitgevoerd in overeenstemming met de TU/e Gedragscode Wetenschapsbeoefening.

To my beloved mother. . .

Summary

Hydraulic fracturing is a process that is used to enhance the permeability in reservoirs by inducing fractures with the help of viscous fluids which are injected at high pressures. A better understanding of the hydraulic fracture growth phenomena will enhance the productivity in these reservoirs and also reduce the environmental footprint as less fractures can be created in a much more efficient way. Hence in this thesis a numerical model was developed to investigate the influence of various parameters such as rock material properties, injection fluid, injection flow rates, in-situ stresses on the hydraulic fracture growth.

Several existing models focus on modelling of hydraulic fracturing in near impermeable rocks, such as shales, which have negligible leak-off from the fracture into the formation. But hydraulic fracturing is also used in permeable rocks, such as sandstones and limestones, for enhanced oil recovery and geothermal heat extraction. Hence a Modified Enhanced Local Pressure (MELP) model was developed with an improved leak-off model which can be used for both near impermeable as well as permeable rocks. The MELP model makes use of Biot's theory of poro-elasticity and Darcy's law for modelling the solid grain deformation and the pore pressure in the formation. An additional degree of freedom is used for modelling the pressure in the fracture. The MELP model captures the leak-off accurately with the help of a 1-D Terzaghi consolidation equation and also fully couples the pore pressure in the formation with the leak-off. The model captures the high pressure gradients, in near impermeable rocks, without the need for a fine mesh close to the fracture while the pressure transition is much smoother in permeable rocks, where leak-off becomes a vital parameter. Using the MELP model, the growth of a fracture network is demonstrated in which the leak-off from the outer fractures acts as a shield against leak-off for a centre fracture.

Most sedimentary rock formations, particularly shales, are highly anisotropic in nature. The anisotropy is due to the orientation of grains along a specific di-

rection causing the properties along the grain orientation direction to be vastly different from the properties perpendicular to the grain orientation direction. To take this into account, we extend the model to include directional dependence of all the rock properties, both elastic and flow related. A combination of the Tsai–Hill failure criterion and Camacho–Ortiz propagation criterion is proposed to determine the fracture propagation and its orientation. Anisotropy in Young's modulus is observed to promote fracture growth perpendicular to the grain direction whereas ultimate tensile strength anisotropy promotes fracture growth parallel to the grain direction. The effect of these material anisotropies were also found to be varying with the angle between the initial fracture orientation and the grain orientation direction. Anisotropy in in-situ stress causes the fracture to propagate parallel to the maximum stress direction. Different regimes of fracture propagation were identified by combining all these anisotropic parameters in varying degrees.

Heterogeneities in rocks can either be of discrete nature, due to the presence of inclusions which are formed due to the precipitation of minerals at specific locations, or of a layered nature due to the deposition of different minerals over different times. Inclusions softer than the surrounding rock materials act as obstacles for the fracture path and the fractures are found to deflect significantly to avoid them. While harder inclusions tend to deflect the fractures towards them. The layered nature of rocks causes a significant change in the stress state of each layer which can cause the hydraulic fractures to cross, kink, turn or arrest when propagating from one layer to another. The fracture behaviour in a layered rock depends upon the contrast in material properties between the layers (Young's modulus, ultimate tensile strength) as well as reservoir level properties such as layer thickness, bedding plane orientation and in-situ stresses.

In this thesis, novel numerical techniques have been developed to further the understanding of the hydraulic fracturing phenomenon and the factors influencing them. The developed model can be used for fracture propagation in permeable as well as near impermeable rocks. The anisotropic and heterogeneous nature of rock formations have significant impact on the fracture propagation direction.

Contents

Abstract **vii**

1 Introduction **1**
1.1 Hydraulic fracturing 3
1.2 Research Objectives 4
1.3 Outline of the thesis 6

2 Parametric study on hydraulic fracturing **9**
2.1 Hydraulic fracture models 10
2.2 KGD Model 11
2.3 Test example 11
2.4 Control Parameters 13
2.4.1 Fluid injection rates 13
2.4.2 Fracture fluid viscosity 14
2.5 Material Properties 16
2.5.1 Young's Modulus 16
2.5.2 Poisson's Ratio 17
2.5.3 Ultimate tensile strength 18
2.5.4 Porosity 19
2.5.5 Permeability 20
2.6 Summary 22

3 Modified Enhanced Local Pressure (MELP) model **23**
3.1 Introduction 24
3.2 Mathematical Model 25
3.2.1 Kinematics 25
3.2.2 Poromechanics model 27
3.2.3 Cohesive Zone Model 28
3.2.4 Leak-off model 29

3.3 Governing Equations . . . 31
3.3.1 Momentum Balance . . . 31
3.3.2 Mass Balance . . . 31
3.3.3 Mass Balance in the fracture . . . 31
3.3.4 Weak Form . . . 32
3.4 Solution Methodology . . . 34
3.4.1 Discretisation . . . 34
3.4.2 Solution . . . 36
3.5 Numerical Examples . . . 36
3.5.1 Consolidation Problem . . . 37
3.5.2 Single hydraulic fracture . . . 40
3.5.3 Cluster of hydraulic fractures . . . 43
3.6 Conclusion . . . 46

4 Effect of anisotropy on hydraulic fractures 47
4.1 Introduction . . . 48
4.2 Mathematical formulation . . . 49
4.3 Implementation . . . 50
4.3.1 Discretisation . . . 50
4.3.2 Solution . . . 51
4.3.3 Propagation . . . 51
4.4 Anisotropic parameters . . . 52
4.4.1 Constitutive relation . . . 52
4.4.2 Ultimate tensile strength . . . 53
4.4.3 Poro-elastic coefficients . . . 55
4.4.4 Permeability . . . 56
4.5 Results . . . 56
4.5.1 Validation . . . 56
4.5.2 Vertical hydraulic fracture problem . . . 59
4.5.3 Parametric anisotropy . . . 60
4.5.4 Degree of material anisotropy . . . 63
4.5.5 Angle of orientation . . . 65
4.5.6 Lithostatic stresses . . . 67
4.6 Conclusion . . . 70

5 Hydraulic fracture propagation in heterogeneous reservoirs 73
5.1 Introduction . . . 74
5.2 MELP Model . . . 75
5.2.1 Physical model . . . 75
5.2.2 Numerical model . . . 76
5.2.3 Propagation . . . 77
5.3 Numerical Example . . . 78
5.3.1 Influence of material properties . . . 80

5.3.2 Influence of reservoir properties 83
5.3.3 Effect of fracture initiation location 87
5.3.4 Effect of a thin layered formation 89
5.4 Comparison with experiments and field observations 90
5.5 Effect of Inclusions 92
5.6 Multi-stage Hydraulic fracturing 94
5.7 Conclusion 96

6 Conclusions 99
6.1 Conclusions 99
6.2 Outlook 101

A Expression for matrices in the MELP solution 103

B Final fracture orientation angles for varying anisotropy ratios 107

Bibliography 117

Acknowledgements 131

Curriculum Vitae 133

Chapter 1

Introduction

Ever since the advancement of industrial and technological sectors, the need for energy is growing rapidly across the world. The global energy consumption is projected to grow by 28% over the next 20 years, according to U.S. Energy Information Administration (2017). In order to meet this growing demand, every source of energy needs to be explored. The expected growth rate of various sources of energy, as shown in Figure 1.1, predicts that close to three-quarters of the global energy demand would still be met by the fossil fuels in 2040 under the current policy scenario (International Energy Agency, 2018b).

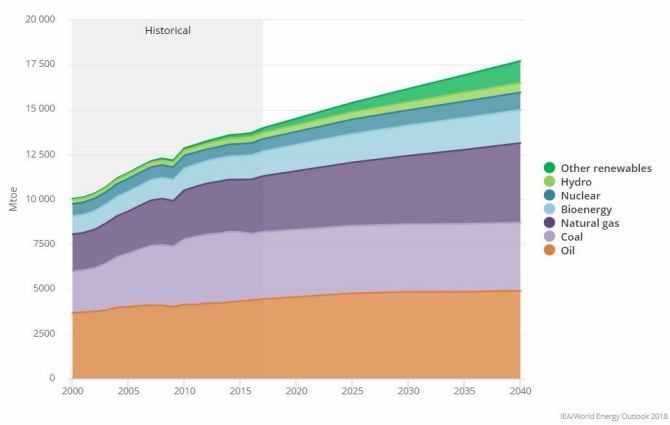

Figure 1.1: Total world energy demand supplied by various sources of energy. Reproduced from the International Energy Agency (2018b)

The U.S. Energy Information Administration (2017) in its international energy outlook predicts that the majority of this rise in energy consumption (around 60%), to come from countries that are not in the Organization for Economic Cooperation and Development (OECD). These countries primarily use coal as a source to meet their electricity demands which is the single high-

est contributor in terms of global CO_2 emissions (International Energy Agency, 2018a). Hence a shift from coal-based energy to less polluting natural gas-based, would already have significant benefits to the environment.

With time, the extraction of oil and gas from reservoirs has become increasingly difficult as most of the easily accessible reserves have already been explored. Hence there is a need for exploring new reserves of oil and gas present in unconventional reservoirs. Reservoirs in which hydrocarbons are trapped in rock formations with very low permeability are referred to as unconventional reservoirs. The huge amount of shale gas and tight oil reserves trapped in these unconventional reservoirs in the various regions around the world is shown in Figure 1.2.

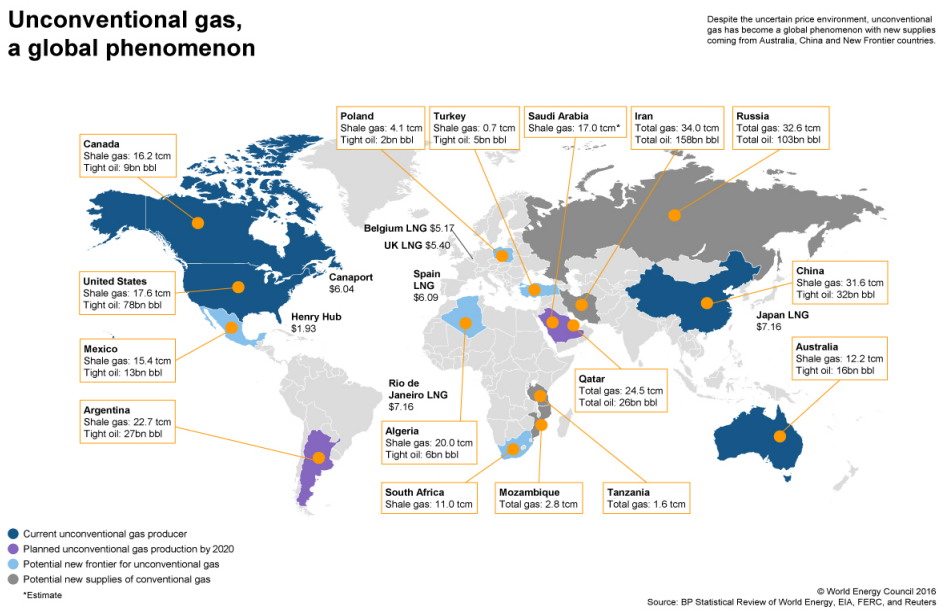

Figure 1.2: World reserves of shale oil and tight gas in unconventional reservoirs. Reproduced from World Energy Council (2016)

To meet the industrial heat demand in a sustainable way it is necessary to extract geothermal energy from greater depths than has been done so far. For industrial application and the production of electricity, temperatures of 150°C and more are essential for which we require Ultra Deep Geothermal (UDG) reservoirs. At these depths there is no natural permeability, so the connectivity has to be artificially created by fracturing.

1.1 Hydraulic fracturing

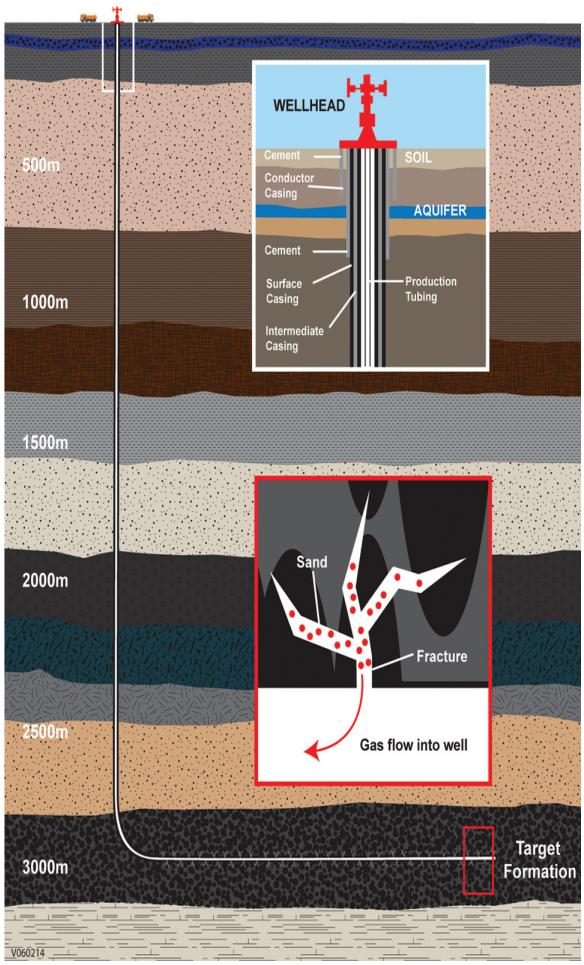

Figure 1.3: A schematic of the hydraulic fracturing principle in a horizontally drilled well. A viscous fluid at high pressure is injected into the well to create fractures. The opened fractures are held in place by sand particles after the release of pressure.(Department of mines, industry regulation and safety, Government of Western Australia, 2018)

Although unconventional reservoirs contain a significant amount of oil and gas, they have very poor production rates due to their very low permeability. They require some form of stimulation to enable economical recovery rates. One such stimulation technique is hydraulic fracturing. Although the process of hydraulic fracturing has been well known since the 1950's, it has gained traction in recent decades due to several technological advancements (King et al., 2010) such as horizontal drilling, multi-stage fracturing, slick water fracking

fluids. The capability to drill horizontal wells has enabled an efficient way to recover the oil and gas trapped in a single hydrocarbon-rich layer.

The hydraulic fracturing process can be described as follows (Hubbert and Willis, 1972). The horizontally drilled wells are surrounded by several layers of casing as shown in Figure 1.3. These casings are perforated at specific locations. Then a viscous fluid is injected into the well at high pressures. When the fluid pressure overcomes a critical value (dependent on the depth of the formation and rock strength), a fracture is initiated and starts to propagate. The fracture forms highly permeable pathway through which the oil and gas can be extracted. After a certain time, the injection pressure is reduced to allow the flow of oil and gas but this also results in the closing of the previously opened fractures. After pressure release, the fractures are kept open with the help of proppants that are granular particles like sand which are mixed with the injection fluid (Economides and Nolte, 2000).

The hydraulic fracturing process has also been successfully employed for enhancing the productivity in conventional reservoirs (Rahim et al., 2012) during tertiary treatment. The same stimulation technique can also be used for extracting geothermal energy (Legarth et al., 2005) as shown in Figure 1.4. Currently the production of geothermal energy majorly relies on a unique set of conditions where there is hot rock formation which is also permeable with the presence of large number of pre-existing fractures which need to be highly interconnected. Hydraulic fractures would help in untapping new resources of geothermal energy and enhancing the productivity of the current reservoirs by creating new fractures which would increase the interconnectivity of fractures and result in better transport of the injected cold fluid through the subsurface where it is heated up by the hot dry rocks in Enhanced Geothermal Systems (EGS) (Brown et al., 2012). Finally, hydraulic fracturing can also be helpful in carbon sequestration where carbon dioxide is stored in these tight rocks with low permeability.

1.2 Research Objectives

The major objective of this thesis is to have a better understanding of the hydraulic fracture growth phenomena which helps in enhancing the productivity and also reduce the environmental footprint as less fractures can be created in a more efficient way.

One of the major environmental concerns regarding hydraulic fracturing is that the fractures propagate through several layers to reach the aquifer layers which would result in groundwater contamination (Taherdangkoo et al., 2017). From an economic perspective, the concern is that the fractures tend to abruptly stop at several bedding layer interfaces (Simonson et al., 1978; Fisher et al., 2012). In order to address these concerns, an accurate prediction

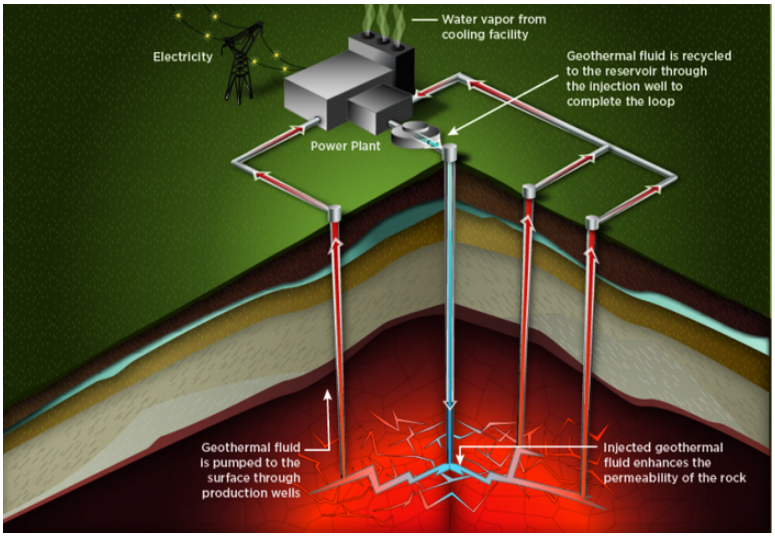

Figure 1.4: A schematic describing the energy extraction process in an Enhanced geothermal reservoir.(National Renewable Energy Laboratory, U.S. Department of Energy, 2018)

of the fracture growth in the vertical direction is important for which the proposed hydraulic fracture models need to take into account the variation in rock properties.

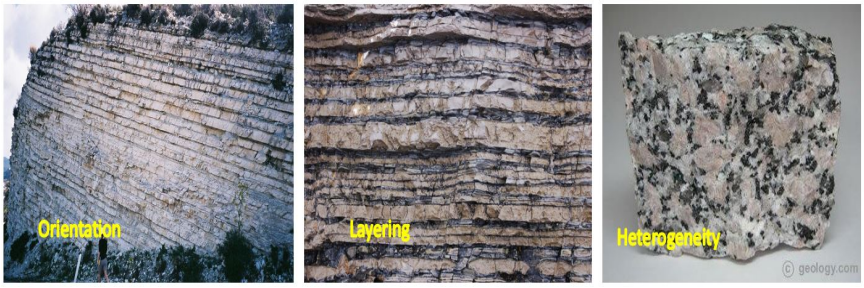

Figure 1.5: Sedimentary rocks showing anisotropy and heterogeneity characteristics. (Left) Carbonate rocks from Cyprus which show the orientation along a particular direction. The centre figure shows the layering behaviour in rocks. While the figure on the right shows the heterogeneity present in the granite rocks. (Geology.com, 2018)

Many existing models assume the rock formation to be isotropic and homogeneous in nature. But in reality most formations are not as ideal, as observed in Figure 1.5. The sedimentary rock formations are a consequence of deposition of minerals over time which results in a layered nature of the formations as different minerals are deposited at different times through the history. Also,

in many cases the formations are not composed of one unique mineral, but several inclusions are found which results in a heterogeneous nature. In several formations, the grains are oriented along a specific direction due to weathering , erosion which leads to the formation being anisotropic in nature. Hence a realistic prediction of hydraulic fracture characteristics is only possible when the anisotropy, heterogeneity and the layered nature of rock formations present in the reservoir is taken into account.

It is also imperative to minimize water consumption. First to enable fracturing in arid regions where water is scarce, but also to reduce the amount of waste water after a fracturing job (Burden et al., 2016).

Another major concern is potential seismic activity induced in the region during and after the fracturing operation (Bao and Eaton, 2016). This risk can be mitigated by better understanding of the effect of fracturing on the surrounding rock formation. One important factor affecting the surrounding formation is the leak-off of fluid from the fracture to the formation. If there is an excess fluid leak-off, it would result in surrounding formation matrix damage (Penny et al., 1985). Hence the modelling of the fluid leak-off phenomenon is an important factor for efficient economical operation of the wells as well as to prevent damage in the surrounding formation.

1.3 Outline of the thesis

The thesis is structured in the following manner:

- In Chapter 2, a background of the evolution of hydraulic fracture models is provided. The influence of various parameters (rock material properties, injection fluid viscosity, flow rate) on hydraulic fracture growth is investigated.

- Chapter 3 proposes a Modified Enhanced Local Pressure (MELP) model which can be utilised for hydraulic fracture modelling in both permeable rocks, such as sandstones, and also for near-impermeable rocks like shales. The MELP model is a two dimensional extended finite element (XFEM) model which focuses on improving the leak-off (transport of fluid from the fracture into the formation) model and coupling with pore-pressure.

- In Chapter 4, the XFEM model is extended to include the anisotropy (transverse isotropy) of the rock material properties. A parametric study on the effect of anisotropy on the fracture propagation direction was conducted by varying the degree of anisotropy in the material properties and the in-situ stress.

- Chapter 5, focuses on modelling the behaviour of hydraulic fractures in the presence of layered rocks. Fracture propagation across layers was studied for varying contrasts in material properties between the layers and varying reservoir properties. The chapter also focusses on the propagation of hydraulic fractures in the presence of inclusions, multi-stage hydraulic fracturing in an anisotropic and heterogeneous reservoir.

  In the final chapter, the main conclusions of this work are summarised. In addition, an outlook to the future research is given.

Chapter 2

Parametric study on hydraulic fracturing

Abstract

The aim of this chapter is to understand the sensitivity of hydraulic fractures with the various parameters that influence them. This is a vital requirement for the following chapters in this thesis as we choose to perturb only the sub-set of parameters which have a greater influence. A very brief review of the numerical models attempting to understand the hydraulic fracturing phenomenon is presented. The KGD model which provides an analytical solution for the hydraulic fracture problem is described. The standard KGD problem is then considered as a test example for the parametric study. A numerical model called Enhanced Local Pressure (ELP) model which is improved upon and utilised in the following chapters is used as the base model for the study to identify the vital parameters. The variation of the fracture characteristics (length, width and pressure at the fracture mouth) with the different parameters are observed.

2.1 Hydraulic fracture models

Several models have been developed for understanding the hydraulic fracture phenomenon, the earliest of which was developed by Geertsma and De Klerk (1969) to form the KGD model, which proposed an analytical solution to the problem by assuming plane strain conditions. Another analytical solution with a different geometrical assumption (fracture length >> fracture height) was given by Perkins and Kern (1961) and extended to include fluid loss by Nordgren (1972). Although these models have been accepted as a standard case for hydraulic fracturing due to its simplicity, it suffers from the assumption that the formation is assumed to be solid, the leak-off from fracture to formation is not captured accurately. Analytical asymptotic solutions were formulated by Garagash and Detournay (2000). Asymptotic solutions work by identifying small parameters and classifying the solution space into specific regimes (Detournay, 2004; Adachi and Detournay, 2008). Later these asymptotic solutions have been modified to take into account the leak-off, fracture toughness and fluid viscosity (Adachi and Detournay, 2008; Kovalyshen, 2010; Dontsov, 2017).

With the increase in applications of hydraulic fracturing and the advancement of numerical modelling techniques several detailed models were developed. These hydraulic fracture models made use of a variety of numerical techniques such as the finite element method, the boundary element method (McClure and Horne, 2014; Wu et al., 2015), the Discrete Element method (Al-Busaidi et al., 2005; Zhao et al., 2014), phase field method (Mikelic et al., 2015; Mikelić et al., 2015, 2019; Wilson and Landis, 2016; Heider and Markert, 2017; Van Duijn et al., 2019), and peridynamics (Ouchi et al., 2015; Oterkus et al., 2017). Finite element method (FEM) based models as developed by Schrefler et al. (2006); Secchi et al. (2007) used an adaptive mesh refinement technique for capturing the propagating fractures while other FEM models (Boone and Ingraffea, 1990; Segura and Carol, 2008b,a; Chen et al., 2009; Centeno Lobão et al., 2010; Carrier and Granet, 2012) captured them with the help of interface elements. These models made use of the cohesive zone approach as proposed by Dugdale (1960) and Barenblatt (1962) to overcome crack tip singularity whereas Peirce and Detournay (2008) used the near tip asymptotic solutions in combination with implicit level set algorithm (ILSA). Several hydraulic fracturing models (Lecampion, 2009; Mohammadnejad and Khoei, 2013; Remij et al., 2015a) were developed based on extended finite element method (XFEM) which makes use of the partition of unity property to take into account the discontinuity in the field without the need for re-meshing every time the fracture propagates. The XFEM model developed by Mohammadnejad and Khoei (2013) describes the fluid pressure with the help of a linear distance enrichment function whereas Remij et al. (2015a) uses a heaviside step function for the pressure in the porous media and an additional local

degree of freedom for the pressure inside the fracture. Meschke and Leonhart (2015) proposed a generalised finite element model in which the enrichment function used to model the fluid pressure is based on the physical formulation of the model.

The Enhanced Local Pressure (ELP) model proposed by Remij et al. (2015a) has been utilised as the base model for the parametric study. The further chapters in the thesis extend the aforementioned ELP model to overcome its limitations for addressing the objectives of this thesis.

2.2 KGD Model

A plane strain solution for the hydraulic fracture problem was initially developed by Khristianovic and Zheltov (1955) and later extended by Geertsma and De Klerk (1969) to formulate the KGD model. This model is applicable based on the geometrical consideration that the fracture height is much larger than the fracture length. The model assumes the medium surrounding the fracture to be non-porous. This restricts the applicability of the model to only rocks with very low permeability. This also results in the assumption that there is no fluid flow from the fracture into the surrounding medium. The model assumes, the fluid inside the fracture to be incompressible. With these assumptions in hand, Geertsma and De Klerk (1969) derived the analytical solution for the fracture propagation as given by Eqs.(2.1) - (2.3).

$$\mathrm{L} = 0.68\left(\frac{GQ^3}{\mu(1-\nu)}\right)^{1/6} t^{2/3} \tag{2.1}$$

$$\mathrm{CMOD} = 1.87\left(\frac{\mu(1-\nu)Q^3}{G}\right)^{1/6} t^{1/3} \tag{2.2}$$

$$\mathrm{CMP} = 1.135\left(\frac{G^3 Q\mu}{(1-\nu)^3 L^2}\right)^{1/4} \tag{2.3}$$

where L refers to the fracture length while CMOD, CMP refer to the width and pressure at the fracture mouth respectively. Q refers to the rate of injection of the fracturing fluid while μ refers to the viscosity of the fracturing fluid. G, ν refer to the shear modulus and the Poisson's ratio of the surrounding medium. t refers to the time period of injection of the fracturing fluid.

2.3 Test example

The standard KGD problem as described by Figure 2.1 is considered as the test example for the parametric study in this chapter. The solution to this example is

obtained from KGD analytical solution as well as the Enhanced Local Pressure (ELP) model. The aim of this example is not to compare the results of the numerical model with the analytical solution but to identify the sensitivity of the models to various parameters and identify the critical parameters.

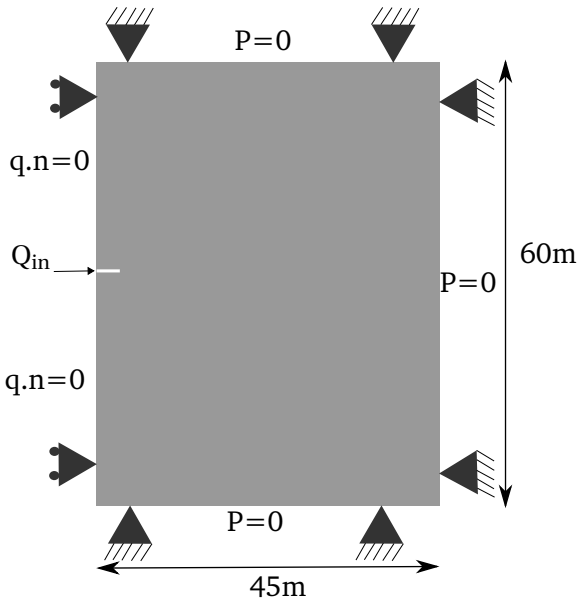

Figure 2.1: Geometry and boundary conditions of standard KGD problem.

Table 2.1: Isotropic value of parameters

Parameter	Reference Value
Young's modulus (E)	20 GPa
Poisson's ratio (ν)	0.2
Toughness(G_c)	120 N/m
Ultimate tensile strength (τ_{ult})	2 MPa
Ultimate shear strength (τ_s)	80 MPa
Permeability (κ)	10^{-19}m^2
Porosity (n_f)	0.1
Viscosity (μ)	0.01 Pa s
Solid bulk modulus (K_s)	36 GPa
Fluid bulk modulus (K_f)	3 GPa
Injection rate (Q_{rmin})	50 mm^2/s
Injection time (t)	20 s

The initial fracture is assumed to be horizontal, while it is free to propagate in any direction in the numerical model. The fracture is injected with a fluid

for 20 seconds with a time step of 0.1 s. The mesh for the numerical model consists of 50 mm × 50 mm elements. The reference values from which the parameters are varied are shown in Table 2.1.

2.4 Control Parameters

The parameters considered in this section (namely fluid injection rate and fracturing fluid viscosity) can be controlled by the operator, during the operation or planning stage of the fracturing problem. The variation in these parameters are user controlled and only restricted by the physical capabilities (like the large quantities of fluid required, fluids with the desired properties).

2.4.1 Fluid injection rates

The rate of injection of fluid (Q_{in}) into the fractures is varied and its effect on hydraulic fracture propagation is considered. As seen in Figure 2.2, the fracture increases in length as well as width for an increase in the injection rate. As more fluid volume is available in the same time, the pressure inside the fracture increases. This happens till the pressure reaches a critical value beyond which it causes the fracture to propagate further while also enhancing its width. This increase in fracture dimensions causes the pressure inside the fracture to reduce. Hence we see a more or less constant pressure, which is the critical pressure for fracture propagation, for the different injection rates. The different fractures profiles represent a concentric series for varying injection rates.

The analytical KGD model predicts a similar trend to the numerical model. The fracture length and the width at the mouth are proportional to the square root of the injection flow rate while pressure at the mouth is independent of the flow rate as can be seen in Figure 2.2.

A higher fluid injection rate is favourable for fracture propagation but the quantity of fracturing fluid required also increases with increasing rate. While cost of fracturing fluid is an economical issue, a greater concern is the handling and treatment of this large quantity of fluid which is mixed with chemicals at the end of the fracturing process.

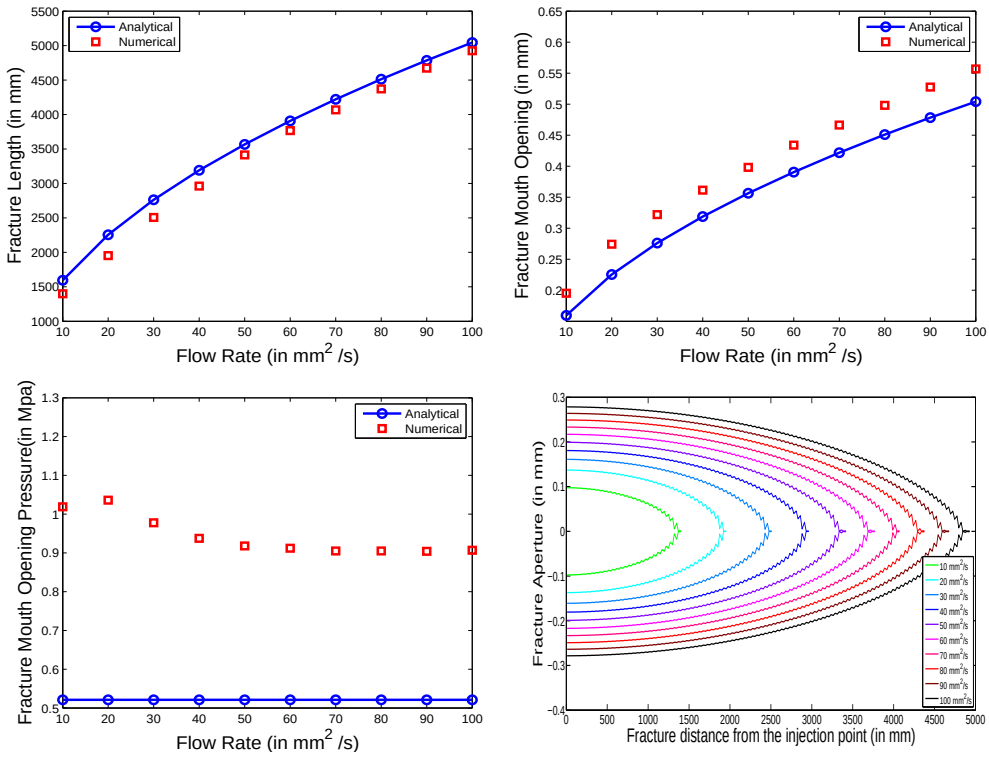

Figure 2.2: Variation of hydraulic fracture (length, width, profile, pressure at the mouth) with varying fluid injection rates

2.4.2 Fracture fluid viscosity

One of the major factors considered before deciding the fracking fluid is its viscosity. Several fracturing fluids like slick water (0.001 - 0.01 Pa · s), linear gels (0.01 - 0.1 Pa · s), cross linked gels (0.1 - 1 Pa · s) have been considered to give the required properties. The analytical KGD problem predicts that the fracture length is inversely proportional to the sixth root of viscosity, while the pressure and the width at the fracture mouth are proportional to the sixth root.

The numerical model follows the same trend as the KGD model. The viscosity of the fracturing fluid affects the hydraulic fracture process through two phenomenons: a) Transport of fluid inside the fracture b) Transport of the fluid from the fracture to the rock formation. The injected fluid flows from the mouth of the fracture to the tip of the fracture. As the viscosity of the fluid increases, there is an increased resistance for the fluid to reach the fracture tip. This causes less fluid to reach the fracture tip and hence lesser energy to propagate the fracture further. With the tendency of fluid to stay close to the

mouth of the fracture this also causes an increase in the fracture width in the region. This also results in the fracture becoming extremely narrow closer to the fracture tip as observed in Figure 2.3. This is also the reason why we see a divergence from the KGD model in the pressure for higher viscosities as the KGD assumes a uniform elliptical fracture shape always.

One of the reasons why highly viscous fluids are preferred in real field scenarios is due to the leak-off phenomenon. But this phenomenon is not noticably observed in this case due to the consideration of an extremely low permeability of the rock formation ($\kappa = 10^{-19}\text{m}^2$). An increase in the viscosity of the fluid causes a decrease in the leak-off into the rock formation, which ensures more availability of fluid to power the fracture propagation.

A fluid with a higher viscosity results in a short, wide fracture but becomes essential in a reservoir which has considerable permeability. A low viscosity fluid, which results in long narrow fracture, is preferable in extreme low permeable rocks like shales where the leak-off is not the most significant factor.

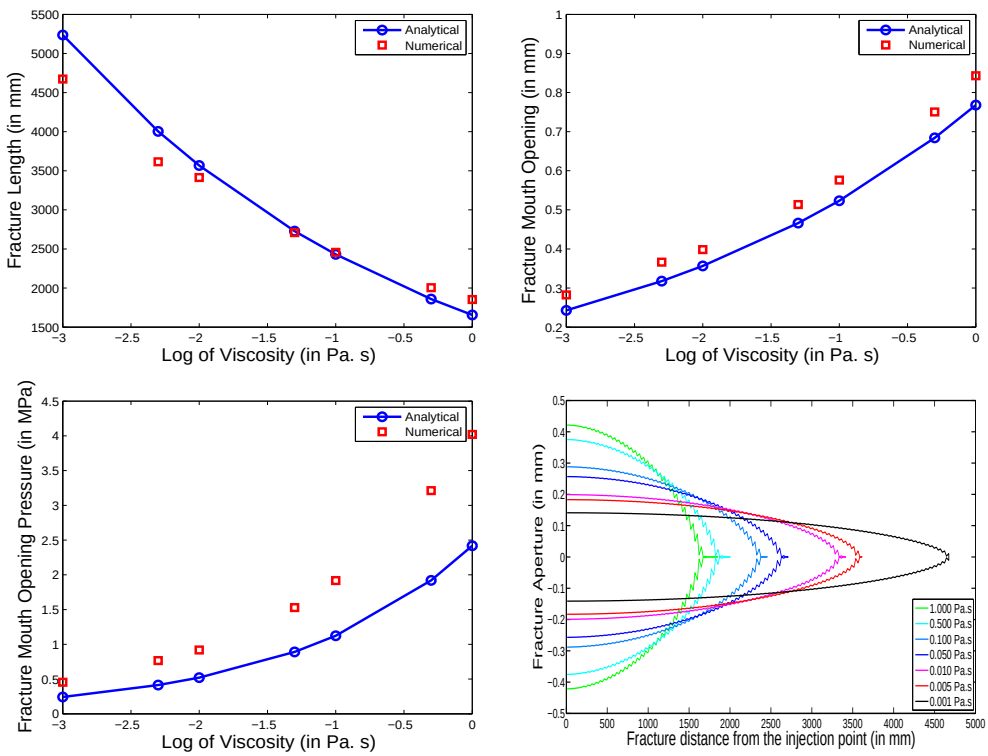

Figure 2.3: Variation of hydraulic fracture (length, width, profile, pressure at the mouth) with varying fracturing fluid viscosity

2.5 Material Properties

In the previous section we considered parameters whose values might be altered, but there are several parameters which cannot be modified for any given reservoir. These parameters are typically properties of the reservoir rock material like Young's modulus, Poisson's ratio, ultimate tensile strength, porosity and permeability.

2.5.1 Young's Modulus

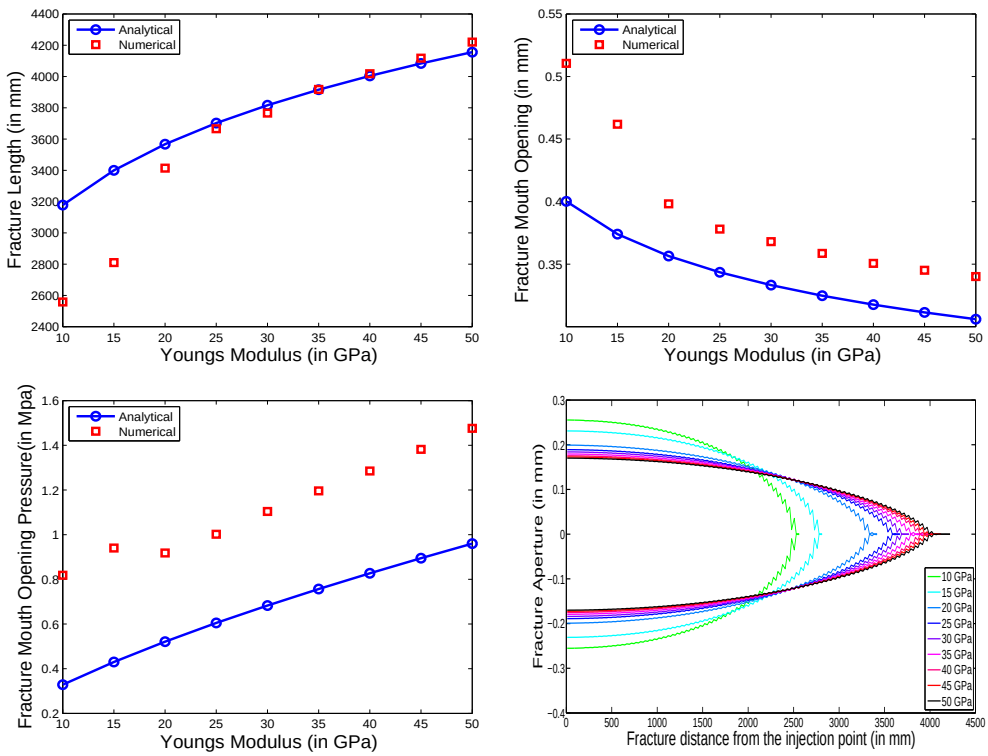

Figure 2.4: Variation of hydraulic fracture (length, width, profile, pressure at the mouth) with varying Young's modulus

The Young's modulus (E) of a rock formation can vary significantly depending on the composition and the structure of the minerals. Significant differences are found between the different sedimentary rock types like shales, sandstones, granite. In Figure 2.4, we observe the effect of young's modulus on hydraulic fracture propagation. The KGD analytical model observes that the fracture length and the pressure at the mouth is directly proportional to the sixth root

of Young's Modulus while the width at the fracture mouth is inversely proportional to it.

The numerical model shows a similar trend. With an increase in Young's modulus, the material becomes more stiffer causing the pressure required for fracture propagation to increase while the width at the mouth of the fracture decreases. This reduced width combined with a higher pressure results in more energy available to drive the fracture further. Hence we observe the increase of fracture length with the Young's Modulus. We also observe the region closer to the fracture tip becomes extremely narrow for increasing Young's modulus.

A rock formation with higher Young's modulus results in a narrow long fracture with an increase in the pressure required for propagation.

2.5.2 Poisson's Ratio

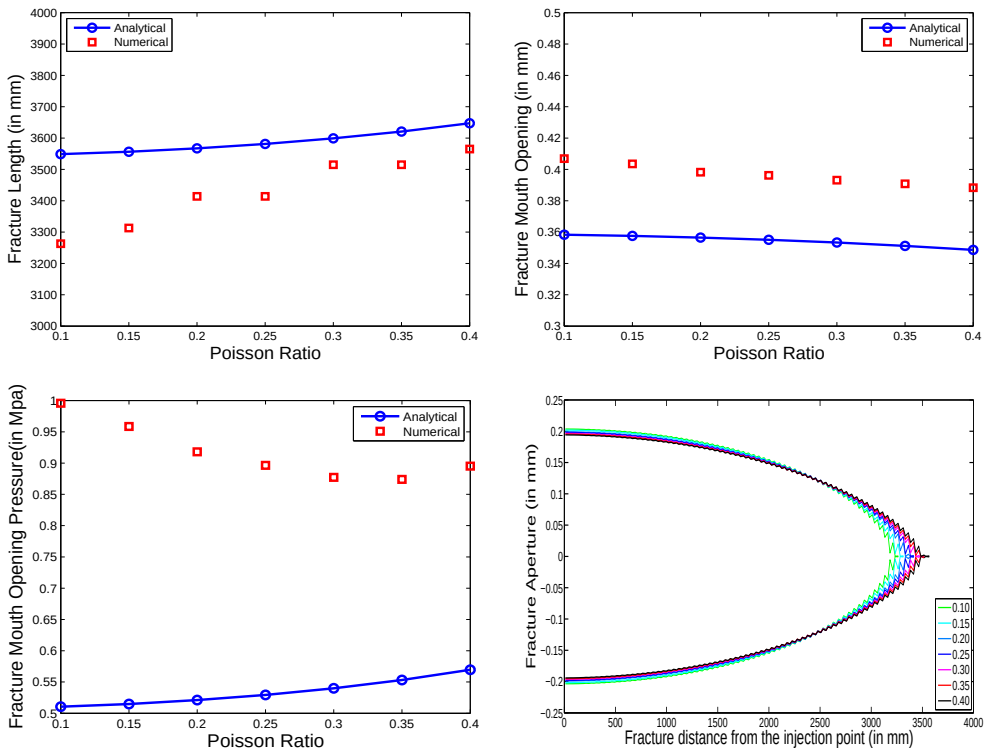

Figure 2.5: Variation of hydraulic fracture (length, width, profile, pressure at the mouth) with varying Poisson's ratio

In Figure 2.5, we observe the variation of a hydraulic fracture by varying the Poisson' ratio (ν) between 0.1 to 0.4. The analytical KGD model gives us the

relation between $(1-\nu)$ and the fracture characteristics. We can observe from Figure 2.5, that the variation of the fracture with Poisson's ratio is very minimal. Similar to the observations by the analytical model, the numerical ELP model predicts the fracture length to increase with increasing Poisson's ratio. A marginal decrease in the fracture mouth opening and a marginal increase in the fracture mouth pressure is observed.

Variation in Poisson's ratio does not have a significant impact on the fracture propagation characteristics.

2.5.3 Ultimate tensile strength

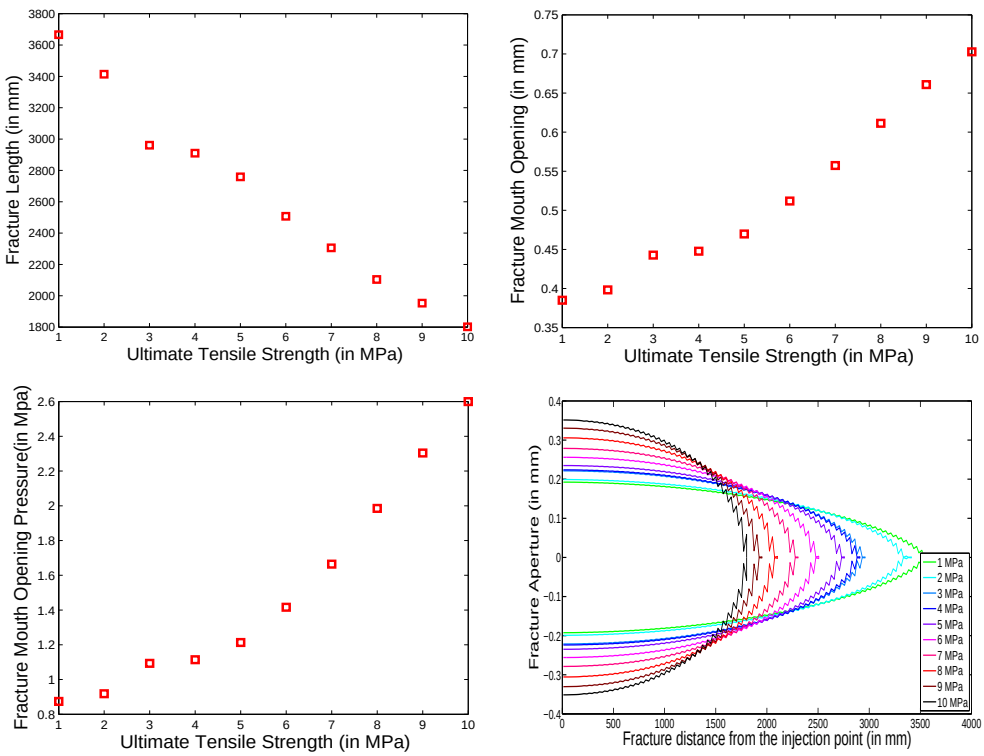

Figure 2.6: Variation of hydraulic fracture (length, width, profile, pressure at the mouth) with varying ultimate tensile strength

Ultimate tensile strength (τ_{ult}) is the stress value in tension beyond which material failure occurs. For a rock material, it also depends on the degree to which the rock is ductile or brittle in nature. The ultimate tensile strength value for rocks are not well documented as the Young's modulus. The analytical KGD

model does not take into account the ultimate tensile strength of the formation. Hence only the numerical model is used to study the effect on hydraulic fracture by varying the ultimate tensile strength from 1 MPa to 10 MPa.

From Figure 2.6, it can be observed that the variation in ultimate tensile strength has significant effect on the fracture characteristics. A rock formation with a higher ultimate tensile strength makes it harder for the fracture to propagate causing the fracture length to decrease and also the fracture pressure at the mouth increases as more energy is required to break the material. This higher fluid pressure inside the fracture also results in an increased fracture width at the mouth since the stiffness of the rock remains constant.

A rock formation with higher Ultimate tensile strength results in a wider and shorter fracture with an increase in the pressure required for fracture propagation.

2.5.4 Porosity

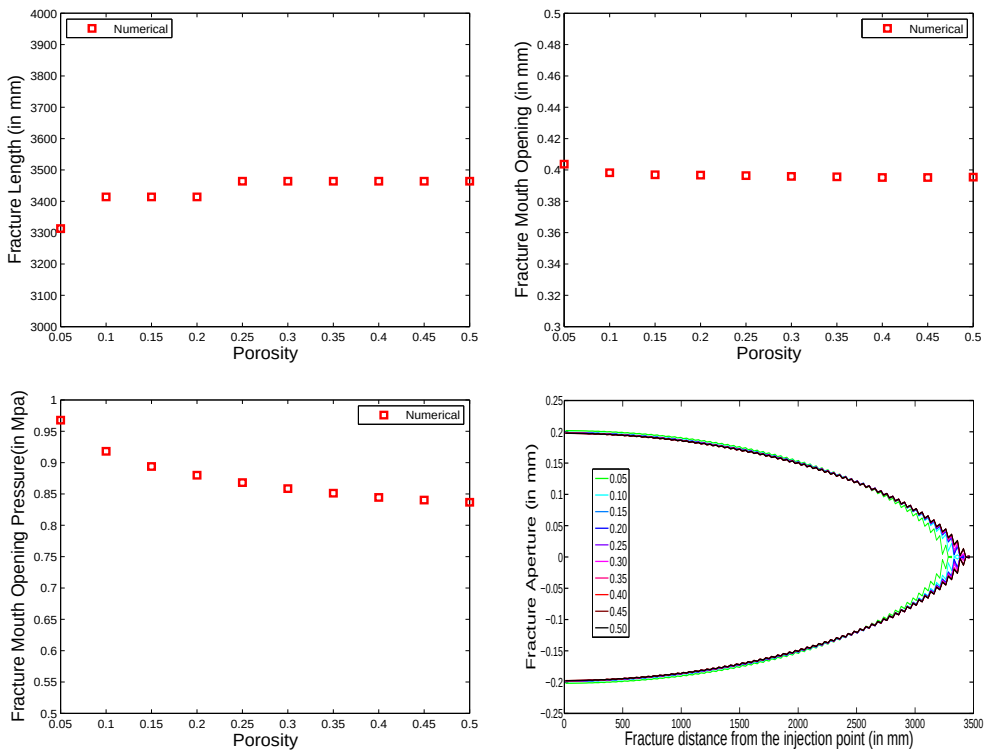

Figure 2.7: Variation of hydraulic fracture (length, width, profile, pressure at the mouth) with varying porosity of the porous medium

A porous medium consists of a solid grains and pores. Porosity represents the ratio of pore volume to the total volume of the porous medium. Typical porosity values varies from 5% to 50% in most rocks. As seen in Figure 2.7, the variation in porosity has very minimal effects on the hydraulic fracture propagation. This is due to the fact that the porosity affects the ELP model only through the alteration of the bulk modulus and compressibility modulus of the porous medium. Although porosity has a positive correlation with permeability, with a few relations (like Kozeny–Carman equation) for defining the relationship , it has not been taken into account in the ELP model. This is due to the empirical nature of these relations caused by assumptions around the sphericity of the particles and the type of flows. The KGD problem assumes the medium surrounding the fracture to be solid hence porosity does not come into consideration.

Porosity is observed to have negligible impact on the hydraulic fracture propagation.

2.5.5 Permeability

Permeability is the measure of the ability of fluids to flow through a porous medium. It is dependent on interconnectivity of the pore spaces in a rock formation. The different sedimentary rock types have differing permeabilities, like shales and granite exhibit very low permeabilities of $< 10^{-17}\mathrm{m}^2$ while sandstones and carbonates exhibit higher permeabilities in the order of $10^{-14}\mathrm{m}^2$ – $10^{-17}\mathrm{m}^2$. The KGD model assuming a solid medium, does not take into account the permeability for modelling of hydraulic fracturing.

As observed in Figure 2.8, the fracture characteristics shows a step behaviour in response to the permeability variation. This is due to the fact that the major effect of permeability on the fracture growth is based on the leak-off phenomenon. The leak-off phenomenon as explained in the earlier section on viscosity is the transport of the fracturing fluid from the fracture into the rock formation. Rocks with higher permeability result in greater leak-off thereby reducing the volume of fluid available for fracture propagation. This in-turn results in lower fracture length and lower fracture width. Since the variation in permeability considered here is in order of magnitude differences it causes the leak-off volume to change in an exponential manner as observed in Figure 2.9. Once the leak off volume becomes a considerable portion of the total injected volume, then it has a major impact on the fracture propagation. This is the reason hydraulic fracturing is preferable in rocks with lower permeability.

An increase in permeability causes more fluid to leak-off causing the fracturing to reduce in length and its width.

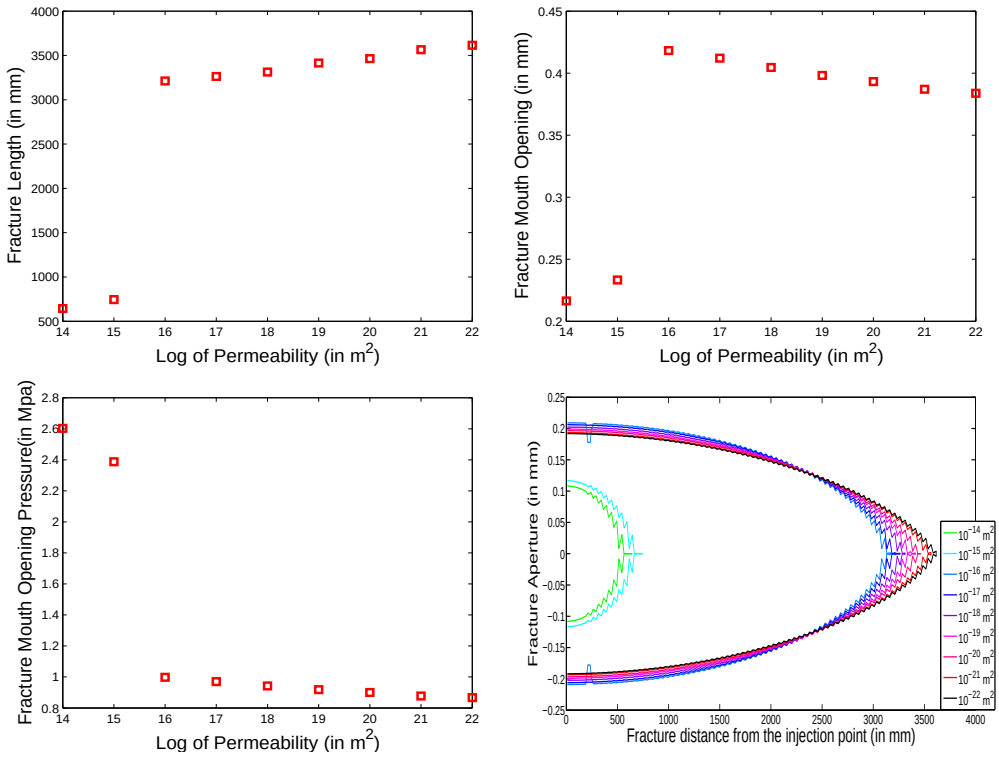

Figure 2.8: Variation of hydraulic fracture (length, width, profile, pressure at the mouth) with varying permeability of the rock formation

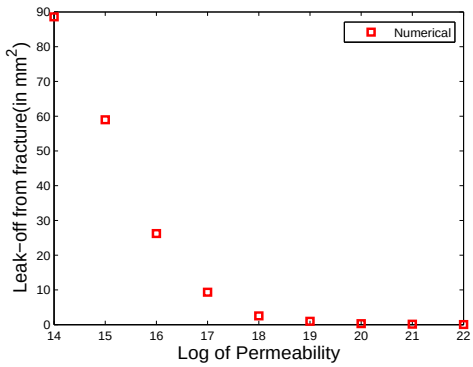

Figure 2.9: Variation of leak-off from the fracture with varying permeability of the rock formation

2.6 Summary

Sensitivity of various parameters (user controlled and rock material properties) on hydraulic fractures were studied. The user controlled parameters of fluid injection rate and fluid viscosity are found to have a significant impact on the hydraulic fracture propagation. In the parameters which are dependent on the rock properties, Young's modulus and ultimate tensile strength were found to have a significant effect on the fracture while Poisson's ratio and porosity had negligible effect. Sensitivity with permeability is dependent on the magnitude of the actual permeability value.

Chapter 3

Modified Enhanced Local Pressure (MELP) model

Abstract

In this chapter, we propose a fully coupled two-dimensional hydraulic fracture model which can be used in both near impermeable (shales and granites) rocks and also in permeable (sandstone, limestone, dolomites) rocks. We make use of extended finite element method along with an exponential cohesive zone model for modelling the fracture. Using Biot's theory of poro-elasticity, we model the mechanical behaviour of a fully saturated porous medium to obtain the solid deformation in the grains, and fluid pressure in the pores. We consider an additional degree of freedom to model the pressure inside the fracture arising due to the injection of fluid and its leak off into the porous medium. Leak-off from fracture to the porous medium becomes vital in permeable rocks which have a much higher permeability compared to the near impermeable rocks. An accurate leak-off model which is fully coupled with the fluid flow in the porous medium is proposed based on the analytical solution for 1-D Terzaghi consolidation equation. The effect of this improved leak-off model on single fracture propagation and a fracture network formation is studied with numerical examples.

Reproduced from: Valliappan, V., Remmers, J. J. C., Barnhoorn, A., & Smeulders, D. M. J., A fully coupled hydraulic fracturing model with accurate analysis of the leak-off phenomenon in porous rocks. International Journal for Numerical and Analytical Methods in Geomechanics, submitted, 2019.

3.1 Introduction

Fluid leak-off phenomenon in hydraulic fracturing is the transport of fracturing fluid from the fracture to the formation. This becomes an important phenomenon in modelling of permeable (sandstone, limestone, dolomites) rocks as they have a significant permeability which causes a significant amount of fluid to be lost from the fracture which directly influences the fluid pressure within the fracture and hence the fracturing process. The analytical KGD model described in the previous chapter and several early hydraulic fracture models assumed that there is no fluid leak-off. While these models can be expected to give reasonable estimates of the fracture growth in near impermeable rocks, they cannot be used for permeable rocks.

There have been several models that have focused specifically on understanding the leak-off phenomenon. The classical Carter's law (Howard and Fast, 1957) proposes that the leak-off is inversely proportional to the square root of time. It also requires the knowledge of a leak-off co-efficient, which is determined from laboratory experiments. Numerical models that accurately obtain leak-off by solving the multiphase flow equations in porous media have been proposed (Settari et al., 1985; Yi et al., 1994; Valkó et al., 1997). They consider the fracturing fluid to form a filter cake and the filtrate passing through it to compress the reservoir fluid. However, all these models are applicable only for non-propagating fractures.

In models with propagating hydraulic fractures, some formulations (Adachi and Detournay, 2008; Carrier and Granet, 2012; Bunger et al., 2005) make use of the empirical Carter's law while some other formulations (Mohammadnejad and Khoei, 2013; Fan et al., 1995; Yang et al., 2016) obtain the leak-off by using a fully coupled model. These models work well for rocks with significant permeability, but they require a very fine mesh close to the fracture in case of near impermeable rocks like shales due to the steep pressure gradient. The enhanced local pressure (ELP) model proposed by Remij et al. (2015a), captures the steep pressure gradient accurately with the help of Terzaghi's consolidation equation (Terzaghi, 1925). This approach works well for shales, but it fails to take into account the effect of leak-off on the pore pressure in the formation, which becomes vital for rocks with significant permeability. This causes the ELP model to have a discontinuous jump in the pressure from the fracture to the formation even in highly permeable rocks.

In this chapter, we extend the aforementioned ELP model by Remij et al. (2015a) by applying an improved leak-off model which couples the leak-off phenomenon with the pore pressure in the formation, to form a modified enhanced local pressure model (MELP). Thereby forming a unified model which can accurately model the leak off and fracture propagation in both near impermeable rocks, such as shales and granites, and also in permeable rocks, such as

sandstones, limestone and dolomites.

The chapter is organised as follows: Section 3.2 describes the kinematic relations in the model and also the various sub-models which describe the different phenomenons occurring in the hydraulic fracture problem. In section 3.3, we derive the set of equations governing the problem from the standard mass and momentum balance equations. In section 3.4, we describe the numerical discretisation required to solve the aforementioned set of equations. Finally in section 3.5, we use numerical examples to validate and understand the MELP model.

3.2 Mathematical Model

Consider a body Ω which contains the discontinuity Γ_d as shown in Figure 3.1. The degrees of freedom in the body Ω, which undergo a discontinuous jump across Γ_d, can be represented by continuous fields in the domains Ω^+ and Ω^-. The normal ($\vec{\boldsymbol{n}}_d$) to the discontinuity surface Γ_d, is always assumed to be pointing towards the Ω^+ domain. Boundary conditions are specified along the external surface (Γ) of the body.

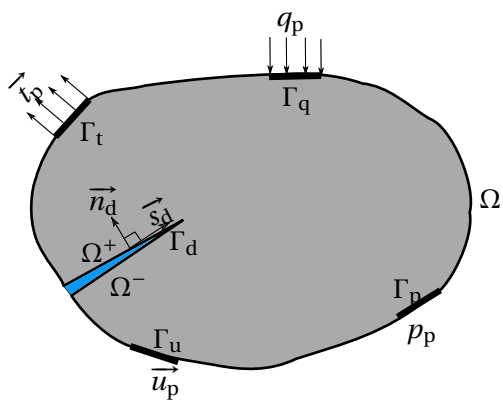

Figure 3.1: A body Ω containing a discontinuity Γ_d along with the specified boundary conditions

3.2.1 Kinematics

For describing the state of a porous formation, we need two fields, i.e the displacement in the solid grains and fluid pressure in the pores. In addition for a porous formation with a fracture, we need to model the discontinuous jump of the displacement field.

Hence, the displacement field in the solid skeleton of the porous medium is described as:

$$\boldsymbol{u} = \hat{\boldsymbol{u}} + H_{\Gamma_\mathrm{d}} \tilde{\boldsymbol{u}} \quad \text{when} \quad \mathrm{x} \notin \Gamma_\mathrm{d} \tag{3.1}$$

where $\hat{\boldsymbol{u}}$ denotes the regular displacement field which is used to represent a domain without a discontinuity, while $\tilde{\boldsymbol{u}}$ represents the additional displacement field which along with a heaviside enrichment function models the discontinuity. This heaviside function is represented as:

$$H_{\Gamma_\mathrm{d}} = \begin{cases} 1 & \text{when} \quad \mathrm{x} \in \Omega^+ \\ 0 & \text{when} \quad \mathrm{x} \in \Omega^- \end{cases} \tag{3.2}$$

The jump in displacement across the discontinuity can be obtained from the additional displacement degree of freedom and the enrichment function as:

$$\boldsymbol{v}_\mathrm{d} = (H_{\Gamma_{\mathrm{d}^+}} - H_{\Gamma_{\mathrm{d}^-}}) \tilde{\boldsymbol{u}} = \tilde{\boldsymbol{u}} \quad \text{when} \quad \mathrm{x} \in \Gamma_\mathrm{d} \tag{3.3}$$

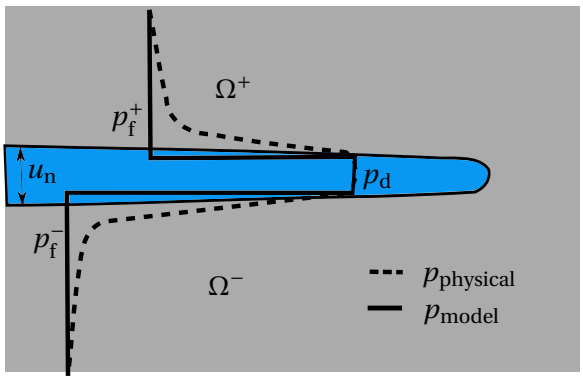

Figure 3.2: Representation of pressure profile across fractures

For a porous medium with a hydraulic fracture we need to model the pressure inside the fracture in addition to the pressure in the pores. Computing the fluid pressure inside the fracture is complicated due to the involvement of various processes such as: i) injection of fluid from external sources ii) the movement of fracture surfaces and iii) the leak-off from fracture into the adjacent formation. In order to take into account these complications, an additional degree of freedom for pressure inside the fracture is used (Remij et al., 2015a). As shown in Figure 3.2, this causes the pressure profile to be discontinuous.

Hence the fluid pressure in the pores and inside the fracture are represented as:

$$p = \hat{p} + H_{\Gamma_\mathrm{d}} \tilde{p} \quad \text{when} \quad \mathrm{x} \notin \Gamma_\mathrm{d} \tag{3.4}$$

$$p = p_\mathrm{d} \quad \text{when} \quad \mathrm{x} \in \Gamma_\mathrm{d} \tag{3.5}$$

where $\hat{p}$ and $\tilde{p}$ are the regular and additional pressure fields describing the pressure in the porous formation while p_{d} is used to describe the pressure in the discontinuity.

3.2.2 Poromechanics model

We make use of Biot's theory of poro-elasticity to formulate a coupled poromechanics model. We assume the porous medium to be in isothermal conditions and fully saturated i.e. the pores are filled with a single phase fluid.

Solid Phase In a fully saturated porous medium, the external stresses on the porous media are partly taken by the fluid pressure in the pores and partly by deformation of the solid grains. This can be represented mathematically as:

$$\boldsymbol{\sigma} = \boldsymbol{\sigma}_{\mathrm{e}} - \alpha p \boldsymbol{I} \tag{3.6}$$

where $\boldsymbol{\sigma}$ is the total stress, $\boldsymbol{\sigma}_{\mathrm{e}}$ is effective stress. Tensile stresses are considered to be positive and Biot's co-efficient (α) is defined as:

$$\alpha = 1 - \frac{K}{K_{\mathrm{s}}} \tag{3.7}$$

where K is the drained bulk modulus of the porous medium while K_{s} represents the bulk modulus of the solid grains in the porous medium.

The effective elastic stresses in the solid grain is related to the elastic strains by means of generalised Hooke's law:

$$\boldsymbol{\sigma}_{\mathrm{e}} = \boldsymbol{C}\boldsymbol{\epsilon} \tag{3.8}$$

where $\boldsymbol{C}$ is the consistent tangent modulus of the solid grains and $\boldsymbol{\epsilon}$ is the elastic strain tensor in the solid grains. Assuming small strains, we represent the strain in the porous medium as:

$$\boldsymbol{\epsilon} = \nabla^{\mathrm{s}} \hat{\boldsymbol{u}} + H_{\Gamma_{\mathrm{d}}} \nabla^{\mathrm{s}} \tilde{\boldsymbol{u}} \tag{3.9}$$

where ∇^{s} represents the symmetric part of the gradient.

Flow in the porous formation The fluid flow in the porous medium is described using Darcy's law as:

$$\boldsymbol{q} = -\frac{\kappa}{\mu} \nabla p \tag{3.10}$$

where κ is the intrinsic permeability, μ is the dynamic viscosity of the fluid. An outward fluid flux is considered positive, hence the negative sign is required to represent a fluid flow from high pressure to low pressure region.

Flow inside the fracture Since the fracture length is much larger than its width, we assume the pressure along the width of the fracture to be constant. This causes a one-dimensional flow inside the fracture along the tangential direction. This tangential flow inside the fracture is described as:

$$q_{\text{tang}} = -\frac{\kappa_{\text{d}}}{\mu}\frac{\partial p_{\text{d}}}{\partial s} \tag{3.11}$$

where κ_{d} is the permeability within the fracture. Witherspoon et al. (1980) described the flow inside a fracture to be similar to flow between two parallel plates and obtained the permeability as $v_{\text{n}}^2/12$.

3.2.3 Cohesive Zone Model

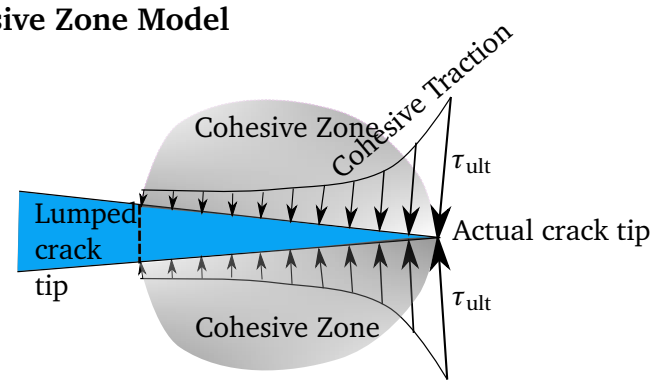

Figure 3.3: Schematic of a Cohesive zone model

The fracture is described using a cohesive zone model, where the crack tip is lumped on to a plane ahead of the actual crack tip as seen in Figure 3.3. The cohesive zone, from the fictitious crack tip to the actual crack tip, has cohesive traction acting along the fracture surfaces (Barenblatt, 1962). This is to signify that the material is only partially damaged in the cohesive zone with some material bondings still intact in the presence of micro cracks.

The cohesive traction ($\boldsymbol{t}_{\text{d}}$) is dependent upon the displacement jump across the fracture ($\boldsymbol{v}_{\text{d}}$) and a history parameter. The hydraulic fracture openings are assumed to be predominant in the normal direction. Hence we neglect the shear tractions and assume an exponential traction-separation relation (Needleman, 1987) for normal tractions.

$$t_{\text{n}} = \tau_{\text{ult}} \exp\left(\frac{-v_{\text{n}}\tau_{\text{ult}}}{G_{\text{c}}}\right) \tag{3.12}$$

where τ_{ult} is the ultimate tensile strength, G_{c} is the toughness of the rock material.

The linear form of this traction displacement relation is written as:

$$\triangle t_{\text{n}} = T \triangle v_{\text{n}} \quad \text{where} \quad T = \frac{\partial t_{\text{n}}}{\partial v_{\text{n}}} \tag{3.13}$$

where T is the tangential stiffness matrix obtained by differentiating the binomial expansion of Eq. 3.12 as:

$$T = \tau_{\text{ult}}(-\frac{\tau_{\text{ult}}}{G_{\text{c}}} + \frac{\nu_{\text{n}}\tau_{\text{ult}}^2}{G_{\text{c}}^2} - ...) \tag{3.14}$$

3.2.4 Leak-off model

For accurate modelling of hydraulic fracturing in rocks with significant permeability, it is very important to take into account the leak-off phenomenon. Owing to the significant permeability, the ratio of the volume of fluid leak-off to the the total fluid injection volume is high. The leak-off volume is dependent upon the pressure gradient at the fracture surface. As observed in Figure 3.2, we have a discontinuous model for the pressure. Hence we make use of 1-D Terzaghi consolidation equation to recreate the physical pressure gradients in the vicinity of the fracture. This gives us the advantage of using a coarse mesh near the fractures but still capture the high pressure gradients accurately in case of near impermeable rocks like shales.

The Terzaghi consolidation model (Terzaghi, 1925) is well known where any excess loading on the soil layer is transmitted as an over pressurisation of the saturating fluid in the transient state. Over time the excess pressure in the fluid keeps reducing reaching the original pressure state at infinite time. Terzaghi derived the equations for obtaining this excess pressure in the saturating fluid as a function of time and distance from the surface of the soil layer. In MELP, we utilise the same equation for modelling the excess pressure that is observed in the pore fluid due to the leak-off of fluid from the fracture into the formation. The Terzaghi model helps us in obtaining the excess pore pressure as a function of time, distance from the fracture and the amount of fluid leak-off.

The MELP model obtains the leak-off using the solution for a one dimensional semi-infinite fluid saturated poro elastic consolidation problem which can be stated by the following equation (Terzaghi, 1925):

$$\frac{\partial p}{\partial t} = C_{\text{v}}\frac{\partial^2 p}{\partial y^2} \quad \text{for} \quad \text{t} > 0 \quad \text{and} \quad 0 < \text{y} < \infty \tag{3.15}$$

where C_{v} is the Terzaghi consolidation co-efficient which can be given as (Detournay and Cheng, 1993):

$$C_{\text{v}} = \frac{\kappa M}{\mu}\frac{K + \frac{4}{3}G}{K_{\text{u}} + \frac{4}{3}G} \tag{3.16}$$

where μ is the dynamic viscosity of the fluid, M is the compressibility modulus or Biot's modulus, K and K_{u} are the drained and undrained bulk modulus

and G is the shear modulus of the porous medium. The boundary conditions associated with the problem are: constant fluid flux (Neumann type boundary condition) at the near boundary and drained condition at the far boundaries which are represented as:

$$\boldsymbol{q}(0,t) = \boldsymbol{Q}_{\text{flux}} \quad \text{for} \quad t > 0 \tag{3.17}$$

$$p(\infty,t) = 0 \quad \text{for} \quad t > 0 \tag{3.18}$$

Solving Equation 3.15 and using the boundary conditions, one can obtain the pressure increase in the porous medium as:

$$\triangle p(y,t) = \frac{2\mu \boldsymbol{Q}_{\text{flux}}}{\kappa}\left(\sqrt{\frac{c_{\text{v}}t}{\pi}}\,\exp\left(\frac{-\text{y}^2}{4\text{c}_{\text{v}}\text{t}}\right) - \frac{\text{y}}{2}\,\text{erfc}\left(\frac{\text{y}}{2\sqrt{\text{c}_{\text{v}}\text{t}}}\right)\right) \tag{3.19}$$

At the influx point into the porous medium (y=0) which is the interface between the fracture and the porous formation, we obtain the influx volume as a function of the pressure differences at the interface as:

$$\boldsymbol{Q}_{\text{flux}} = \frac{\kappa}{2\mu\sqrt{\frac{C_{\text{v}}t}{\pi}}}\;\triangle p(0,t) \tag{3.20}$$

In the MELP model, we assume that the classical consolidation process occurs only for the instantaneous time step. The pore pressure is modified at every instant due to the changing stress state close to the fracture and also due to the leak-off from previous time steps. Hence in MELP, we model the leak-off by using the analytical solution at instantaneous time steps and update the pore pressure after every time step. The updated pore pressure is used as the initial pressure for the consolidation process at the next time step. This ensures that the changes in pore pressure due to the modified stress state as well as the previous leak-off are captured.

Hence we can relate the fluid leak-off at any instantaneous time with the pressure differences at the interface with the help of a coupling co-efficient C_{a} as:

$$\boldsymbol{Q}_{\text{flux}} = C_{\text{a}}\;(p_{\text{d}} - p_{\text{f}}) \qquad \text{where} \qquad C_{\text{a}} = \frac{\kappa}{2\mu\sqrt{\frac{C_{\text{v}}\triangle t}{\pi}}} \tag{3.21}$$

where $\triangle t$ is the time step of the simulation.

The expression for leak-off in the MELP model is given by including the leak-off from the two sides of the fracture as:

$$q_{\text{leak}} = (\boldsymbol{q}_{\Gamma_{\text{d}^+}} - \boldsymbol{q}_{\Gamma_{\text{d}^-}}) \cdot \boldsymbol{n}_{\text{d}} = C_{\text{a}}(p_{\text{d}} - p_{\text{f}}^{+}) + C_{\text{a}}(p_{\text{d}} - p_{\text{f}}^{-}) \tag{3.22}$$

where p_{d} is the pressure inside the fracture, p_{f}^{+} and p_{f}^{-} are the pore pressures on either side of the fracture inside the porous media.

The ELP model developed by Remij et al. (2015a) considers a similar solution to the leak-off but it assumes that there is a uniform consolidation process from the time the discontinuity was created. Also the ELP model fails to incorporate the increase in pore pressure due to this leak-off, as it is inherently taken into account in the analytical solution.

3.3 Governing Equations

In this section, we obtain the set of equations which govern the hydraulic fracture problem using the mass and momentum balance equations along with the auxiliary equations described in the previous section.

3.3.1 Momentum Balance

The linear momentum balance equation is written as:

$$\nabla \cdot \boldsymbol{\sigma} = 0 \tag{3.23}$$

with boundary conditions prescribing either displacement ($\boldsymbol{u} = \boldsymbol{u}_{\mathrm{p}}$ on Γ_{u}) or traction ($\boldsymbol{\sigma} \cdot \boldsymbol{n}_{\Gamma} = \boldsymbol{t}_{\mathrm{p}}$ on Γ_{t}) at the boundaries.

The other boundary conditions which ensures stress continuity along the fracture faces is given as : $\boldsymbol{\sigma} \cdot \boldsymbol{n}_{\Gamma_{\mathrm{d}}} = \boldsymbol{t}_{\mathrm{d}} - p_{\mathrm{d}} \boldsymbol{n}_{\mathrm{d}}$ along Γ_{d} where $\boldsymbol{t}_{\mathrm{d}}$ corresponds to the cohesive traction obtained using Eq.(3.12).

3.3.2 Mass Balance

The mass balance equation for saturated porous medium (Detournay and Cheng, 1993) is given as:

$$\alpha \nabla \cdot \dot{\boldsymbol{u}} + \frac{\dot{p}}{M} + \nabla \cdot \boldsymbol{q} = 0 \tag{3.24}$$

where $\dot{\boldsymbol{u}}$ is the velocity vector of solid deformation, $\dot{p}$ is the time derivative of fluid pressure in the pores, $\mathbf{q}$ is the flux and M is the compressibility modulus of the porous media. Boundary conditions associated with the mass balance equation are either prescribed pressure along the boundaries ($p = p_{\mathrm{p}}$ on Γ_{p}) or prescribed flux across the boundaries ($\boldsymbol{q} \cdot \boldsymbol{n}_{\Gamma} = q_{\mathrm{p}}$ on Γ_{q}).

3.3.3 Mass Balance in the fracture

This additional governing equation ensures the mass conservation inside the fracture. Irzal et al. (2013) obtained the local mass continuity equation by analytical integration of the mass balance equation given by Eq.(3.24) over the width of the fracture.

$$q_{\mathrm{leak}} - v_{\mathrm{n}} \frac{\partial}{\partial s}\left(\frac{\kappa_{\mathrm{d}}}{\mu} \frac{\partial p_{\mathrm{d}}}{\partial s}\right) + \dot{v}_{\mathrm{n}} + v_{\mathrm{n}} \left\langle \frac{\partial \dot{v}_{\mathrm{s}}}{\partial s} \right\rangle + \frac{v_{\mathrm{n}}}{K_{\mathrm{f}}} \dot{p}_{\mathrm{d}} = 0 \tag{3.25}$$

where q_{leak} is the leak off from the fracture into the formation, v_{n} is the fracture opening in the normal direction, v_{s} is the shear displacement of the fracture surface, the symbol $\langle . \rangle$ denotes average of the quantity over the fracture width, p_{d} is the pressure inside the fracture, K_{f} is the bulk modulus of the fluid, κ_{d} is the permeability within the fracture.

The mass conservation of the fluid inside the fracture is governed by three different mechanisms: 1) Movement of the fracture boundaries which is governed by the displacement terms (3 and 4th terms present in Eq. 3.25 obtained by integrating the first term in Eq. 3.24). 2) Movement of fluid along and across the fracture (first two terms in Eq. 3.25 obtained from the last term in Eq. 3.24) 3) Change in pressure of the fluid inside the fracture represented by the last term in Eq. 3.25.

3.3.4 Weak Form

In the previous subsection, the strong differential form of the governing equations along with their associated boundary conditions were presented. In this subsection, we obtain the weak integral form of these governing equations by integrating them over the two dimensional domain Ω_{e} along with an admissible test function for each field variable. We assume three test functions $\boldsymbol{\eta}$, ξ, Ψ corresponding to the field variables $\boldsymbol{u}$, p, p_{d} respectively. These test functions are assumed to be in the same form as their underlying field variables such that $\boldsymbol{\eta} = \hat{\boldsymbol{\eta}} + H_{\Gamma_{\text{d}}}\tilde{\boldsymbol{\eta}}$, and $\xi = \hat{\xi} + H_{\Gamma_{\text{d}}}\tilde{\xi}$.

Multiplying Eqs.(3.23),(3.24),(3.25) by their corresponding test functions $\boldsymbol{\eta}$, ξ, Ψ and applying Gauss's divergence theorem, we obtain the following integral equations:

$$\begin{aligned}\int_{\Omega_{\text{e}}} \nabla(\hat{\boldsymbol{\eta}} + H_{\Gamma_{\text{d}}}\tilde{\boldsymbol{\eta}}) : \boldsymbol{\sigma} \, \mathrm{d}\Omega_{\text{e}} = \int_{\Gamma_{\text{t}}} (\hat{\boldsymbol{\eta}} + H_{\Gamma_{\text{d}}}\tilde{\boldsymbol{\eta}}) \cdot (\boldsymbol{\sigma} \cdot \boldsymbol{n}_{\Gamma}) \, \mathrm{d}\Gamma_{\text{t}} + \int_{\Gamma_{\text{u}}} (\hat{\boldsymbol{\eta}} + H_{\Gamma_{\text{d}}}\tilde{\boldsymbol{\eta}}) \cdot (\boldsymbol{\sigma} \cdot \boldsymbol{n}_{\Gamma}) \, \mathrm{d}\Gamma_{\text{u}} \\ - \int_{\Gamma_{\text{d}^+}} (\hat{\boldsymbol{\eta}} + H_{\Gamma_{\text{d}^+}}\tilde{\boldsymbol{\eta}}) \cdot (\boldsymbol{\sigma} \cdot \boldsymbol{n}_{\text{d}}) \, \mathrm{d}\Gamma_{\text{d}^+} + \int_{\Gamma_{\text{d}^-}} (\hat{\boldsymbol{\eta}} + H_{\Gamma_{\text{d}^-}}\tilde{\boldsymbol{\eta}}) \cdot (\boldsymbol{\sigma} \cdot \boldsymbol{n}_{\text{d}}) \, \mathrm{d}\Gamma_{\text{d}^-}\end{aligned} \tag{3.26}$$

$$\begin{aligned}\alpha \int_{\Omega_{\text{e}}} (\hat{\xi} + H_{\Gamma_{\text{d}}}\tilde{\xi}) \nabla \cdot \dot{\boldsymbol{u}} \, \mathrm{d}\Omega_{\text{e}} - \int_{\Omega_{\text{e}}} \nabla(\hat{\xi} + H_{\Gamma_{\text{d}}}\tilde{\xi}) \cdot \boldsymbol{q} \, \mathrm{d}\Omega_{\text{e}} + \int_{\Omega_{\text{e}}} (\hat{\xi} + H_{\Gamma_{\text{d}}}\tilde{\xi}) \frac{\dot{p}}{M} \, \mathrm{d}\Omega_{\text{e}} = \\ - \int_{\Gamma_{\text{q}}} (\hat{\xi} + H_{\Gamma_{\text{d}}}\tilde{\xi})(\boldsymbol{q} \cdot \boldsymbol{n}_{\Gamma}) \, \mathrm{d}\Gamma_{\text{q}} - \int_{\Gamma_{\text{p}}} (\hat{\xi} + H_{\Gamma_{\text{d}}}\tilde{\xi})(\boldsymbol{q} \cdot \boldsymbol{n}_{\Gamma}) \, \mathrm{d}\Gamma_{\text{p}} \\ + \int_{\Gamma_{\text{d}^+}} (\hat{\xi} + H_{\Gamma_{\text{d}}}\tilde{\xi})(\boldsymbol{q}_{\Gamma_{\text{d}^+}} \cdot \boldsymbol{n}_{\text{d}}) \, \mathrm{d}\Gamma_{\text{d}^+} - \int_{\Gamma_{\text{d}^-}} (\hat{\xi} + H_{\Gamma_{\text{d}}}\tilde{\xi})(\boldsymbol{q}_{\Gamma_{\text{d}^-}} \cdot \boldsymbol{n}_{\text{d}}) \, \mathrm{d}\Gamma_{\text{d}^-}\end{aligned} \tag{3.27}$$

$$\int_{\Gamma_d} \Psi \left((\boldsymbol{q}_{\Gamma_{d^+}} - \boldsymbol{q}_{\Gamma_{d^-}}) \cdot \boldsymbol{n}_d \right) \, d\Gamma_d + \int_{\Gamma_d} \Psi (\frac{\kappa_d}{\mu} \frac{\partial p_d}{\partial s}) \, d\Gamma_d + \int_{\Gamma_d} v_n \frac{\partial \Psi}{\partial s} (\frac{\kappa_d}{\mu} \frac{\partial p_d}{\partial s}) \, d\Gamma_d + \int_{\Gamma_d} \Psi \dot{v}_n \, d\Gamma_d + \int_{\Gamma_d} \Psi v_n \langle \frac{\partial \dot{v}_s}{\partial s} \rangle \, d\Gamma_d + \int_{\Gamma_d} \Psi \frac{v_n}{K_f} \dot{p}_d \, d\Gamma_d = \psi Q_{in} \tag{3.28}$$

where Q_{in} represents the fluid influx into the fracture. Applying the boundary conditions associated with the governing equations and utilising the auxiliary equations Eqs.(3.10), (3.22) and segregating the regular fields and the additional fields we obtain:

$$\int_{\Omega_e} \nabla \hat{\boldsymbol{\eta}} : \boldsymbol{\sigma} \, d\Omega_e = \int_{\Gamma_t} \hat{\boldsymbol{\eta}} \cdot \boldsymbol{t}_p \, d\Gamma_t \tag{3.29}$$

$$\int_{\Omega_e} H_{\Gamma_d} \nabla \tilde{\boldsymbol{\eta}} : \boldsymbol{\sigma} \, d\Omega_e = \int_{\Gamma_t} H_{\Gamma_d} \tilde{\boldsymbol{\eta}} \cdot \boldsymbol{t}_p \, d\Gamma_t - \int_{\Gamma_d} h \tilde{\boldsymbol{\eta}} \cdot (\boldsymbol{t}_d - p_d \boldsymbol{n}_d) \, d\Gamma_d \tag{3.30}$$

$$-\alpha \int_{\Omega_e} \hat{\xi} (\nabla \cdot \dot{\boldsymbol{u}}) \, d\Omega_e + \int_{\Omega_e} \nabla \hat{\xi} \cdot (-\frac{\kappa}{\mu} \nabla p) \, d\Omega_e - \int_{\Omega_e} \hat{\xi} \frac{\dot{p}}{M} \, d\Omega_e = + \int_{\Gamma_q} \hat{\xi} \, q_p \, d\Gamma_q - \int_{\Gamma_d} \hat{\xi} \, C_a (2p_d - p_f^+ - p_f^-) \, d\Gamma_d \tag{3.31}$$

$$-\alpha \int_{\Omega_e} H_{\Gamma_d} \tilde{\xi} (\nabla \cdot \dot{\boldsymbol{u}}) \, d\Omega_e + \int_{\Omega_e} H_{\Gamma_d} \nabla \tilde{\xi} \cdot (-\frac{\kappa}{\mu} \nabla p) \, d\Omega_e - \int_{\Omega_e} H_{\Gamma_d} \tilde{\xi} \frac{\dot{p}}{M} \, d\Omega_e = \int_{\Gamma_q} H_{\Gamma_d} \tilde{\xi} \, q_p \, d\Gamma_q - \int_{\Gamma_d} \tilde{\xi} C_a (H_{\Gamma_{d^+}} (p_d - p_f^+) + H_{\Gamma_{d^-}} (p_d - p_f^-)) \, d\Gamma_d \tag{3.32}$$

$$\int_{\Gamma_d} \Psi \, C_a (2p_d - p_f^+ - p_f^-) \, d\Gamma_d + \int_{\Gamma_d} \Psi \frac{\partial v_n}{\partial s} (\frac{v_n^2}{12\mu} \frac{\partial p_d}{\partial s}) \, d\Gamma_d + \int_{\Gamma_d} \frac{\partial \Psi}{\partial s} (\frac{v_n^3}{12\mu} \frac{\partial p_d}{\partial s}) \, d\Gamma_d + \int_{\Gamma_d} \Psi \dot{v}_n \, d\Gamma_d + \int_{\Gamma_d} \Psi v_n \langle \frac{\partial \dot{v}_s}{\partial s} \rangle \, d\Gamma_d + \int_{\Gamma_d} \Psi \frac{v_n}{K_f} \dot{p}_d \, d\Gamma_d = \psi Q_{in} \tag{3.33}$$

The last terms in right hand side of Eqs.(3.31),(3.32) represent the effect of fluid leak-off on the pore pressure in the porous formation, as presented in Eqs.(3.22),(3.21). This causes the local pressure in the vicinity of the fracture to increase and thereby making the pressure field continuous in case of highly permeable rocks.

3.4 Solution Methodology

3.4.1 Discretisation

In order to solve the coupled set of equations Eqs.(3.29) - (3.33), we need to discretise the field variables in both the space and time domains. The variables are discretised spatially, using the extended finite element method (Melenk and Babuška, 1996) with the help of shape functions, as follows:

$$\boldsymbol{u} = \boldsymbol{N}\hat{\boldsymbol{U}} + H_{\Gamma_\mathrm{d}}\boldsymbol{N}\tilde{\boldsymbol{U}} \qquad \boldsymbol{\eta} = \boldsymbol{N}\hat{\boldsymbol{\eta}} + H_{\Gamma_\mathrm{d}}\boldsymbol{N}\tilde{\boldsymbol{\eta}} \tag{3.34}$$

$$p = \boldsymbol{H}\hat{\boldsymbol{P}} + H_{\Gamma_\mathrm{d}}\boldsymbol{H}\tilde{\boldsymbol{P}} \qquad \xi = \boldsymbol{H}\hat{\boldsymbol{\xi}} + H_{\Gamma_\mathrm{d}}\boldsymbol{H}\tilde{\boldsymbol{\xi}} \tag{3.35}$$

$$p_\mathrm{d} = \boldsymbol{V}\boldsymbol{P}_\mathrm{d} \qquad \Psi = \boldsymbol{V}\boldsymbol{\Psi} \tag{3.36}$$

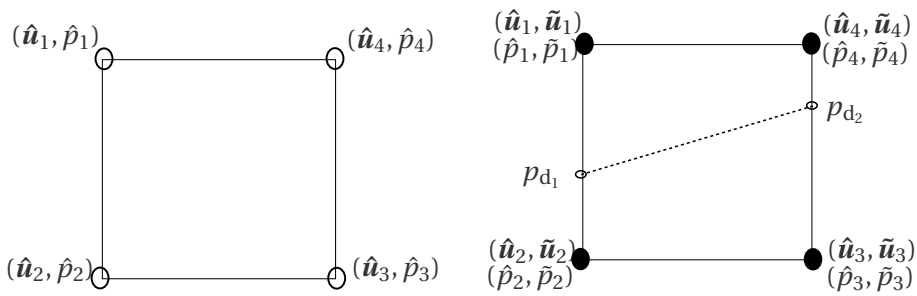

Figure 3.4: Degrees of freedom in a finite element a) without a discontinuity b) with a discontinuity

where $\boldsymbol{N}, \boldsymbol{H}, \boldsymbol{V}$ are the shape function matrices associated with displacement, pore pressure, enhanced local pressure respectively and $\hat{\boldsymbol{U}}, \tilde{\boldsymbol{U}}, \hat{\boldsymbol{P}}, \tilde{\boldsymbol{P}}$ are the vectors that represent the nodal values of displacement and pressure field variables respectively. $\boldsymbol{P}_\mathrm{d}$ is the field variable that represents the pressure inside the fracture. As seen in Figure.3.4, an element which contains a discontinuity has 4r+2 unknown nodal values whereas an element without a discontinuity has 2r unknown nodal values, where r is the number of nodes in the two-dimensional element . The admissible test functions are discretised with the same set of shape functions as the corresponding field variables. By substituting the discretised unknowns given by Eqs.(3.34) - (3.36) into Eqs.(3.29) - (3.33), we convert the set of differential equations into a set of algebraic equations. The discretised algebraic equations are written as:

$$\int_{\Omega_e} \boldsymbol{B}^\mathrm{T}\left(\boldsymbol{C}(\boldsymbol{B}\hat{\boldsymbol{U}} + H_{\Gamma_\mathrm{d}}\boldsymbol{B}\tilde{\boldsymbol{U}}) - \alpha \boldsymbol{m}^T(\boldsymbol{H}\hat{\boldsymbol{P}} + H_{\Gamma_\mathrm{d}}\boldsymbol{H}\tilde{\boldsymbol{P}})\right)\, \mathrm{d}\Omega_e - \int_{\Gamma_t} \boldsymbol{N}^T \boldsymbol{t}_\mathrm{p}\, \mathrm{d}\Gamma_t = 0 \tag{3.37}$$

$$\int_{\Omega_e} H_{\Gamma_d} \boldsymbol{B}^{\mathrm{T}} \left(\boldsymbol{C}(\boldsymbol{B}\hat{\boldsymbol{U}} + H_{\Gamma_\mathrm{d}} \boldsymbol{B}\tilde{\boldsymbol{U}}) - \alpha \boldsymbol{m}^T (\boldsymbol{H}\hat{\boldsymbol{P}} + H_{\Gamma_\mathrm{d}} \boldsymbol{H}\tilde{\boldsymbol{P}}) \right) \, \mathrm{d}\Omega_e - \int_{\Gamma_t} H_{\Gamma_d} \boldsymbol{N}^T \boldsymbol{t}_\mathrm{p} \, \mathrm{d}\Gamma_t + \int_{\Gamma_d} h \boldsymbol{N}^T (h \boldsymbol{T}_\mathrm{d} \boldsymbol{N}\tilde{\boldsymbol{U}} - \boldsymbol{V}\boldsymbol{P}_\mathrm{d} \boldsymbol{n}_\mathrm{d}) \, \mathrm{d}\Gamma_d = 0 \tag{3.38}$$

$$-\alpha \int_{\Omega_\mathrm{e}} \boldsymbol{H}^{\mathrm{T}} \boldsymbol{m}^{\mathrm{T}} (\boldsymbol{B}\dot{\hat{\boldsymbol{U}}} + H_{\Gamma_\mathrm{d}} \boldsymbol{B}\dot{\tilde{\boldsymbol{U}}}) \, \mathrm{d}\Omega_\mathrm{e} + \int_{\Gamma_\mathrm{d}} \boldsymbol{H}^{\mathrm{T}} \, C_\mathrm{a} (2\boldsymbol{V}\boldsymbol{P}_\mathrm{d} - 2\boldsymbol{H}\hat{\boldsymbol{P}} - (H_{\Gamma_{\mathrm{d}^+}} + H_{\Gamma_{\mathrm{d}^-}}) \boldsymbol{H}\tilde{\boldsymbol{P}}) \, \mathrm{d}\Gamma_\mathrm{d}$$
$$-\frac{\kappa}{\mu} \int_{\Omega_\mathrm{e}} \nabla \boldsymbol{H}^{\mathrm{T}} (\nabla \boldsymbol{H}\hat{\boldsymbol{P}} + H_{\Gamma_\mathrm{d}} \nabla \boldsymbol{H}\tilde{\boldsymbol{P}}) \, \mathrm{d}\Omega_\mathrm{e} - \frac{1}{M} \int_{\Omega_\mathrm{e}} \boldsymbol{H}^{\mathrm{T}} (\boldsymbol{H}\dot{\hat{\boldsymbol{P}}} + H_{\Gamma_\mathrm{d}} \boldsymbol{H}\dot{\tilde{\boldsymbol{P}}}) \, \mathrm{d}\Omega_\mathrm{e} = \int_{\Gamma_\mathrm{q}} \boldsymbol{H}^{\mathrm{T}} q_\mathrm{p} \, \mathrm{d}\Gamma_\mathrm{q} \tag{3.39}$$

$$-\alpha \int_{\Omega_\mathrm{e}} H_{\Gamma_\mathrm{d}} \boldsymbol{H}^{\mathrm{T}} \boldsymbol{m}^{\mathrm{T}} (\boldsymbol{B}\dot{\hat{\boldsymbol{U}}} + H_{\Gamma_\mathrm{d}} \boldsymbol{B}\dot{\tilde{\boldsymbol{U}}}) \, \mathrm{d}\Omega_\mathrm{e} - \frac{\kappa}{\mu} \int_{\Omega_\mathrm{e}} H_{\Gamma_\mathrm{d}} \nabla \boldsymbol{H}^{\mathrm{T}} ((\nabla \boldsymbol{H}\hat{\boldsymbol{P}} + H_{\Gamma_\mathrm{d}} \nabla \boldsymbol{H}\tilde{\boldsymbol{P}}) \, \mathrm{d}\Omega_\mathrm{e}$$
$$+ \int_{\Gamma_\mathrm{d}} H_{\Gamma_\mathrm{d}} \boldsymbol{H}^{\mathrm{T}} \, C_\mathrm{a} ((H_{\Gamma_{\mathrm{d}^+}} + H_{\Gamma_{\mathrm{d}^-}}) \boldsymbol{V}\boldsymbol{P}_\mathrm{d} - (H_{\Gamma_{\mathrm{d}^+}} + H_{\Gamma_{\mathrm{d}^-}}) \boldsymbol{H}\hat{\boldsymbol{P}} - (H^2_{\Gamma_{\mathrm{d}^+}} + H^2_{\Gamma_{\mathrm{d}^-}}) \boldsymbol{H}\tilde{\boldsymbol{P}}) \, \mathrm{d}\Gamma_\mathrm{d}$$
$$-\frac{1}{M} \int_{\Omega_\mathrm{e}} H_{\Gamma_\mathrm{d}} \boldsymbol{H}^{\mathrm{T}} (\boldsymbol{H}\dot{\hat{\boldsymbol{P}}} + H_{\Gamma_\mathrm{d}} \boldsymbol{H}\dot{\tilde{\boldsymbol{P}}}) \, \mathrm{d}\Omega_\mathrm{e} = \int_{\Gamma_\mathrm{q}} H_{\Gamma_\mathrm{d}} \boldsymbol{H}^{\mathrm{T}} q_\mathrm{p} \, \mathrm{d}\Gamma_\mathrm{q} \tag{3.40}$$

$$\int_{\Gamma_\mathrm{d}} \boldsymbol{V}^{\mathrm{T}} \, C_\mathrm{a} (2\boldsymbol{V}\boldsymbol{P}_\mathrm{d} - 2\boldsymbol{H}\hat{\boldsymbol{P}} - (H_{\Gamma_{\mathrm{d}^+}} + H_{\Gamma_{\mathrm{d}^-}}) \boldsymbol{H}\tilde{\boldsymbol{P}}) \, \mathrm{d}\Gamma_\mathrm{d} + \int_{\Gamma_\mathrm{d}} \frac{h}{K_\mathrm{f}} \boldsymbol{V}^{\mathrm{T}} \boldsymbol{n}_\mathrm{d} \boldsymbol{N}\tilde{\boldsymbol{U}} \boldsymbol{V}\dot{\boldsymbol{P}}_\mathrm{d} \, \mathrm{d}\Gamma_\mathrm{d}$$
$$+ \int_{\Gamma_\mathrm{d}} h \boldsymbol{V}^{\mathrm{T}} \boldsymbol{n}_\mathrm{d} \boldsymbol{N}\dot{\tilde{\boldsymbol{U}}} \, \mathrm{d}\Gamma_\mathrm{d} + \int_{\Gamma_\mathrm{d}} h \boldsymbol{V}^{\mathrm{T}} \boldsymbol{n}_\mathrm{d} \boldsymbol{N}\tilde{\boldsymbol{U}} \left(2\boldsymbol{s}_\mathrm{d} \frac{\partial \boldsymbol{N}}{\partial s} \dot{\hat{\boldsymbol{U}}} + (H_{\Gamma_{\mathrm{d}^+}} + H_{\Gamma_{\mathrm{d}^-}}) \boldsymbol{s}_\mathrm{d} \frac{\partial \boldsymbol{N}}{\partial s} \dot{\tilde{\boldsymbol{U}}} \right) \, \mathrm{d}\Gamma_\mathrm{d}$$
$$+ \int_{\Gamma_\mathrm{d}} \boldsymbol{V}^{\mathrm{T}} (h \boldsymbol{n}_\mathrm{d} \frac{\partial \boldsymbol{N}}{\partial s} \tilde{\boldsymbol{U}}) \frac{(h \boldsymbol{n}_\mathrm{d} \boldsymbol{N}\tilde{\boldsymbol{U}})^2}{12\mu} \frac{\partial \boldsymbol{V}}{\partial s} \boldsymbol{P}_\mathrm{d} \, \mathrm{d}\Gamma_\mathrm{d} + \int_{\Gamma_\mathrm{d}} \frac{\partial \boldsymbol{V}^{\mathrm{T}}}{\partial s} \frac{(h \boldsymbol{n}_\mathrm{d} \boldsymbol{N}\tilde{\boldsymbol{U}})^3}{12\mu} \frac{\partial \boldsymbol{V}}{\partial s} \boldsymbol{P}_\mathrm{d} \, \mathrm{d}\Gamma_\mathrm{d} = \boldsymbol{V}^{\mathrm{T}} Q_\mathrm{in} \tag{3.41}$$

where $\boldsymbol{m} = [1 \quad 1 \quad 0]^{\mathrm{T}}$ is introduced to account for the fact that the pore pressure coupling has an influence only on the normal stresses, $\boldsymbol{s}_\mathrm{d}$ represents the tangent to the fracture and $\boldsymbol{B}$ is the strain-displacement matrix which can be expressed as:

$$\boldsymbol{B} = \begin{bmatrix} \frac{\partial N_1}{\partial x} & 0 & \frac{\partial N_2}{\partial x} & 0 & . & . & . & \frac{\partial N_\mathrm{r}}{\partial x} & 0 \\ 0 & \frac{\partial N_1}{\partial y} & 0 & \frac{\partial N_2}{\partial y} & . & . & . & 0 & \frac{\partial N_\mathrm{r}}{\partial y} \\ \frac{\partial N_1}{\partial y} & \frac{\partial N_1}{\partial x} & \frac{\partial N_2}{\partial y} & \frac{\partial N_2}{\partial x} & . & . & . & \frac{\partial N_\mathrm{r}}{\partial y} & \frac{\partial N_\mathrm{r}}{\partial x} \end{bmatrix} \tag{3.42}$$

where r is the number of nodes in the two-dimensional element and N_i is the shape function for the corresponding nodes.

Time Discretisation: The system of equations contain time dependent terms hence we discretise the field variables with time and solve them in discrete time steps. This discretisation enables the variables in the equations to be described using their values at the current time step and the previous time step as:

$$(\cdot) = \bar{\theta}(\cdot)^{t+\triangle t} + (1-\bar{\theta})(\cdot)^{t} \tag{3.43}$$

The time derivative of the variables are obtained as:

$$\frac{\partial(\cdot)}{\partial t} = \frac{(\cdot)^{t+\triangle t} - (\cdot)^{t}}{\triangle t} \tag{3.44}$$

where $(\cdot)^{t+\triangle t}$ is the unknown solution at the current time step, $(\cdot)^{t}$ is the known solution at the previous time step, $\triangle t$ represents the time interval. Depending on the parameter $\bar{\theta}$, we obtain Euler's explicit method $\bar{\theta} = 0$ or Euler's implicit method $\bar{\theta} = 1$. In the remainder of this chapter, we use Euler's implicit method ($\bar{\theta} = 1$).

3.4.2 Solution

In order to solve these set of equations Eqs.(3.37) - (3.41), we make use of the Newton-Raphson iterative solver. The linearised form of the set of algebraic equations is represented as:

$$\begin{bmatrix} \boldsymbol{K}_{\hat{\mathrm{u}}\hat{\mathrm{u}}} & \boldsymbol{K}_{\hat{\mathrm{u}}\tilde{\mathrm{u}}} & \boldsymbol{K}_{\hat{\mathrm{u}}\hat{\mathrm{p}}} & \boldsymbol{K}_{\hat{\mathrm{u}}\tilde{\mathrm{p}}} & \boldsymbol{K}_{\hat{\mathrm{u}}\mathrm{p_d}} \\ \boldsymbol{K}_{\tilde{\mathrm{u}}\hat{\mathrm{u}}} & \boldsymbol{K}_{\tilde{\mathrm{u}}\tilde{\mathrm{u}}} & \boldsymbol{K}_{\tilde{\mathrm{u}}\hat{\mathrm{p}}} & \boldsymbol{K}_{\tilde{\mathrm{u}}\tilde{\mathrm{p}}} & \boldsymbol{K}_{\tilde{\mathrm{u}}\mathrm{p_d}} \\ \boldsymbol{K}_{\hat{\mathrm{p}}\hat{\mathrm{u}}} & \boldsymbol{K}_{\hat{\mathrm{p}}\tilde{\mathrm{u}}} & \boldsymbol{K}_{\hat{\mathrm{p}}\hat{\mathrm{p}}} & \boldsymbol{K}_{\hat{\mathrm{p}}\tilde{\mathrm{p}}} & \boldsymbol{K}_{\hat{\mathrm{p}}\mathrm{p_d}} \\ \boldsymbol{K}_{\tilde{\mathrm{p}}\hat{\mathrm{u}}} & \boldsymbol{K}_{\tilde{\mathrm{p}}\tilde{\mathrm{u}}} & \boldsymbol{K}_{\tilde{\mathrm{p}}\hat{\mathrm{p}}} & \boldsymbol{K}_{\tilde{\mathrm{p}}\tilde{\mathrm{p}}} & \boldsymbol{K}_{\tilde{\mathrm{p}}\mathrm{p_d}} \\ \boldsymbol{K}_{\mathrm{p_d}\hat{\mathrm{u}}} & \boldsymbol{K}_{\mathrm{p_d}\tilde{\mathrm{u}}} & \boldsymbol{K}_{\mathrm{p_d}\hat{\mathrm{p}}} & \boldsymbol{K}_{\mathrm{p_d}\tilde{\mathrm{p}}} & \boldsymbol{K}_{\mathrm{p_d}\mathrm{p_d}} \end{bmatrix} \begin{bmatrix} \triangle\hat{\boldsymbol{U}} \\ \triangle\tilde{\boldsymbol{U}} \\ \triangle\hat{\boldsymbol{P}} \\ \triangle\tilde{\boldsymbol{P}} \\ \triangle\boldsymbol{P}_{\mathrm{d}} \end{bmatrix} = \begin{bmatrix} \boldsymbol{f}^{\mathrm{ext}}_{\hat{\mathrm{u}}} \\ \boldsymbol{f}^{\mathrm{ext}}_{\tilde{\mathrm{u}}} \\ \triangle t\boldsymbol{f}^{\mathrm{ext}}_{\hat{\mathrm{p}}} \\ \triangle t\boldsymbol{f}^{\mathrm{ext}}_{\tilde{\mathrm{p}}} \\ \triangle t\boldsymbol{f}^{\mathrm{ext}}_{\mathrm{p_d}} \end{bmatrix} - \begin{bmatrix} \boldsymbol{f}^{\mathrm{int}}_{\hat{\mathrm{u}}} \\ \boldsymbol{f}^{\mathrm{int}}_{\tilde{\mathrm{u}}} \\ \boldsymbol{f}^{\mathrm{int}}_{\hat{\mathrm{p}}} \\ \boldsymbol{f}^{\mathrm{int}}_{\tilde{\mathrm{p}}} \\ \boldsymbol{f}^{\mathrm{int}}_{\mathrm{p_d}} \end{bmatrix} \tag{3.45}$$

Using a monolithic solver, the unknown field variables $\left(\boldsymbol{X} = [\ \hat{\boldsymbol{U}}\ \ \tilde{\boldsymbol{U}}\ \ \hat{\boldsymbol{P}}\ \ \tilde{\boldsymbol{P}}\ \ \hat{\boldsymbol{P}}_d\ ]^T\right)$ are solved simultaneously at all the nodes for every time step by using their values at previous time step and their increment as $\boldsymbol{X}^{t+\triangle t} = \boldsymbol{X}^{t} + \triangle\boldsymbol{X}$. The external and internal force matrices are represented by $\boldsymbol{f}^{\mathrm{ext}}$ and $\boldsymbol{f}^{\mathrm{int}}$ respectively. The definition of all the co-efficient and force matrices are described in the Appendix. For further details on the implementation of the numerical model we refer to Remmers et al. (2003); Remmers (2006) and Wells and Sluys (2001).

3.5 Numerical Examples

In this section, we look at three different test cases to validate and demonstrate the working of the modified enhanced local pressure model. For validation of

the model we consider a simple consolidation problem (Terzaghi, 1925) which has an analytical solution for the benchmarking and a hydraulic fracture problem for near impermeable rocks which enables the comparison with the ELP solution. To demonstrate the improvement of the model we look at the same hydraulic fracture problem for permeable rocks and a fracture network problem to analyse the effect of the improved leak-off model on fracture interactions.

3.5.1 Consolidation Problem

In the example shown in Figure 3.5 we consider a thin long column with dimensions of 20000 mm × 50 mm with no-flow boundary conditions along its length. We consider an open fracture at the middle of the column with the fracture surfaces fixed at 0.02 mm apart from each other. The fracture is injected with a constant fluid flow of $5.0 \times 10^{-6}\mathrm{m}^2/\mathrm{s}$ for a time period of 4 seconds from the right edge. The fracture is assumed to be filled with fluid and no flow conditions on the other edge of the fracture ensures that all of the injected fluid leaks off into the formation. The Young's modulus and Poisson's ratio of the formation are assumed to be 20 GPa and 0.2 respectively with a porosity of 0.2. The bulk modulus of the solid grains is assumed to be 36 GPa while the fluid in the porous medium has bulk modulus and viscosity of 3 GPa and 0.01 $Pa \cdot s$, respectively. The time step of the simulation is 0.02 s. The long column is discretised with a mesh consisting of standard quadrilateral elements with a size of 1 mm × 50 mm for both the permeable and the near impermeable rocks.

One half of the column can be assumed to be a semi-infinite consolidation problem with a constant flux at one end. This problem can be analytically solved by using the 1-D Terzaghi consolidation equation (Terzaghi, 1925) and the pore pressure in the formation can be obtained from Carslaw and Jaeger (1959) as :

$$p(y,t) = \frac{2Q_{\mathrm{flux}}\mu}{\kappa}\left(\sqrt{\frac{c_{\mathrm{v}}t}{\pi}}\,\exp\left(\frac{-\mathrm{y}^2}{4\mathrm{c_v t}}\right) - \frac{\mathrm{y}}{2}\,\mathrm{erfc}\left(\frac{\mathrm{y}}{2\sqrt{\mathrm{c_v t}}}\right)\right) \tag{3.46}$$

where y indicates the distance from the discontinuity in the vertical direction and c_{v} is the co-efficient of consolidation. The Q_{flux} in our problem is obtained as $5.0 \times 10^{-5}\mathrm{m/s}$ by splitting the flow for one half along the fracture length. We compare the MELP and ELP solutions against the benchmark analytical solutions for two different permeabilities. In the first case for near impermeable rocks with a permeability of $\kappa = 10^{-19}\mathrm{m}^2$, we can observe that both the MELP and ELP models can capture the pressure in the fracture (Figure 3.7) and a steep pressure gradient in the formation, Figure 3.6(a), is represented as a discontinuity in both the numerical models.

In the second case for permeable rocks with a permeability of $5 \times 10^{-14}\mathrm{m}^2$, we can clearly see that the MELP model is able to capture the pore pressure in

the formation (Figure 3.6(b)) and also accurately obtain the pressure inside the discontinuity (Figure 3.8). We can also observe that the pressures are continuous from the fracture to the formation. This is due to the fact that the MELP model takes into account the effect of leak off on the flow inside the fracture and also coupled the leak off with the pressure in the formation.

Vermeer and Verruijt (1981) derived the stability criterion for the accurate modelling of a consolidation problem using finite element methods. This criterion gives the consolidation distance for a single time step as: $\triangle x_{\text{cons}} = \sqrt{\triangle t\ E\ \kappa/\mu}$. By substituting the known variables, we observe that the consolidation distance for near impermeable rocks is 0.0632 mm while that for permeable rocks is 44.7 mm. The height of a single element needs to be lower than this consolidation distance for accuracy. We use a uniform mesh with a element height of 1 mm for both the models. We can observe from Figure 3.7b, that the MELP model obtains the pressure in the discontinuity with a relative error of < 3% even when we violate the criteria proposed by Vermeer and Verruijt (1981). Thereby we eliminate the need for a very fine mesh in case of

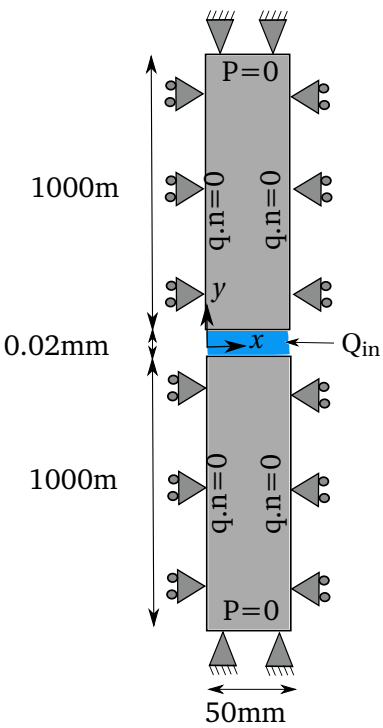

Figure 3.5: Long column with an open fracture

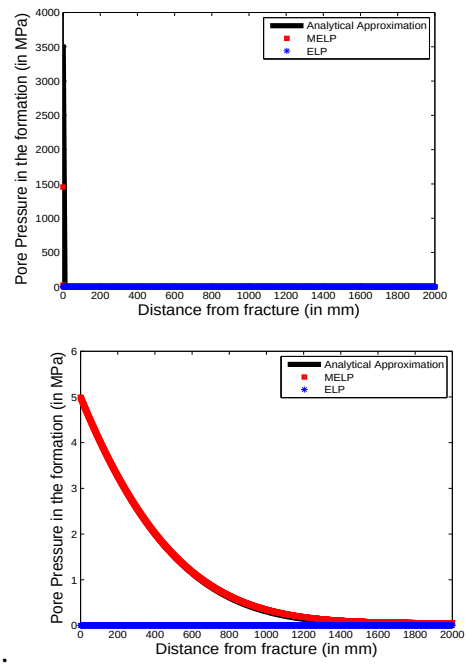

Figure 3.6: Pore Pressure distribution for near impermeable rocks ($\kappa = 10^{-19}\text{m}^2$) (top) and permeable rocks ($\kappa = 5 \times 10^{-14}\text{m}^2$) (bottom) after injection for 4 seconds.

near impermeable rocks. We also observe from Figure 3.8b, that the relative error reduces significantly when the consolidation distance is greater than the element height.

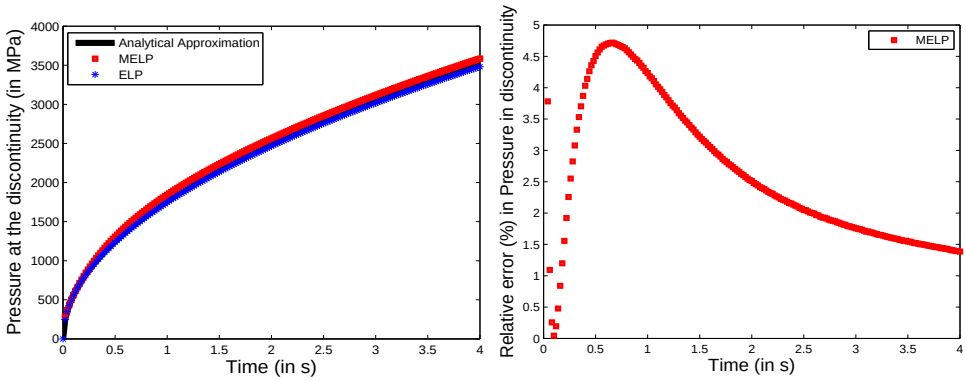

(a) (b)

Figure 3.7: Pressure in the discontinuity in near impermeable rocks ($\kappa = 1 \times 10^{-19}\text{m}^2$) for a 1-D consolidation problem

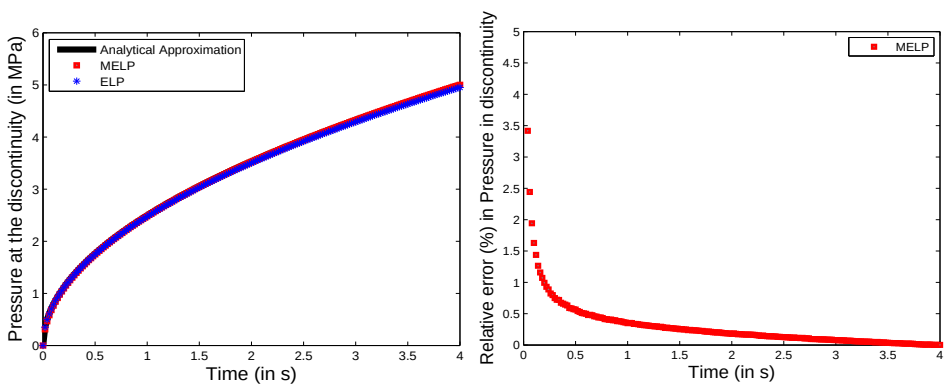

(a) (b)

Figure 3.8: Pressure in the discontinuity in permeable rocks ($\kappa = 5 \times 10^{-14}\text{m}^2$) for a 1-D consolidation problem

3.5.2 Single hydraulic fracture

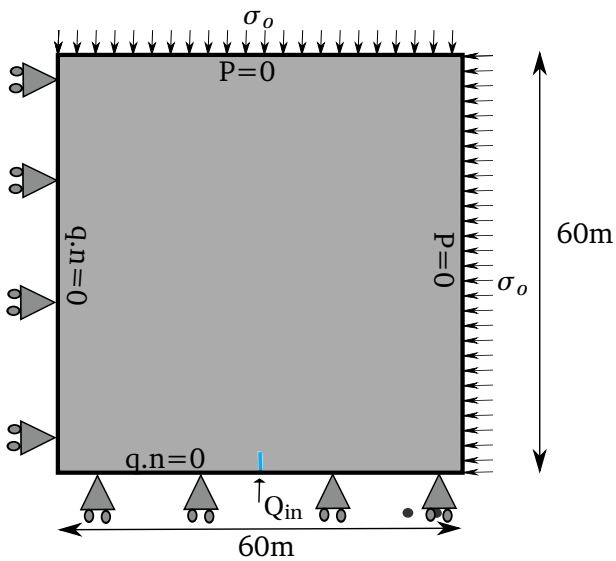

Figure 3.9: Vertical KGD problem

In this example, we consider a rock formation as shown in Figure 3.9 with an initial fracture opening at the bottom where fluid is injected at the rate of $6.0\times10^{-4}\mathrm{m}^2/\mathrm{s}$ for 20 seconds with a time step of 0.1s. The Young's modulus and Poisson's ratio of the rock are 20 MPa and 0.2 respectively. The ultimate tensile and shear strength are assumed to be 6 MPa and 60 MPa respectively with a toughness of 120 N/m. The in-situ stresses are considered to be 40 MPa both in the vertical and the horizontal direction. The formation is assumed to have has a porosity of 0.1 and a fluid viscosity of 0.001 $Pa{\cdot}s$. The mesh in the region surrounding the fracture consists of standard quadrilateral elements with a size of 50 mm × 50 mm for both the permeable and the near impermeable rocks.

The ELP model proposed by Remij et al. (2015a) is considered for benchmarking, as it is accurate for near impermeable rocks. As observed in Figure 3.10, the fracture propagation characteristics are similar in both the MELP and ELP models for near impermeable rocks, such as shales, with a permeability of $10^{-19}\mathrm{m}^2$. This is due to the fact that the fluid leak off is extremely low in these rocks which renders leak off - pore pressure coupling effect to be negligible. In this case the leak off is observed to be less than 5 % by both MELP and ELP models.

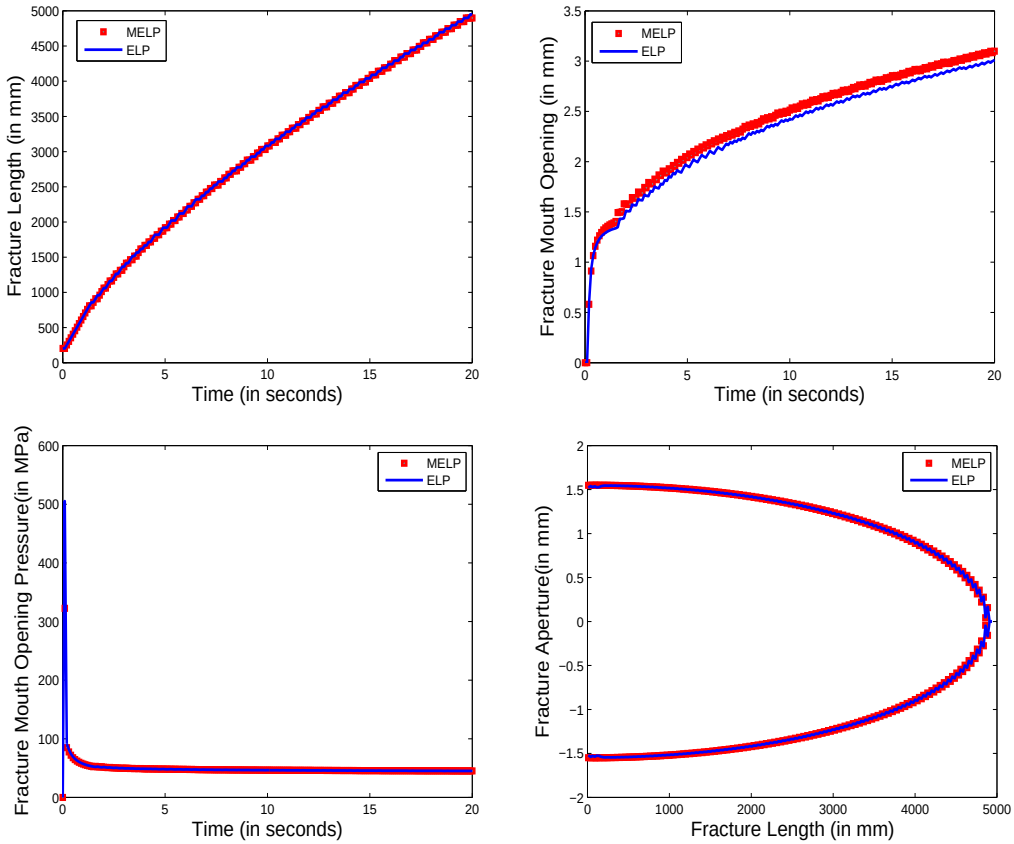

Figure 3.10: Comparison of MELP Vs ELP models for a single hydraulic fracture propagation in near impermeable rocks

The same hydraulic fracture problem is considered for permeable rocks, such as sandstones, which have a permeability of 10^{-15}m^2. As we observe in Figure 3.11, the MELP model predicts a higher fracture length and a lower width compared to the ELP model but the pressure inside the fracture remains constant in both models. In order to understand the reason for this variation, we plot the pore pressure in the formation along a plane which is perpendicular to the fracture after 20 seconds. In Figure 3.12a, we observe that the MELP model successfully resolves the pore pressure in the formation causing a much more smoother transition from formation to fracture which the ELP model fails. This pore pressure distribution has two major consequences: a) It modifies stress state closer to the existing fracture surfaces causing more compressive stress and as a result the fracture width is lower. b) It results in much lower leak off in the MELP model (40% of total fluid volume injected in MELP Vs ~ 60% in ELP) as observed in Figure 3.12b. This causes more fluid to be available for fracture propagation and hence an increase in length in the MELP model.

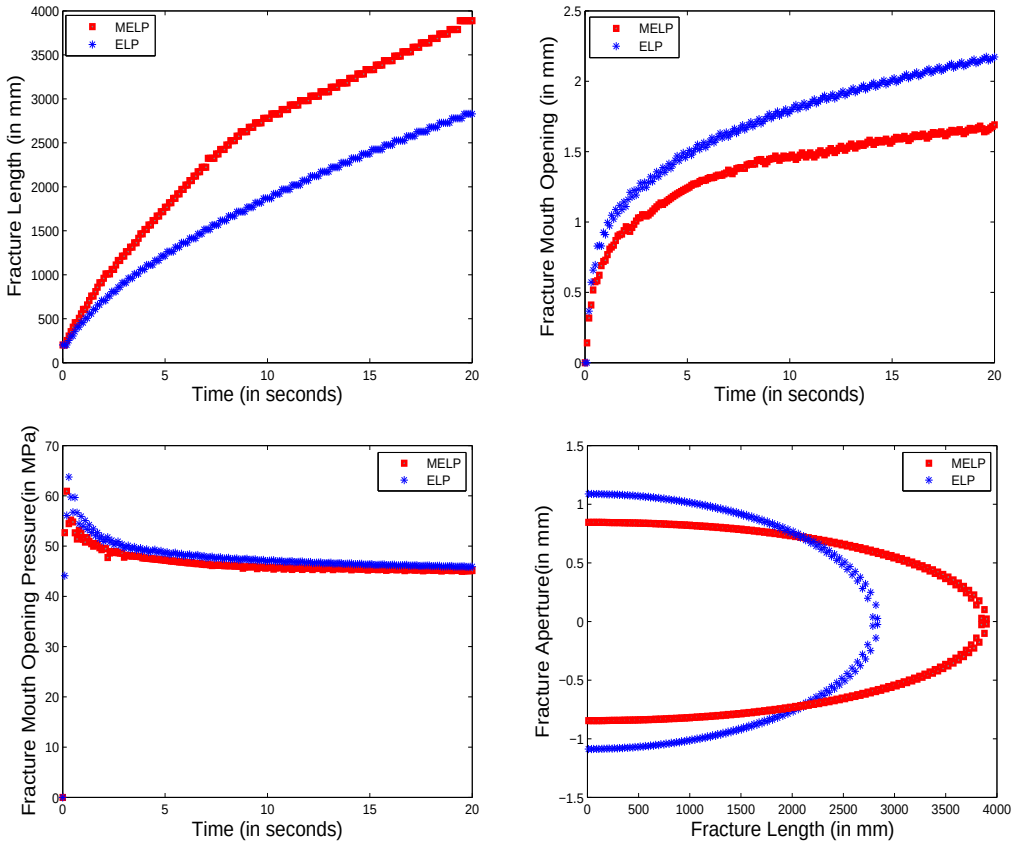

Figure 3.11: Comparison of MELP Vs ELP models for a single hydraulic fracture propagation in permeable rocks

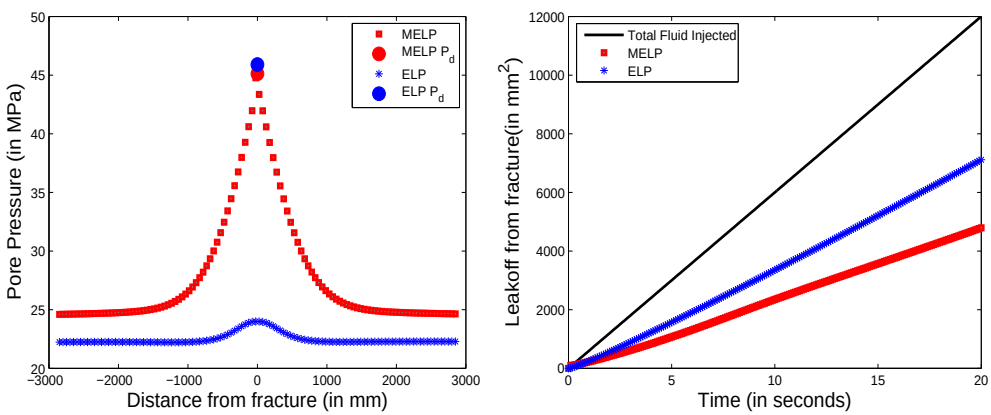

(a) (b)

Figure 3.12: For a single hydraulic fracture problem: (a)Pore Pressure distribution in a plane across the fracture for ELP and MELP models. The circular dots indicate the pressure inside the fracture. (b) Cumulative Leak-off with time for MELP and ELP models. The black line indicates the total volume of fluid injected inside the fracture

3.5.3 Cluster of hydraulic fractures

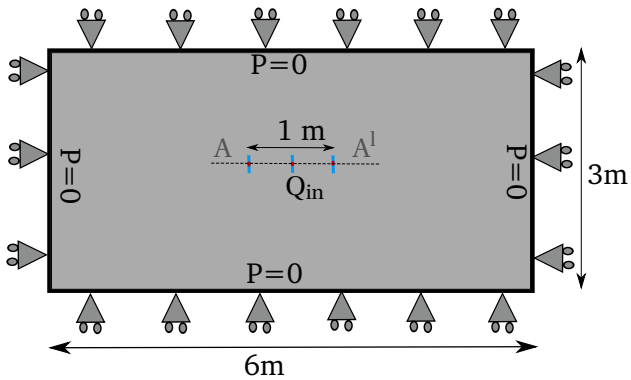

Figure 3.13: Cluster of hydraulic fractures

Hydraulic fracturing in reservoirs are conducted in several stages with each stage consisting of several fractures which are essential for forming a fracture network. Hence in this example (Figure 3.13) we try to understand the differences between MELP and ELP models on a cluster of fractures. In this test case, we consider a model with three initial fractures in the formation separated by a distance of 0.5 m from each other. The boundaries are assumed to have free drainage. The fractures are injected at the rate of $5.0 \times 10^{-5} \mathrm{m}^2/\mathrm{s}$ for 10 seconds. The Young's modulus and Poisson's ratio are 20 Gpa and 0.2 respectively while the ultimate tensile strength and toughness of the rock formation are 4 MPa and 120 N/m. The formation is assumed to have a porosity of 0.1 and a fluid viscosity of 0.001 $Pa \cdot s$. We consider two different permeabilities of $10^{-20}\mathrm{m}^2$ for near impermeable rocks and $10^{-14}\mathrm{m}^2$ for permeable rocks. The time step for the simulation is assumed to be 0.1s. The mesh in the region surrounding the fractures consists of standard quadrilateral elements with a size of 50 mm × 50 mm for both the permeable and the near impermeable rocks.

From Figure 3.14 we can observe that the fracture network obtained from MELP and ELP models for near impermeable rocks, such as shales, are almost similar with small differences in the stress contours. The fractures at the ends propagate further when compared to the fracture in the middle due to the stress shadowing effect (Sobhaniaragh et al., 2016). Due to the propagation of fractures at the end, a compressive stress field is created ahead of the tip of the centre fracture thereby stunting its growth.

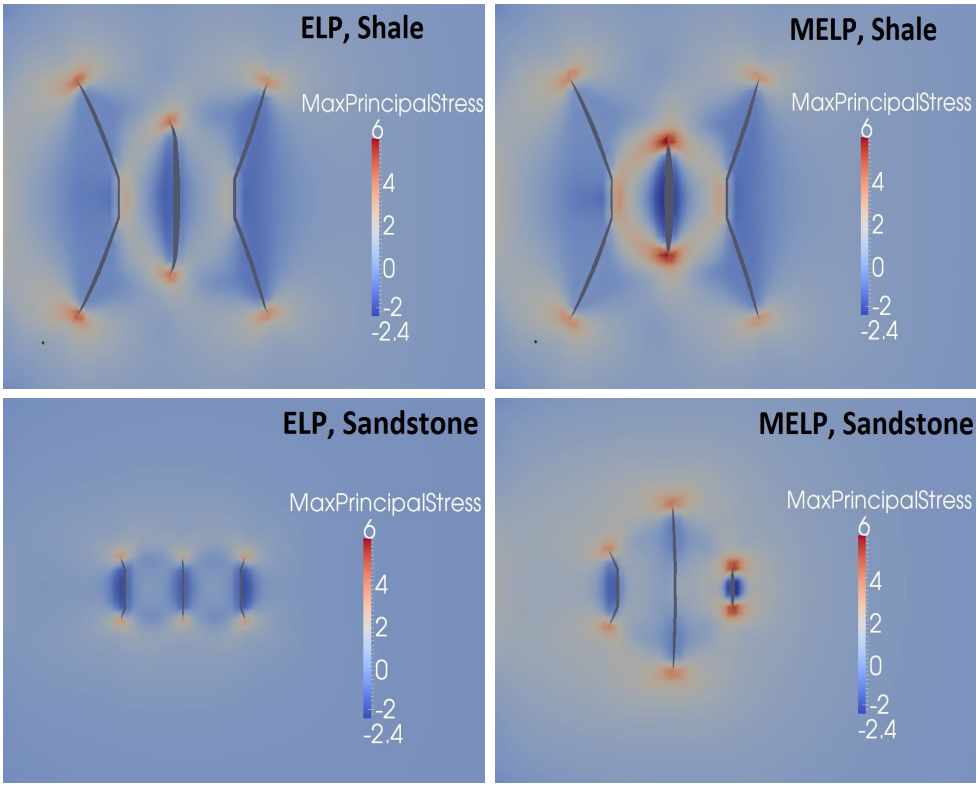

Figure 3.14: Stress contour plots for a cluster of three fractures after 5 seconds (Top) Comparison between ELP and MELP models in near impermeable rocks ($\kappa = 10^{-20}\text{m}^2$) (Bottom) Comparison between ELP and MELP models in permeable rocks ($\kappa = 10^{-14}\text{m}^2$). The deformed configurations are magnified 200 times

For permeable rocks, the fracture patterns vary drastically between ELP and MELP models. The ELP model predicts that the fractures hardly grow while the MELP model shows that the centre fracture propagates much further. In Figure 3.15a, we can see the pore pressure distribution along a plane AA' which passes through the injection point of all the three fractures. The fractures in the ELP model are not able to propagate inspite of pressure build-up at the middle of the fractures due to the fact that almost 90 % of the total injected fluid (Figure 3.15b) is lost in leak off thereby not having enough fluid pressure at the tip. This is due to the fact that the ELP model assumes that the consolidation process happening due to the leak-off from the three fractures are mutually independent.

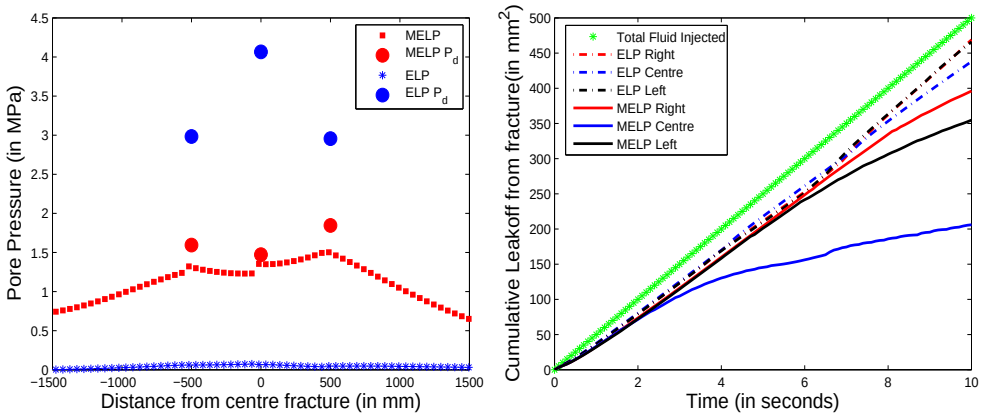

(a) (b)

Figure 3.15: For a cluster of hydraulic fractures problem: (a)Pore Pressure distribution in a plane AA' across the fractures after 10 seconds for ELP and MELP models. The circular dots indicate the pressure inside the fractures. (b) Cumulative Leak-off from the three fractures for MELP and ELP models. The green line indicates the total volume of fluid injected inside each fracture

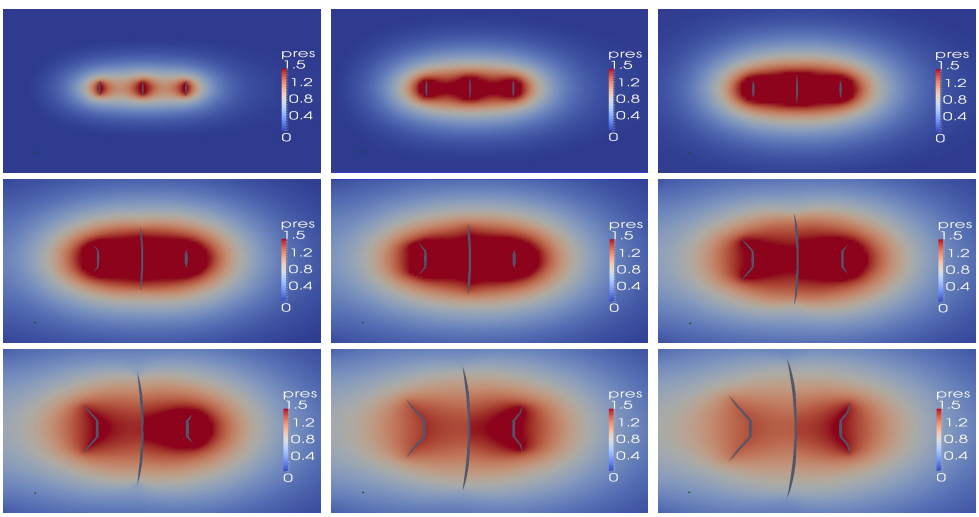

Figure 3.16: Evolution of fracture network with time using MELP model in permeable rocks

From Figure 3.16, we can observe the evolution of the fracture network with time in permeable rocks for MELP model. All the fractures leak fluid from the fracture into the formation initially. After a certain time this causes a build-up of pore pressure in formation in the region surrounding the fractures which

in turn yields a pore pressure plateau in the central region between the two end fractures as observed in Figure 3.15a. This plateau causes the pressure gradient in this region to be very low, thereby significantly lowering the leak off from the central fracture as seen in Figure 3.15b. This leads to further propagation of the central fractures contrary to the pattern observed in MELP model for near impermeable rocks.

3.6 Conclusion

From the numerical examples, we can conclude that the ELP model (Remij et al., 2015a) is less suitable for modelling the fractures and their interactions in rocks with significant permeability while it works well for near impermeable rocks where the leak-off has negligible effect on the pore pressure in the adjacent formation. The conventional fully coupled models (Mohammadnejad and Khoei, 2013; Fan et al., 1995; Yang et al., 2016) can accurately model the fracture and its interactions in permeable rocks and have a continuous pressure profile from the fracture to the formation, but they would require an extremely fine mesh (Vermeer and Verruijt, 1981) to resolve the consolidation process in near impermeable rocks. Hence the MELP model combines the advantages of both these approaches to form a model which tends to behave similar to the ELP model for near impermeable rocks with a discontinuous pressure profile. While for permeable rocks the behaviour of MELP model is similar to the conventional fully coupled models with the pressure profile approaching continuity when there are enough elements to resolve the consolidation process.

Chapter 4

Effect of anisotropy on hydraulic fractures

Abstract

In this chapter, we present a two-dimensional numerical model for modelling of hydraulic fracturing in anisotropic media. The numerical model is based on eXtended Finite Element Method (XFEM). The saturated porous media is modelled using Biot's theory of poroelasticity. An enhanced local pressure (ELP) model is used for modelling the pressure within the fracture, taking into account the external fluid injection and the leak-off. Directional dependence of all the rock properties, both elastic and flow related, are taken into account. A combination of the Tsai-Hill failure criterion and Camacho-Ortiz propagation criterion is proposed to determine the fracture propagation. We study the impact on fracture propagation (in both magnitude and direction) due to anisotropies induced by various parameters, namely ultimate tensile strength, Young's modulus, permeability and overburden pressure. The influence of several combinations of all these anisotropies along with different grain orientation and initial fracture directions on the fracture propagation direction are studied. Different regimes are identified where the fracture propagation direction is controlled by the degree of material anisotropy instead of the stress anisotropy.

Reproduced from: Valliappan, V., Remmers, J. J. C., Barnhoorn, A., & Smeulders, D. M. J. (2019). A Numerical Study on the Effect of Anisotropy on Hydraulic Fractures. Rock Mechanics and Rock Engineering, 52(2), pp.591-609.

4.1 Introduction

The first numerical models for modelling hydraulic fracturing were developed by Boone and Ingraffea (1990) using finite elements for modelling the formation and using finite volume for modelling flow with cohesive zones along element edges describing the fractures. In recent times there have been several models developed based on different numerical techniques. A linear elastic fracture mechanics (LEFM) based finite element model (FEM) was proposed by Hossain and Rahman (2008). To avoid the singularity problems at the crack tip in LEFM, FEM models with zero-thickness elements (describing the fractures using cohesive zones) were developed (Carrier and Granet, 2012; Chen, 2012). The FEM approach requires re-meshing to capture the fracture propagation accurately, whereas extended finite element (XFEM) based models allows for fracture propagation in arbitrary directions without the need for re-meshing (Mohammadnejad and Khoei, 2013; Remij et al., 2015a; Meschke and Leonhart, 2015). A novel approach in which the asymptotic behaviour near the fracture tip was resolved with extended finite element method (Gordeliy and Peirce, 2013a,b, 2015). An alternate approach based on phase field modelling which combines FEM with continuum damage mechanics has been developed (Mikelic et al., 2015; Mikelić et al., 2015; **?**; **?**) which provides a convenient way for modelling complex fracture interactions. But all the above hydraulic fracture models assume the rock formation to be isotropic in nature.

Most rocks (especially shales, which is the most common rock type to be hydraulic fractured) are highly anisotropic in nature (Jaeger et al., 2009; Barton, 2007). Kaarsberg (1959) and Sayers (1994) observed that shales have a plane along which the grains are oriented causing the properties along the grain direction to be vastly different from the properties perpendicular to the grain direction. This causes a special type of anisotropy, called transverse isotropy where the material properties in any direction in the plane can be obtained by using the material properties along any two mutually perpendicular set of directions in that plane. Although there are several studies (Abousleiman et al., 2008; Zhubayev et al., 2015) experimentally obtaining the anisotropic parameters, there are few papers by Cheng (1997) analytically deriving the anisotropic poro-elastic co-efficients. Abousleiman et al. (1996) modelled the deformation and pressure in a transversely isotropic porous medium without any fracture. Porous material with a stress driven fracture in an orthotropic media was modelled by Remij et al. (2015b). More recently the influence of rock anisotropy on tensile fractures was studied experimentally by Mighani et al. (2016).

In this chapter, we enhance the aforementioned XFEM model by Remij et al. (2015a) to include the effects of anisotropy on hydraulic fracturing. Using the model we analyse the effect of anisotropic rock properties (Young's modulus, ultimate tensile strength and permeability) on the fluid driven fracture propa-

gation and also the impact when combined with loading.

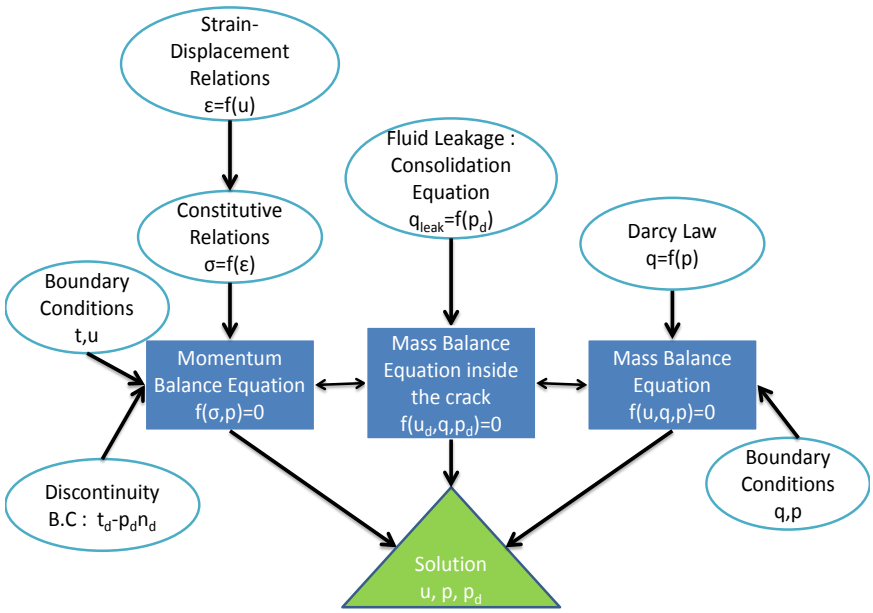

Figure 4.1: Solution procedure for poro-elastic fracture problem.

4.2 Mathematical formulation

In order to solve a poro-elastic problem, we need to solve for the solid deformation ($\mathbf{u}$) and fluid pressure (p) at all points within the porous media. Biot's theory of poroelasticity (Biot, 1941) is used to describe the porous media and fluid flow is described using Darcy's law. The porous media is assumed to be saturated.

In addition for the hydraulic fracture problem, we make use of an enhanced local pressure (ELP) as proposed by Remij et al. (2015a) to model the pressure inside the fracture at all points along the fracture length. This additional degree of freedom (p_{d}) enables us to model the complicated phenomenon happening within the fracture, namely the injection of external fluid, moving boundaries of fracture surface and the leak-off. Leak-off from fracture to formation is described using the 1-D Terzaghi consolidation equation (Terzaghi, 1925).

For solving the unknowns, a set of governing equations along with auxiliary equations are used. The governing equations used to describe the poro-elastic problem are of two types: solid deformation based momentum balance and fluid flow based mass balance. We consider an additional equation to ensure

the mass balance inside the fracture. The auxiliary equations are used for relating these governing equations with the unknowns and also for coupling them. A schematic flow chart of the mathematical formulation is represented in Figure 4.1.

A schematic of a body Ω with a discontinuity Γ_d, which splits the body into two domains Ω^+ and Ω^-, along with prescribed boundary conditions is represented in Figure 4.2.

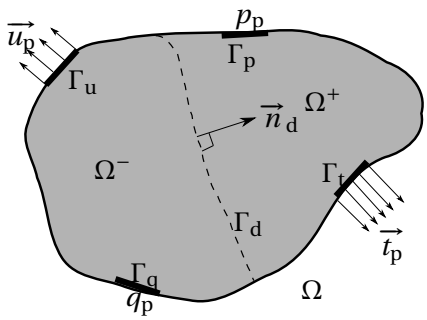

Figure 4.2: Schematic of a domain Ω with discontinuity Γ_d.

4.3 Implementation

4.3.1 Discretisation

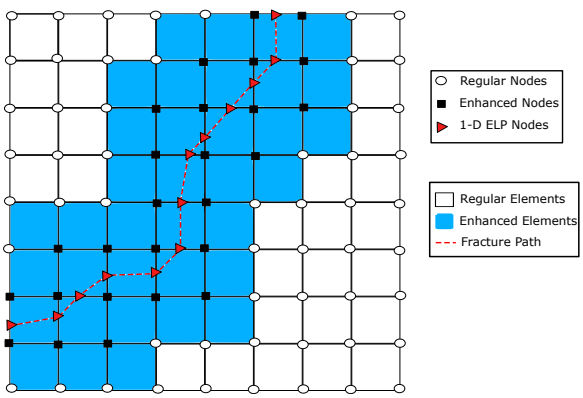

Figure 4.3: Discretisation in XFEM.

We need a numerical method in order to solve the set of coupled differential equations and also incorporate the discontinuous jump in various parameters due to the fracture. Hence, we make use of XFEM which models the discontinuous jump due to fractures by using additional degrees of freedom. XFEM allows for the fracture to propagate through the elements, thus ensuring accuracy in

capturing the fracture even with a coarse mesh making it computationally very efficient. Similar to traditional FEM, the unknowns are obtained at certain control points (nodes) by solving the differential equation and the unknowns in the intermediate regions are obtained by interpolation using shape functions. The discretised form of the unknown displacement and pressure in a porous media intersected by the fracture is expressed as:

$$\boldsymbol{u} = \boldsymbol{N}\hat{\boldsymbol{U}} + H_{\Gamma_\mathrm{d}}\boldsymbol{N}\tilde{\boldsymbol{U}} \quad \text{when} \quad \mathrm{x} \notin \Gamma_\mathrm{d} \tag{4.1}$$

$$p = \boldsymbol{L}\hat{\boldsymbol{P}} + H_{\Gamma_\mathrm{d}}\boldsymbol{L}\tilde{\boldsymbol{P}} \quad \text{when} \quad \mathrm{x} \notin \Gamma_\mathrm{d} \tag{4.2}$$

$$p_\mathrm{d} = \boldsymbol{V}\hat{\boldsymbol{P}}_\mathrm{d} \quad \text{when} \quad \mathrm{x} \in \Gamma_\mathrm{d} \tag{4.3}$$

where H_{Γ_d} is the Heaviside step function, given as:

$$H_{\Gamma_\mathrm{d}} = \begin{cases} 1 & \text{when} \quad \mathrm{x} \in \Omega^+ \\ 0 & \text{when} \quad \mathrm{x} \in \Omega^- \end{cases} \tag{4.4}$$

$\hat{\boldsymbol{U}}$ and $\hat{\boldsymbol{P}}$ represent the regular nodal degrees of freedom for displacement and pressure respectively while $\tilde{\boldsymbol{U}}$ and $\tilde{\boldsymbol{P}}$ represent the enhanced nodal degrees of freedom representing the discontinuous jump in displacement and pressure across the fracture. $\hat{\boldsymbol{P}}_\mathrm{d}$ represents the pressure inside the fracture at points where the fracture intersects the element edges. $\boldsymbol{N}$, $\boldsymbol{L}$ are two dimensional interpolation or shape functions for the displacement and pressure fields whereas $\boldsymbol{V}$ is a one-dimensional shape function for interpolation of the pressure along the fracture length.

4.3.2 Solution

The governing equations are combined with the auxiliary equations as shown in Figure 4.1. Weak form of this set of equations are obtained by integrating them along with a test function. By substituting the discretised unknowns given by Equations (4.1), (4.2) and (4.3) into the weak form, we convert the set of differential equations into a set of algebraic equations. In order to solve this set of equations simultaneously, we make use of the Newton-Raphson iterative solver in combination with Euler's forward scheme for obtaining the time derivative, and Euler's implicit scheme for time independent parameters. A detailed description of the solution procedure is given in Remij et al. (2015a).

The unknown $\left(\boldsymbol{X} = [\ \hat{\boldsymbol{U}}\ \ \tilde{\boldsymbol{U}}\ \ \hat{\boldsymbol{P}}\ \ \tilde{\boldsymbol{P}}\ \ \hat{\boldsymbol{P}}_\mathrm{d}\ ]^T\right)$ degrees of freedom are solved at each grid point (nodes) for every time step.

4.3.3 Propagation

A propagation criterion is needed in order to determine the propagation initiation and also the magnitude and direction of propagation. Hence we make

use of the Camacho-Ortiz criterion (Camacho and Ortiz, 1996) which can be used for mixed mode fractures as well. This criterion states the condition for fracture propagation as:

$$t_{\mathrm{eq}} > 1 \quad \text{where} \quad t_{\mathrm{eq}} = \sqrt{\frac{t_{\mathrm{n}}^2}{\tau_{\mathrm{ult}}^2} + \frac{t_{\mathrm{s}}^2}{S_{\mathrm{ult}}^2}} \tag{4.5}$$

where t_{eq} is the equivalent traction ratio in a specific direction, τ_{ult} and S_{ult} represent the ultimate tensile and shear strength of the porous media, respectively, t_{n} and t_{s} are the normal and shear tractions along that orientation which are obtained from average stresses as:

$$t_{\mathrm{n}} = \begin{cases} \boldsymbol{n}^T \boldsymbol{\sigma}_{\mathrm{av}} \boldsymbol{n} & \text{if} \quad \boldsymbol{n}^T \boldsymbol{\sigma}_{\mathrm{av}} \boldsymbol{n} > 0 \\ 0 & \text{if} \quad \boldsymbol{n}^T \boldsymbol{\sigma}_{\mathrm{av}} \boldsymbol{n} < 0 \end{cases} \tag{4.6}$$

$$t_{\mathrm{s}} = \begin{cases} \boldsymbol{s}^T \boldsymbol{\sigma}_{\mathrm{av}} \boldsymbol{n} & \text{if} \quad \boldsymbol{n}^T \boldsymbol{\sigma}_{\mathrm{av}} \boldsymbol{n} > 0 \\ \boldsymbol{s}^T \boldsymbol{\sigma}_{\mathrm{av}} \boldsymbol{n} - \Psi(\boldsymbol{n}^T \boldsymbol{\sigma}_{\mathrm{av}} \boldsymbol{n}) & \text{if} \quad \boldsymbol{n}^T \boldsymbol{\sigma}_{\mathrm{av}} \boldsymbol{n} < 0 \end{cases} \tag{4.7}$$

where Ψ is the coefficient of friction, and $\boldsymbol{n}$ and $\boldsymbol{s}$ are the unit normal and tangent vector to the direction. $\boldsymbol{\sigma}_{\mathrm{av}}$ is the average stress, used to obtain a better approximation of the stress state in the vicinity of the fracture tip. The average stresses are obtained by assigning weight functions to the Gaussian integration points within a certain distance (generally three times the characteristic element length) from the fracture tip, as derived by Jirasek (1998). As an averaged stress is used, this may lead to a slight delay in the onset of fracture propagation.

The direction of propagation is taken to be the direction in which the equivalent traction is maximum. The fracture is assumed to propagate through the entire element length in a single time step in a straight line. Further details on the implementation of the solution are described by Remmers (2006); Remmers et al. (2003).

4.4 Anisotropic parameters

In this section, we highlight the parameters which need to be modified to incorporate the effect of anisotropy.

4.4.1 Constitutive relation

The effective elastic stress ($\boldsymbol{\sigma}_{\mathrm{e}}$) in the solid grain is related to the elastic strain by means of the generalised Hooke's law.

$$\boldsymbol{\sigma}_{\mathrm{e}} = \boldsymbol{C}\boldsymbol{\epsilon} \tag{4.8}$$

where $\boldsymbol{C}$ is the constitutive relationship matrix and $\boldsymbol{\epsilon}$ is the elastic strain in the solid grains.

The coefficients of the constitutive matrix depend on the material type and geometrical assumptions. The constitutive relation matrix can be obtained as the inverse of the compliance matrix, $\boldsymbol{C} = \boldsymbol{S}^{-1}$. We assume a plane strain case with a transverse isotropic material for which the compliance matrix in the grain direction is given as:

$$\boldsymbol{S}_{local} = \begin{bmatrix} \frac{(E_\perp - E_\parallel \nu_{\text{in}}^2)}{E_\parallel E_\perp} & \frac{-(\nu_{\text{in}} + \nu_{\text{in}}\nu_{\text{out}})}{E_\perp} & 0 \\ \frac{-(\nu_{\text{in}} + \nu_{\text{in}}\nu_{\text{out}})}{E_\perp} & \frac{(1-\nu_{\text{out}}^2)}{E_\perp} & 0 \\ 0 & 0 & \frac{1}{2G} \end{bmatrix} \tag{4.9}$$

where $E_\parallel$ and $E_\perp$ are the Young's moduli parallel and perpendicular to the grain direction and ν_{in} is the in-plane Poisson's ratio, representing compressive strain perpendicular to the grain direction due to a tensile stress parallel to the grain direction and ν_{out} represents the out-of-plane Poisson's ratio.

The constitutive matrix at any arbitrary direction is obtained from the following expression:

$$\boldsymbol{C}_{\text{global}} = T^{-1}\boldsymbol{C}_{\text{local}}T \tag{4.10}$$

where T is the transformation matrix given as a function of the angle (β) between the global direction and the grain orientation direction.

$$T = \begin{bmatrix} \cos^2\beta & \sin^2\beta & 2\sin\beta\cos\beta \\ \sin^2\beta & \cos^2\beta & -2\sin\beta\cos\beta \\ -\sin\beta\cos\beta & \sin\beta\cos\beta & \cos^2\beta - \sin^2\beta \end{bmatrix} \tag{4.11}$$

4.4.2 Ultimate tensile strength

The ultimate tensile strength (τ_{ult}) is an important parameter which determines the fracture propagation. The ultimate tensile strength is maximum in the grain orientation direction and minimum perpendicular to it. Some previous studies (Remij et al., 2015b; Yu et al., 2002; Lee and Pietruszczak, 2015) have assumed cosine functions to interpolate the ultimate tensile strength at arbitrary directions from the values along the grain direction and the perpendicular direction. Here we make use of the Tsai-Hill failure criterion (Jones, 1998) to model the directional dependence of the ultimate tensile strength. The Tsai-Hill failure criterion for a 2-D transverse isotropic material is given as:

$$(\frac{\sigma_\parallel}{\tau_{\text{ult}_\parallel}})^2 + (\frac{\sigma_\perp}{\tau_{\text{ult}_\perp}})^2 - \frac{\sigma_\parallel \sigma_\perp}{\tau_{\text{ult}_\parallel}^2} + (\frac{\sigma_s}{S_{\text{ult}}})^2 = 1 \tag{4.12}$$

where $\sigma_{||}$,$\tau_{\text{ult}_{||}}$ and $\sigma_\perp$,$\tau_{\text{ult}_\perp}$ are the stresses, ultimate tensile strengths parallel and perpendicular to the grain direction respectively, and σ_s and S_{ult} indicate the shear stress and ultimate shear strength in the plane.

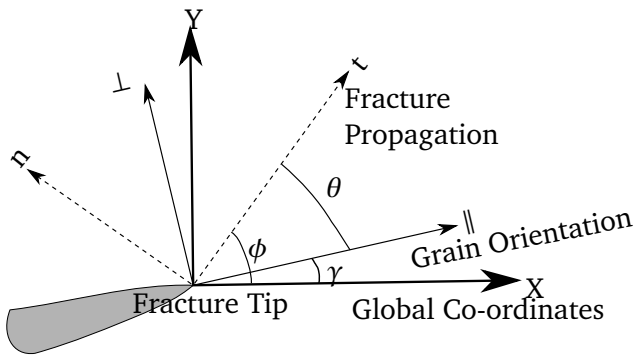

Figure 4.4: Schematic for rotation of parameters.

Assuming a fracture propagating at an angle ϕ with respect to the x-axis, the ultimate tensile strength perpendicular to the fracture propagation direction τ_{frac} is given as the normal stress perpendicular to fracture propagation direction which can satisfy the Tsai-Hill failure criterion. To obtain τ_{frac}, this stress state ($\boldsymbol{\sigma}_{\text{frac}} = \begin{bmatrix} 0 & \tau_{\text{frac}} & 0 \end{bmatrix}^T$) is rotated to the grain orientation direction by using the stress transformation relations and then substituted into Equation (4.12).

$$\boldsymbol{\sigma}_{\text{grain}} = \boldsymbol{T}\boldsymbol{\sigma}_{\text{frac}} \qquad \boldsymbol{\sigma}_{\text{grain}} = \tau_{\text{frac}} \begin{bmatrix} \sin^2\theta \\ \cos^2\theta \\ \sin\theta\cos\theta \end{bmatrix} \tag{4.13}$$

where $\theta = \gamma - \phi$, γ is the grain orientation angle with respect to the x-axis and ϕ is the fracture propagation angle with respect to the x-axis.

Hence for a randomly oriented fracture, we obtain the ultimate tensile strength in the direction perpendicular to the fracture propagation direction ($\phi + 90^o$) as:

$$\frac{1}{\tau_{\text{frac}}} = \sqrt{\frac{\sin^4\theta}{\tau^2_{\text{ult}_\parallel}} + \frac{\cos^4\theta}{\tau^2_{\text{ult}_\perp}} - \frac{\sin^2\theta\cos^2\theta}{\tau^2_{\text{ult}_\parallel}} + \frac{\sin^2\theta\cos^2\theta}{S^2_{\text{ult}}}} \tag{4.14}$$

In order to validate the proposed Tsai-Hill based theory, we make a comparison with experimental results. Mighani et al. (2016) conducted tensile fracture experiments on Lyon's sandstone and pyrophyllite rocks and observed the ultimate tensile strength variation with θ which is the angle between the grain orientation direction and the fracture propagation direction. We make use of the experimental values for maximum and minimum ultimate tensile strengths and interpolate for various angles. As one can observe in Figure 4.5, Tsai-Hill failure criteria provides a much better fit for the experimental values when compared to the previously assumed cosine functions (Remij et al., 2015b; Lee and Pietruszczak, 2015).

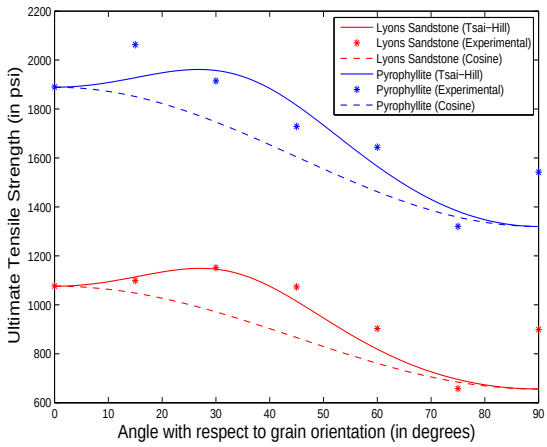

Figure 4.5: Comparison of analytical and experimental values of ultimate tensile strength at various angles with respect to grain orientation direction.

4.4.3 Poro-elastic coefficients

Cheng (1997) derived the analytical expressions for the transverse isotropic poro-elastic coefficients based on the constitutive relationship matrix.

In a fully saturated porous medium, the external stresses on the porous media are partly taken by the fluid pressure in the pores and partly by deformation of the solid grains. This can be represented mathematically as:

$$\boldsymbol{\sigma} = \boldsymbol{\sigma}_{\mathrm{e}} - \boldsymbol{\alpha} p \tag{4.15}$$

where $\boldsymbol{\sigma}$ is the total stress, $\boldsymbol{\sigma}_{\mathrm{e}}$ is effective stress and $\boldsymbol{\alpha}$ is Biot's co-efficient matrix.

The anisotropic Biot's co-efficient matrix reduced to the 2-D form is given by the expression:

$$\boldsymbol{\alpha} = \begin{bmatrix} \alpha_{\parallel} & 0 & 0 \\ 0 & \alpha_{\perp} & 0 \\ 0 & 0 & 0 \end{bmatrix} \qquad \begin{aligned} \alpha_{\parallel} &= 1 - \frac{(C_{11} + 2C_{12})}{3K_s} \\ \alpha_{\perp} &= 1 - \frac{(C_{12} + C_{22} + C_{23})}{3K_s} \end{aligned}$$

The other poro-elastic constants such as bulk modulus and compressibility modulus are given as:

$$K_{\mathrm{bulk}} = \frac{C_{11} + 2C_{22} + 4C_{12} + 2C_{23}}{9} \tag{4.16}$$

$$M = \frac{K_{\mathrm{s}}}{(1 - \frac{K_{\mathrm{bulk}}}{K_{\mathrm{s}}}) - n_{\mathrm{f}}(1 - \frac{K_{\mathrm{s}}}{K_{\mathrm{f}}})} \tag{4.17}$$

where n_f is the porosity of the porous media, and K_s and K_f are the bulk modulus of the solid and fluid respectively.

4.4.4 Permeability

Permeability enters into the formulation through Darcy's law which describes the fluid flow in the porous medium as:

$$\boldsymbol{q} = -\frac{\boldsymbol{\kappa}}{\mu}.\nabla p \tag{4.18}$$

where $\boldsymbol{\kappa}$ is the intrinsic permeability tensor, μ is the dynamic viscosity of the pore fluid, $\boldsymbol{q}$ is the flux and p refers to the pressure in the porous media.

Permeability tensor for an anisotropic rock in the principal grain directions is given as

$$\boldsymbol{\kappa}_{\text{grain}} = \begin{bmatrix} \kappa_{\parallel} & 0 \\ 0 & \kappa_{\perp} \end{bmatrix} \tag{4.19}$$

where permeability in the grain direction $\kappa_{\parallel}$ is larger than the permeability perpendicular to the grain direction $\kappa_{\perp}$. For permeability in any arbitrary orientation we make use of the transformation matrix:

$$\boldsymbol{\kappa}_{\text{frac}} = \Phi^T.\boldsymbol{\kappa}_{\text{grain}}.\Phi \quad \text{where} \quad \Phi = \begin{bmatrix} \cos\theta & -\sin\theta \\ \sin\theta & \cos\theta \end{bmatrix} \tag{4.20}$$

4.5 Results

4.5.1 Validation

Since there are no studies which exactly deal with hydraulic fracturing in anisotropic media, we divide the validation into two parts: 1) Mandel's problem which compares the numerical results with an analytical solution for a transverse isotropic porous medium without fractures 2) The standard KGD problem which compares the numerical results with the ELP model (Remij et al., 2015a) for a hydraulic fracture problem in an isotropic medium.

Mandel's problem

Abousleiman et al. (1996) provided an analytical solution for Mandel's problem in a transversely isotropic porous medium. Mandel's problem (Figure 4.6) consists of an infinitely long rectangular block with the left and right ends free from stresses and the fluid is free to flow whereas an external force is applied on the top and bottom boundaries. The external force is taken as 10.5 MPa. The Young's moduli along horizontal and vertical directions are 20 GPa and 10 GPa respectively. In-plane Poisson's ratio is assumed to be 0.30 whereas the out

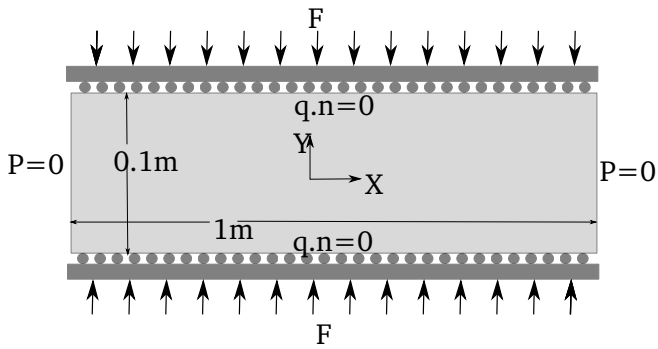

Figure 4.6: Geometry and boundary conditions of Mandel's Problem.

of plane is taken as 0.20. Similarly permeability values are taken to be 10^{-19}m^2 and 10^{-17}m^2 along horizontal and vertical directions. The bulk moduli of the solid grains and the pore fluid are assumed to be 36 GPa and 3 GPa. A time step of 500 seconds is used.

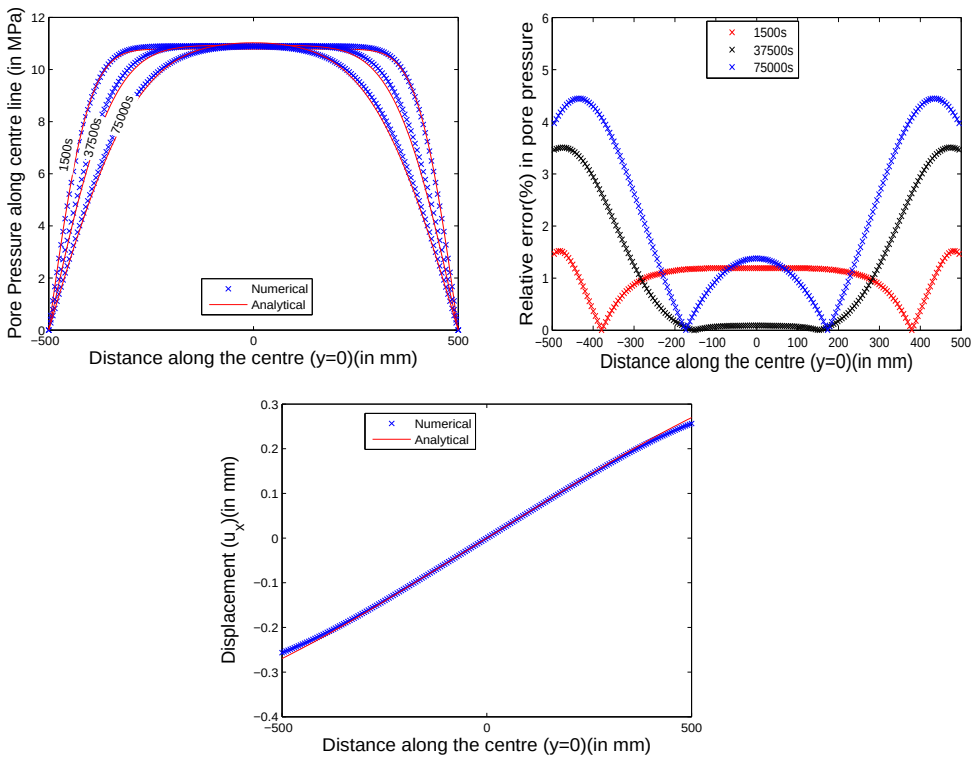

Figure 4.7: a) Pore pressure variation along the centre line at different times b) Relative error (%) in pore pressure when compared to the analytical solution c) Displacement in the x-direction along the centre line at time t=75000s

We compare the pore pressure solution from the numerical model with the analytical solution at different time periods in Figure 4.7. The numerical pore pressure decay from the centre of the specimen to the free edges is found to be consistent with the analytical solution with relative errors (<5%). The displacement in the x-direction along the centre line of the specimen is plotted and compared with the analytical solution.

KGD

In this validation case we consider a KGD problem (Figure 4.8) which is a standard test case for hydraulic fracture problems. When the rock is assumed to be isotropic, there exists a theoretical solution given by Geertsma and De Klerk (1969). The Young's modulus and Poisson's ratio are taken as 20 MPa and 0.2. The ultimate tensile strength is assumed to be 2 MPa while the toughness is 120 N/m. The permeability and viscosity are given as 10^{-19}m^2 and 0.1 Pa s. The initial fracture at the boundary is injected at the rate of 25 mm^2/s for a time period of 100 seconds with a time step of 0.1 s. The KGD problem considered here lies in the viscosity-storage propagation regime.

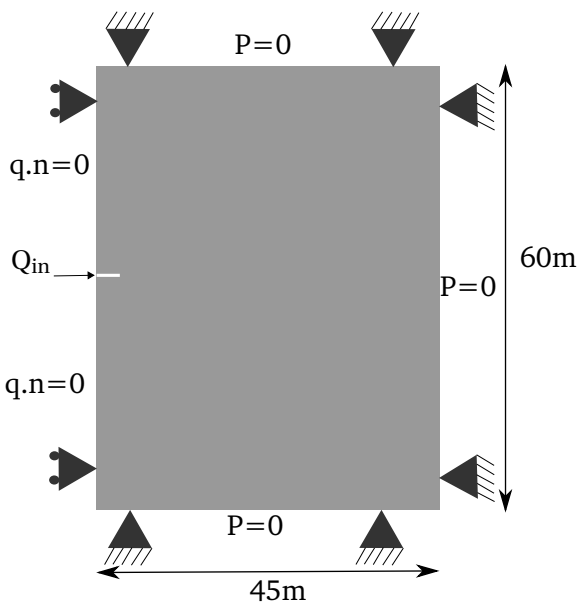

Figure 4.8: Geometry and boundary conditions of standard KGD problem.

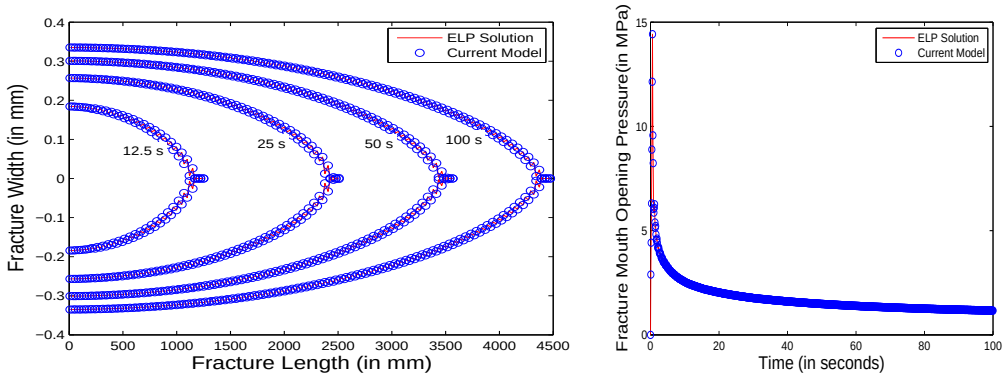

Figure 4.9: a) Comparison of fracture profile variation at different times (t=12.5s,25s,50s,100s) b)Fracture mouth opening pressure variation with time.

The fracture propagates on a non-predefined path. In Figure 4.9, we compare the fracture profiles at various time steps from the current numerical model and the ELP model (Remij et al., 2015a). As observed the current model accurately reduces to the ELP solution for isotropic values of the parameters. The fracture mouth opening pressure variation with time is also plotted and compared. A mesh of 50 $\times$50 mm^2 is used for the purpose.

4.5.2 Vertical hydraulic fracture problem

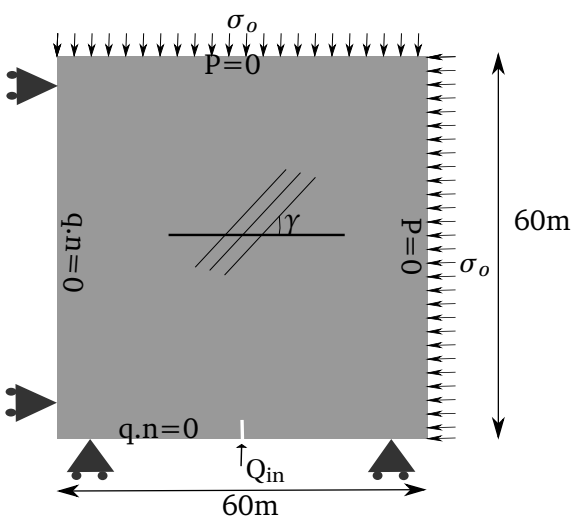

Figure 4.10: Geometry and boundary conditions of the hydraulic fracture problem.

The test case (Figure 4.10) that is used here is very similar to the previous KGD problem, but an initial crack is placed at the bottom of the model, to

model the vertical fracture growth representative of the hydraulic fractures. The model is simulated for 10.5 s with a time step of 0.1 s. Also the model is subjected to external stresses of 40 MPa, due to the overburden pressures or in-situ stresses existing at depths of around 1.5 km. The fluid is free to flow from the top and the right boundaries whereas no flow conditions exist at the left and bottom boundaries. The isotropic values of the parameters used in the model are specified below in Table 4.1. All angles are with respect to the horizontal axis. For cases of anisotropy, these isotropic values are perturbed depending on the degree of anisotropy. The degree of anisotropy is defined as:

$$\text{Degree of Anisotropy (DOA)} = \frac{(.)_{\max} - (.)_{\min}}{(.)_{\max}} \tag{4.21}$$

Table 4.1: Isotropic value of parameters

Parameter	Isotropic Value
Young's modulus	20 GPa
Poisson's ratio	0.2
Toughness(G_c)	120 N/m
Ultimate tensile strength	6 MPa
Ultimate shear strength	60 MPa
Permeability	10^{-19}m^2
Porosity	0.1
Viscosity	10^{-2} Pa s
Solid bulk modulus	36 GPa
Fluid bulk modulus	3 GPa
Injection rate	0.0006 m^2/s
Overburden pressure	40 MPa

By using the parameters in the Table 4.1 to obtain the non-dimensional parameter($\mathscr{M}_k$) described in Bunger et al. (2005), we observe that the hydraulic fracture problem described here lies in the viscosity dominated regime and closer to the storage edge. In the following subsections 4.5.3 and 4.5.6 we try to understand the influence of anisotropy in each individual parameter by keeping all other parameters isotropic. We also look at the possible combination of anisotropy in these parameters in subsections 4.5.4 and 4.5.6 .

4.5.3 Parametric anisotropy

In this subsection, we vary one parameter at a time to find out the fracture propagation variation with anisotropy in each individual parameter. In all the considered test cases we assume that the grains are oriented along the horizontal direction (0°) and the initial fracture is oriented in the vertical direction

(90°).

Anisotropy due to Young's modulus

We consider three possible scenarios for varying Young's modulus: i) E-Parallel: Anisotropy caused by increasing the Young's modulus ($E_{\parallel}$) parallel to the grain direction alone. ii) E-Perpendicular: Anisotropy caused by decreasing the Young's modulus ($E_{\perp}$) perpendicular to the grain direction alone. iii) E-Combined: Anisotropy caused by varying both parallel and perpendicular values from the isotropic values given by following equation:

$$(.)_{\parallel} = \frac{(.)_{\text{isotropic}}}{1-(\text{DOA}/2)} \qquad (.)_{\perp} = (1-\text{DOA})(.)_{\parallel} \tag{4.22}$$

Both in-plane and out-of-plane Poisson's ratios are assumed to have a constant value of 0.2.

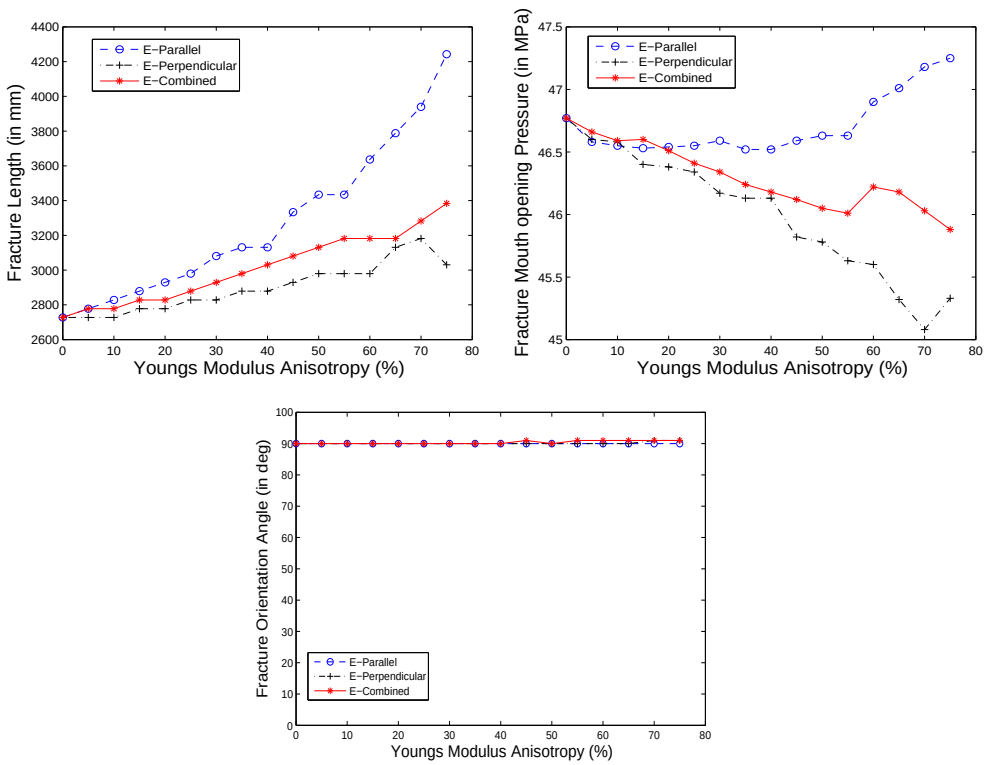

Figure 4.11: Fracture variation with Young's modulus anisotropy.

From the fracture length plot in Figure 4.11, we can observe that $E_{\parallel}$ has a much greater effect on fracture propagation than $E_{\perp}$. This is due to the fact that the propagation of the initial vertical fracture is dependent on the stresses

which are perpendicular to it. Hence an increase in $E_{\parallel}$ results in higher stresses perpendicular to the initial fracture, which promotes fracture growth significantly whereas a decrease in $E_{\perp}$ only has a smaller Poisson's effect on the stress. Since $E_{\parallel} > E_{\perp}$ always, the fracture prefers to orient itself perpendicular to the grain orientation which is observed in all the three scenarios in the fracture orientation plot.

Also we plot the pressure at the mouth of the fracture, which is a much more easily measurable quantity in the field. Since all the three scenarios favour fracture propagation in the same initial fracture direction, there is little variation ($< 5\%$) in the pressure required to open the fracture.

Anisotropy due to ultimate tensile strength

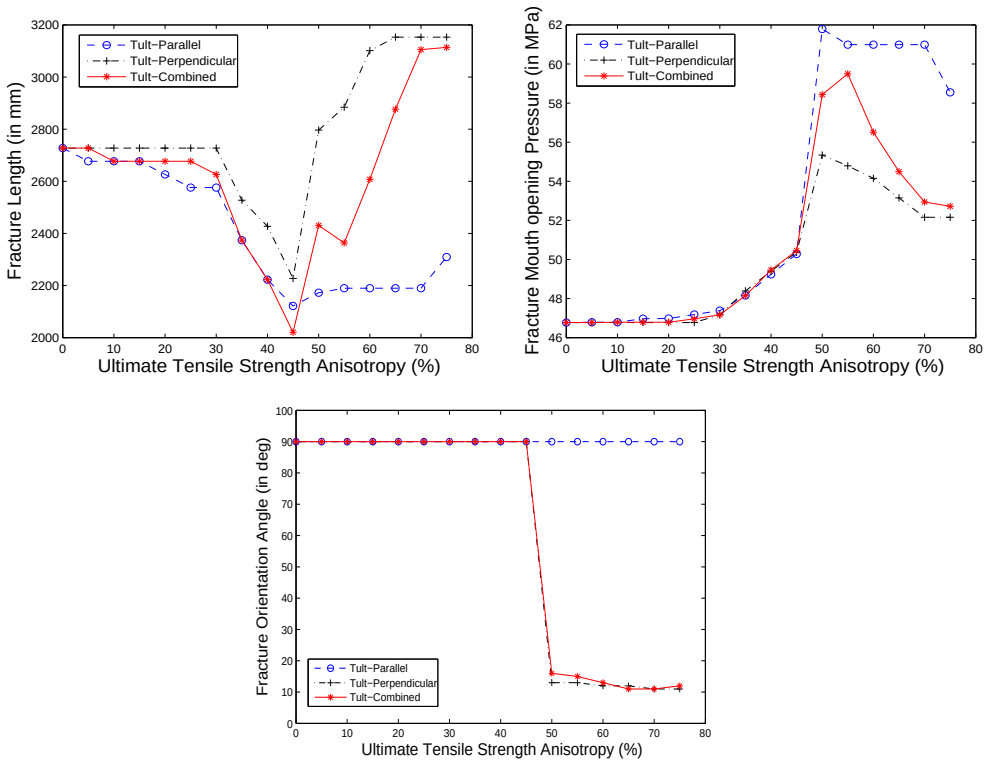

Figure 4.12: Fracture variation with ultimate tensile strength anisotropy.

Similar to the Young's modulus variation, we consider the same three scenarios for understanding ultimate tensile strength induced anisotropy. Fracture propagation is resisted by the ultimate tensile strength perpendicular to the fracture orientation. Hence the fracture tends to propagates along the direction perpendicular to the minimum ultimate tensile strength. Since $\tau_{\mathrm{ult}_{\perp}}$ is always lower

than $\tau_{\mathrm{ult}_{\parallel}}$, the fracture tends to propagate parallel to the grain orientation. But since the initial fracture is oriented in an unfavourable direction (perpendicular to the grain direction), the fracture continues to propagate in its initial direction until a threshold level where the effect of anisotropy becomes significant to rotate the fracture as observed from the fracture orientation plot in Figure 4.12.

Also looking at the fracture length variation we observe that there is a significant increase in the fracture length when the fracture re-orients itself from its initial direction to the favourable direction. Since the fluid inside the fracture has to go through steep rotation ($\sim 80^o$), much higher pressures are required in order to drive the fracture.

Anisotropy due to permeability

Anisotropy in the permeability of the rocks was considered in the formulation. As indicated in Table 4.1, the isotropic permeability of shales was assumed to be $10^{-19}\mathrm{m}^2$ (100nd). It was varied within two orders of magnitude i.e. $10^{-18}\mathrm{m}^2$ to $10^{-20}\mathrm{m}^2$ (1000nd to 10nd). However its impact on the fracture growth was found to be very negligible since shales already have very low permeability values (almost impermeable).

4.5.4 Degree of material anisotropy

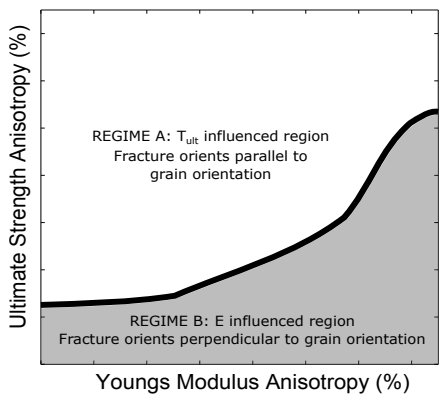

Figure 4.13: Different fracture influence regimes in material anisotropy.

In the following subsections, we focus only on the fracture propagation direction. This is because variation in fracture length or width due to various anisotropies and combinations can be overcome by varying the fluid injection time but the fracture orientation direction cannot be modified by means of any external influence as it is solely dependent on the field conditions. Hereafter

all the anisotropies considered are by varying both the values parallel and perpendicular to the grain direction as given by Equation (4.22).

In this set of cases, we study the interplay between anisotropy due to Young's modulus and the anisotropy due to ultimate tensile strength by varying them from 0% to 75% individually. As seen from the previous Section 4.5.3, both these anisotropies have contrasting effect on the fracture propagation direction. Therefore it is important to identify the regions where one parameter has a higher degree of influence than the other.

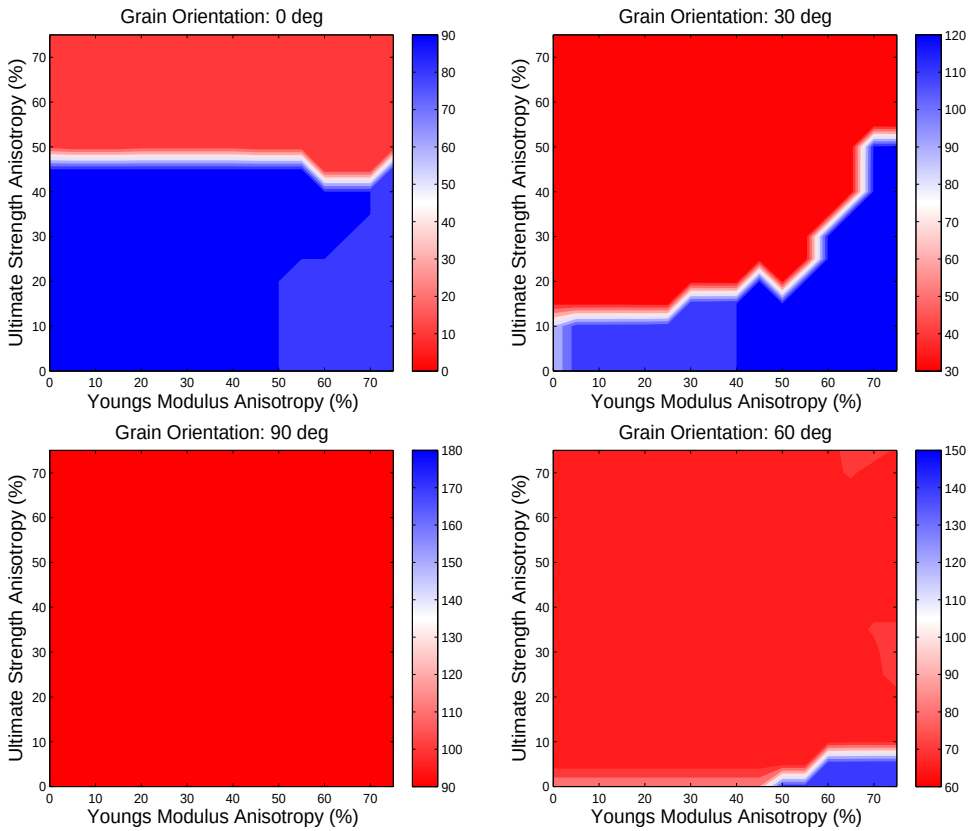

Figure 4.14: Final fracture orientation angle (ϕ, with respect to global horizontal axis) variation with material anisotropy at different grain orientation angles a)0° b)30° c)60° d)90°. The blue colour indicates final fracture gets oriented perpendicular to the grain orientation whereas the red colour indicates parallel to grain orientation. The transition between the blue and red colours (indicated by white colour), would be a very sudden transition if smaller anisotropic step sizes are used.

Figure 4.13 represents a schematic of the material anisotropy contour plots in Figure 4.14. As can be seen there are two distinct regimes: i) Regime A,

influenced by anisotropy in ultimate tensile strength causing the fractures to propagate parallel to the grain direction ii) Regime B, influenced by anisotropy in Young's modulus resulting in fractures finally getting oriented perpendicular to the grain direction. There is a sudden transition from one regime to another once a threshold value is crossed.

In Figure 4.14, we observe that contour plots are represented for four different grain orientation (γ) directions. γ refers to a grain orientation with respect to the global horizontal direction (x-axis). The non-smooth variations in the threshold values for transition between regimes in the contour plots are due to the variation of anisotropies in step sizes of 5%. Looking at the different contour plots we can see that the size and shape of the different regimes vary with varying grain orientation angles.

From the $\gamma = 0^o$ plot, we observe that beyond a threshold value of 50% DOA in τ_{ult} the fracture moves from regime B to regime A (red regions representing $\phi < 20^o$). Looking at the plot for $\gamma = 30^o$, we observe that the fracture tries to align itself perpendicular to the grain direction (blue regions representing $\phi > 100^o$) even for relatively low values of E anisotropy but requires much higher (> 40%) DOA in Young's modulus along with low (< 10%) DOA in ultimate tensile strength when $\gamma = 60^o$. Young's modulus anisotropy cannot influence the fracture at all when the fracture needs to be completely rotated by 90°.

Looking at all the contour plots we can observe that the area of regime A increases with grain orientation angle. The influence of τ_{ult} anisotropy is much higher as the grain orientation angle increases due to the fact that the fracture needs to be rotated by a smaller angle from its initial vertical orientation to align itself with the grain orientation direction. The converse is true for the influence of Young's modulus anisotropy.

4.5.5 Angle of orientation

In this set of cases, we vary the degree of anisotropy of the material parameters (namely both Young's modulus and ultimate tensile strength simultaneously) between 0% and 75% as well as the grain orientation direction from 0° to 90°. The results of these cross-sets of cases are represented in the form of a contour plot as given in Figure 4.15.

Grain orientation direction

We observe that along the vertical axis (for a particular grain orientation direction), after a certain degree of combined material anisotropy the crack always tends to align with the grain direction. This is due to the fact that τ_{ult} anisotropy has a greater impact than the E anisotropy at larger values of DOA (> 30%) whereas E anisotropy has a much larger impact when the DOA is lower (< 30%) . Along the horizontal axis (for a particular combined material DOA),

we observe that the fracture tends to re-orient itself with relative ease as the angle ($\theta = \gamma - \phi$) between the initial fracture orientation and the grain orientation reduces.

In Figure 4.16, the fracture propagation at a constant combined material

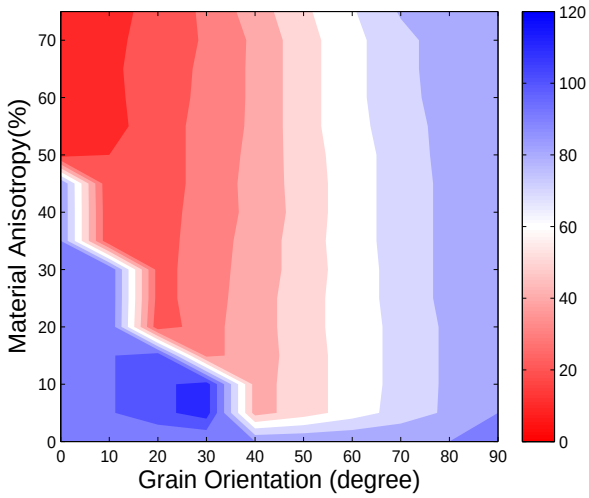

Figure 4.15: Final fracture orientation angle (ϕ) variation with different degrees of combined material anisotropy and grain orientation angles with respect to horizontal axis. The transition between the blue and red colours along the vertical in the left corner, would be a very sudden transition if smaller anisotropic step sizes are used.

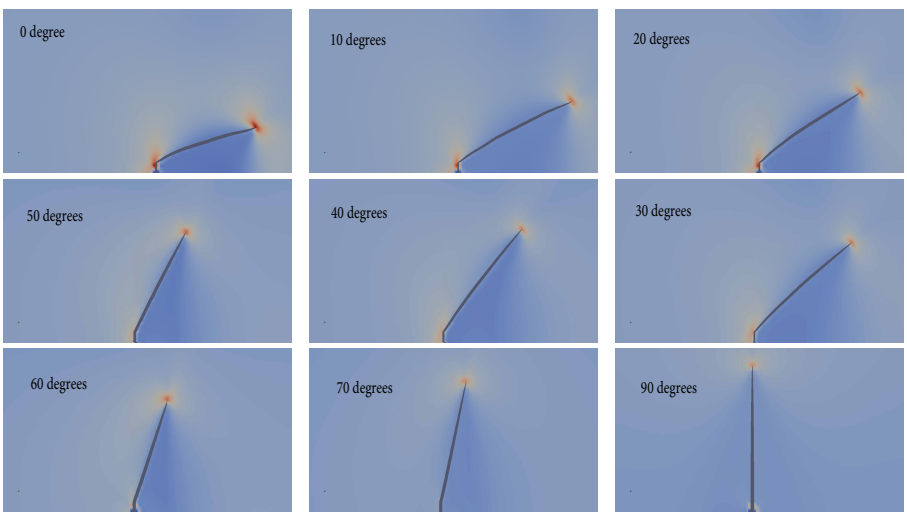

Figure 4.16: Propagation of an initial vertical fracture with different grain orientation angle for a material anisotropy of 55%.

degree of anisotropy of 55% for various grain orientation angles from 0° to 90° is plotted.

Initial fracture orientation

In all the previous and later cases, the initial fracture is assumed to be along the vertical direction (90°). In this subsection, three initial fractures at varying initial orientation angles of 90°, 60°, and 0° are included simultaneously. The grain orientation angle is assumed to be 60° with a combined material DOA of 15%.

From Figure 4.15 for a material DOA of 15%, we observe that the fracture aligns along the grain orientation direction when $\theta < 50^o$ and aligns perpendicular to the grain direction when $\theta > 50^o$. For the initial fractures 90°,60°, and 0° corresponding theta values are 30°,0°, and 60° respectively. Hence the first two initial fractures (90° and 60°) are expected to be aligned along the grain orientation direction (60°), while the 0° initial fracture is expected to be aligned perpendicular to the grain orientation direction (150°) which is exactly replicated by the results shown in Figure 4.17.

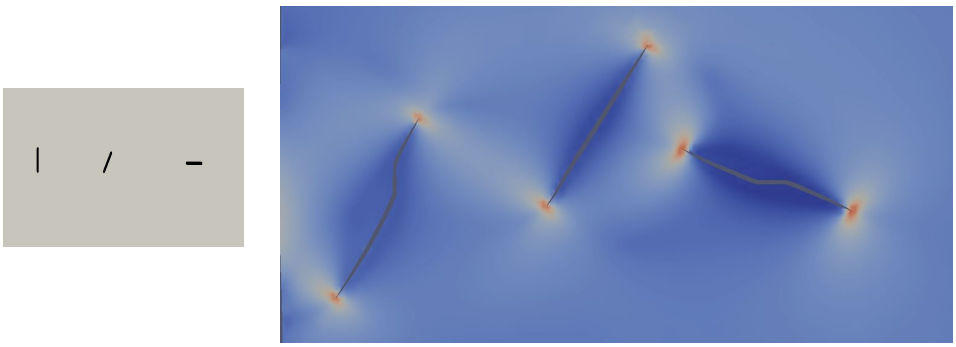

Figure 4.17: Influence of initial fracture orientation on fracture propagation.

4.5.6 Lithostatic stresses

Anisotropy due to lithostatic stress

Similar to other parametric variations, we consider the three possibilities of stress induced anisotropy due to i) increase of vertical stresses ii) decrease of horizontal stress iii) a combination of both. Note that in real hydraulic fracture scenarios in the field, the vertical overburden pressure is assumed to be slightly larger than the horizontal pressure. The fracture orients itself preferably in the direction parallel to the maximum compressive stress, which is same as the initial fracture direction (90°) in all the three scenarios. The decrease of horizontal stresses results in much lower compressive stresses perpendicular to the

fracture, thereby promoting fracture growth and also requiring less pressure to open the fracture as seen from Figure 4.18. Similarly the increase of vertical stresses only causes a mild increase in the tensile stresses acting perpendicular to the fracture due to Poisson's effect.

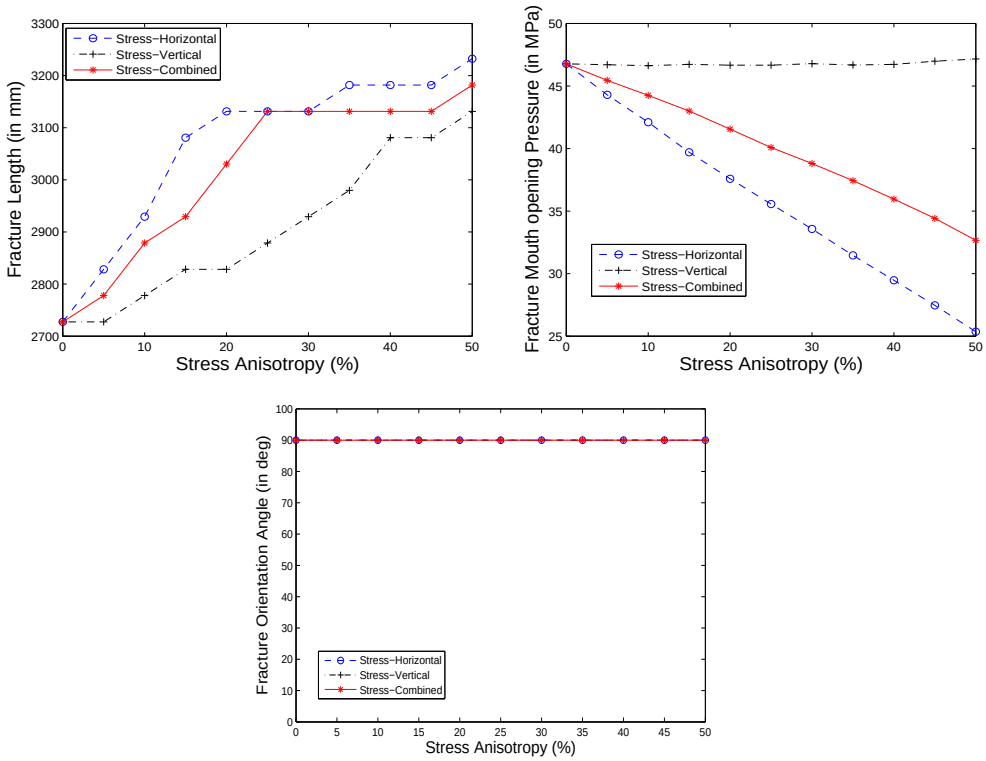

Figure 4.18: Fracture variation with stress anisotropy.

Combined anisotropy

In this final scenario we look at combining all the above discussed anisotropy scenarios. The material anisotropy refers to varying both Young's modulus and ultimate tensile strength simultaneously from 0% to 75% by using Equation (4.22). The stress anisotropy refers to variation of the overburden pressures from 0% to 50% given by Equation (4.22). The contour plots are obtained for four different grain orientation angles (γ) namely 0°, 30°, 60° and 90°.

In looking at the schematic (Figure 4.19) for the combined anisotropy contour plots given in Figure 4.20, we observe that apart with regimes A and B, there is an additional regime C in which the in-situ stresses play a major role in determining the final fracture orientation. The fractures get oriented parallel to the maximum compressive stress direction in this regime. Looking at the plot for $\gamma = 0^o$, as already seen in Figure 4.14 the fracture tends to re-orient

itself parallel to grain direction after a combined material DOA of 50%. But this re-orientation is possible only when the stress anisotropy is less than 20%, beyond which the fracture transitions into regime C. Regime B and regime C coincide in this case as perpendicular to the grain direction and the maximum compressive stress are both in the vertical direction.

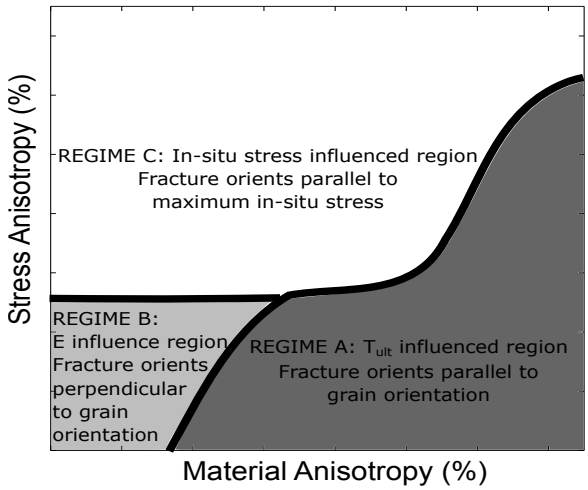

Figure 4.19: Different fracture influence regimes in combined stress and material anisotropy.

The plot for $\gamma = 30^o$ is the most complete plot with all the regimes which are influenced by the various anisotropy parameters. The dark blue regions representing fracture orientations (ϕ) larger than 110 are indicative of regime B at low material DOA (< 25%) and low stress DOA (< 25%). The high material DOA (> 25%) and low stress DOA (< 30%) regions represented by varying intensities of red colour (Regime A), are indicative of the ultimate tensile strength influence. For high stress DOA (> 30%) (Regime C), the fractures are more influenced by the stress induced anisotropy. But the fracture orientation angles (ϕ) are not exactly 90° which it is supposed to be as the vertical overburden pressures are maximum. This is because of the fact that although external stresses are maximum in one direction the local stress state has maximum values in a different direction as a result of the Young's modulus anisotropy. Therefore the fracture ends up oriented at angles ($\sim 100^o$) in between perpendicular to the grain orientation (120°) and the vertical direction (90°).

When $\gamma = 60^o$, the ultimate tensile strength has great influence over most of the regions except the regions with high stress DOA (> 30%) and high material DOA(> 40%) where both the stress and Young's modulus anisotropy combine. When $\gamma = 90^o$, both the combined material DOA and the stress anisotropy prefer the fracture to propagate along its initial vertical direction causing all the regimes to coincide.

Looking at all the four contour plots together one can observe the reduction in the influence of stress induced anisotropy as the grain orientation direction increases or in other words when the angle ($\theta = \gamma - \phi$) between the initial fracture orientation and the grain direction decreases while the converse is true for material based anisotropy.

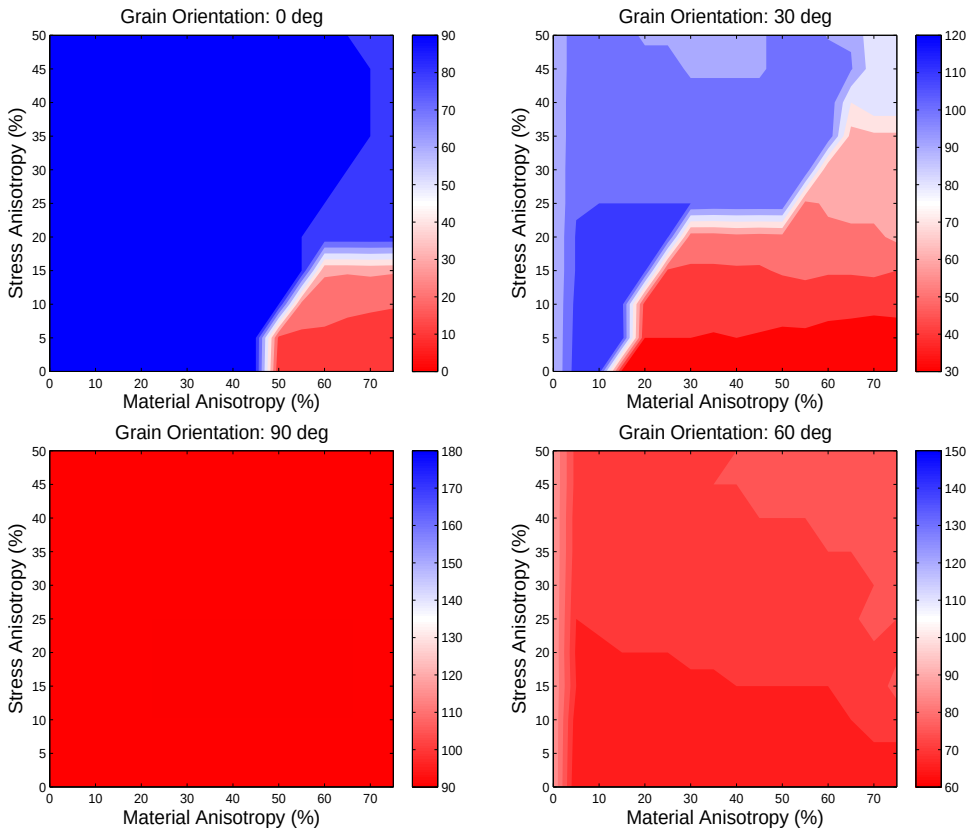

Figure 4.20: Final fracture orientation angle (ϕ, with respect to global horizontal axis) variation with material anisotropy and stress anisotropy at different grain orientation angles a)0° b)30° c)60° d)90°. The blue colour indicates final fracture gets oriented perpendicular to the grain orientation whereas the red colour indicates parallel to grain orientation. The transition between the blue and red colours (indicated by white colour), would be a very sudden transition if smaller anisotropic step sizes are used.

4.6 Conclusion

From all the above simulations, we observe that the hydraulic fractures are greatly influenced by the anisotropy arising due to various parameters. Some

of the important observations are:

a) Young's modulus anisotropy promotes fracture growth perpendicular to the grain direction.

b) Ultimate tensile strength anisotropy promotes fracture growth parallel to the grain direction.

c) Stress induced anisotropy promotes fracture growth parallel to the maximum overburden pressure.

d) At high degrees of material anisotropy, ultimate tensile strength has a greater influence than the Young's modulus while the converse is true for low degrees of anisotropy.

e) Most important angle influencing fracture orientation is the angle between grain orientation and the initial orientation. When this angle decreases, the influence of ultimate tensile strength anisotropy increases while the influence of Young's modulus anisotropy and stress based anisotropy decreases.

Combination of stress anisotropy, material anisotropy and the initial fracture orientation with respect to the grain orientation is observed to determine the final fracture propagation direction.

Chapter 5

Hydraulic fracture propagation in heterogeneous reservoirs

Abstract

In this chapter, we investigate the behaviour of hydraulic fractures in a heterogeneous reservoir. The heterogeneity in the reservoir can either be of discrete nature, due to the presence of inclusions which are formed due to the precipitation of minerals at specific locations, or of a layered nature due to the deposition of different minerals over different times. We extend the Modified Enhanced Local Pressure (MELP) model as presented in Chapter 3, that is based on a two-dimensional extended finite element method. The fracture propagation direction is not prescribed and is dependent on the Camacho-Ortiz propagation criterion. The fracture behaviour due to layering is found to be dependent on the contrast in the material properties (Young's modulus, ultimate tensile strength) between the different layers as well as the reservoir level properties such as layer thickness, in-situ stresses, bedding plane orientation. The fracture propagation mechanism is also observed to change based on the layer in which the fracture initiates and propagates further (i.e. from a soft to hard layer or vice versa). We also investigate the effect of a finely layered reservoir. The behaviour of fractures in the presence of inclusions are found to be dependent on the contrast between the material properties of the inclusions and the host rock.

Reproduced from: Valliappan, V., Remmers, J. J. C., Barnhoorn, A., & Smeulders, D. M. J., Hydraulic fracture propagation in heterogeneous reservoirs. Journal of Petroleum Science and Engineering, in preparation.

5.1 Introduction

Fluid pressure driven, hydraulic fractures have made the extraction of oil and gas from unconventional reservoirs economically feasible (Economides and Nolte, 2000). Hydraulic fracture height has been the focus of several works primarily due to concerns around contamination of groundwater aquifers with the fracturing fluid (Rozell and Reaven, 2012; Warner et al., 2012; Brantley et al., 2014) while other experimental (Fisher et al., 2011) and analytical models (Flewelling et al., 2013) have shown that these concerns might be unrealistic due to a fracture height containment phenomenon. These contrasting results make it vital to accurately model the fracture propagation in the vertical direction. Hydraulic fracture propagation analysis are often focused on the vertical fracture height that is obtained due to injection pressures, propagation velocity, lithostatic stresses.

One of the most common factors affecting the fracture growth in the vertical direction is the layered nature of the sedimentary rocks (Nolte et al., 1979; Warpinski et al., 1982; Teufel and Warpinski, 1983). These distinct layers are formed due to the sedimentation of different minerals and organic particles over time (Blatt et al., 1972). Due to the different mineralogy, these layers exhibit stark contrasts in the rock material properties such as Young's modulus, ultimate tensile strength, porosity and permeability. Hence even if we consider a single layer to be homogeneous, the rock structure on a macroscopic scale would be heterogeneous.

Some of the earliest works on the effect of this layered heterogeneity on the hydraulic fractures were developed by Daneshy et al. (1978). He observed the fracture propagation across layers to be strongly dependent on the interfacial strength between the two layers, while Simonson et al. (1978) obtained an analytical expression for fracture height which depends on the in-situ stresses in both the formation and the barrier zones along with fracture toughness of the materials and borehole pressure. Later, these two different phenomenon have been studied by various other researchers as a cause for fracture height containment in reservoirs.

Warpinski et al. (1981, 1982) conducted a series of laboratory and field-scale mineback experiments. They observed the fracture height containment in a layered rock formation to be strongly dependent on the in-situ stress state in the layers and reported only a small influence of the interfacial properties. In the presence of layered formations, the fractures exhibited a complex behaviour with multiple strands instead of a simple planar fracture.

The presence of weak interfaces in the rock formation act as shear slip planes along which the fractures orient themselves to form T-shaped fractures or have an offset along the interface. Experimental observations of such fracture slippage along interfaces were observed by Xing et al. (2016) . Numerical

models to study the fracture behaviour along the interface under various field conditions were developed by several authors (Garcia et al., 2013; Chuprakov et al., 2015; Ouchi et al., 2017). These interfacial models are strongly dependent on the interfacial shear strength (τ_{shear}) which in-turn is related to the cohesion (τ_{o}) between the two layers and friction between the two layers.

$$\tau_{\text{shear}} = \tau_{\text{o}} + \mu_{\text{f}}\sigma_{\text{n}} \tag{5.1}$$

From Eq.(5.1), we can observe that the interfaces can be weak only in shallow reservoirs due to the lower normal lithostatic stresses (σ_{n}).

Some models that explain the fracture height containment phenomenon in the absence of weak interfaces were developed. The impact of Young's modulus contrast on the fracture propagation was studied by Gu et al. (2006). While Smith et al. (2001) observed the impact on the fracture width and how it affects the proppant placement process. Miskimins et al. (2003) focussed on the modelling of thinly layered formations. These models assumed a very strong interface and the resultig fracture behaviour was purely the result of variation in rock material properties. All these models assume the fracture propagation along a prescribed direction.

In this chapter we investigate the propagation of hydraulic fractures in layered reservoirs by extending the Modified Enhanced Local Pressure (MELP) model proposed by in Chapter 3. We focus on hydraulic fracturing in deep reservoirs where the friction between the layers is strong enough to prevent fracture slippage along the interfaces. Hence in the presence of strong interfaces, an interface that cannot fail, the fractures always propagate into the second layer or get trapped within the layer in extreme cases. The contrast in rock material properties determines the in-situ stresses in each layer which inturn decides the fracture propagation direction. Thereby we can model the fracture behaviour across the layers with strong interfaces.

5.2 MELP Model

5.2.1 Physical model

A hydraulic fracture problem can be defined as a combination of a poro-mechanics problem and a fracture problem. In order to model the poro-mechanics problem, we make use of Biot's theory of poro-elasticity (Biot, 1941). The unknowns associated with the poro-mechanics problem are the deformation in the solid grains ($\boldsymbol{u}$) and the fluid pressure in the pores (p) . The fluid flow in the porous medium is governed by Darcy's law. These unknowns are solved using the mass and momentum balance equations and its associated boundary conditions. The stress in the solid grains is coupled with the pressure in the pores by means of effective stress.

The introduction of a fracture causes a discontinuous jump in the displacement field across the fracture. We make use of a cohesive zone model (Barenblatt, 1962) to avoid the singularity at the fracture tip by lumping the fracture tip to a plane. This also introduces a cohesive traction, which is dependent on the displacement jump, along the normal to the fracture.

The injection of fluid into the fracture in a hydraulic fracture problem causes a fluid flow inside the fracture as well as leak-off of fluid from the fracture to the adjacent formation. We introduce an additional field variable to model the pressure inside the fracture (p_{d}) as prescribed in the ELP model proposed by Remij et al. (2015a). The leak-off phenomenon is modelled using the analytical 1-D Terzaghi consolidation equation (Terzaghi, 1925). In order to solve for this additional unknown we make use of the mass balance equation inside the fracture as derived by Irzal et al. (2013).

5.2.2 Numerical model

We need to make use of a numerical method, in order to solve for all the the unknown field variables from the various governing equations as described above. While several numerical methods can be employed for the problem, the introduction of a discontinuity in the model makes the use of an extended finite element method (XFEM) desirable. The XFEM model makes use of partition of unity property of the finite element shape functions to include a discontinuity in a continuous field (Melenk and Babuška, 1996). Hence using XFEM we can spatially discretise the field variables in the porous formation as :

$$\boldsymbol{u} = \boldsymbol{N}\hat{\boldsymbol{U}} + H_{\Gamma_{\mathrm{d}}}\boldsymbol{N}\tilde{\boldsymbol{U}} \tag{5.2}$$

$$p = \boldsymbol{H}\hat{\boldsymbol{P}} + H_{\Gamma_{\mathrm{d}}}\boldsymbol{H}\tilde{\boldsymbol{P}} \tag{5.3}$$

while the discretisation of the fluid pressure inside the fracture is written as:

$$p_{\mathrm{d}} = \boldsymbol{V}\boldsymbol{P}_{\mathrm{d}} \tag{5.4}$$

$\boldsymbol{N}, \boldsymbol{H}, \boldsymbol{V}$ are the shape functions associated with displacement, pore pressure and pressure inside the fracture respectively. $\hat{\boldsymbol{U}}, \tilde{\boldsymbol{U}}$ represents the regular and additional nodal values for the displacement field, while $\hat{\boldsymbol{P}}, \tilde{\boldsymbol{P}}$ represents the regular and additional nodal values for the pressure field. $\boldsymbol{P}_{\mathrm{d}}$ represents the nodal values of the enhanced local pressure.

Using this discretisation, we convert the set of governing differential equations into a set of algebraic equations. Details of the derivation of the discrete balance equations are given in Section 3.4. We make use of Newton-Raphson method and a monolithic solver to obtain the solution for the field variables at all the nodes for every time step.

5.2.3 Propagation

Using the solution for the field variables, we compute the effective stresses at all the integration points based on the generalised Hooke's law. But to obtain the stresses in the vicinity of the crack tip, we make use of a weighted average method as proposed by Jirasek (1998).

$$\boldsymbol{\sigma}_{\mathrm{av}} = \sum_{\mathrm{i}=1}^{(\mathrm{n_{int}})_{\mathrm{m}}} \frac{w_{\mathrm{i}}}{w_{\mathrm{tot}}} \boldsymbol{\sigma}_{\mathrm{e,i}} \qquad w_{\mathrm{tot}} = \sum_{\mathrm{j}=1}^{(\mathrm{n_{int}})_{\mathrm{m}}} w_{\mathrm{j}} \tag{5.5}$$

where $\boldsymbol{\sigma}_{\mathrm{e,i}}$ is the effective stress at the integration point i, $(\mathrm{n_{int}})_{\mathrm{m}}$ is the number of integration points in the material m, in which the fracture tip is present. w_{i} is the weight assigned for the integration point, which is based on its distance from the crack tip given as:

$$w_{\mathrm{i}} = \frac{(2\pi)^{-3/2}}{l_{\mathrm{a}}^{3}} \exp^{\frac{-r_{\mathrm{i}}^{2}}{2l_{\mathrm{a}}^{2}}} \tag{5.6}$$

where r_{i} is the distance of the integration point from the crack tip, l_{a} is the characteristic length which sets the decay of the weight function with distance from crack tip. This averaging procedure for a model with a single material and multiple materials is shown in Figure 5.1.

Note that in this model the material interfaces are aligned with the element interfaces. Based on the assumption that the material interfaces are perfectly bonded, it is assumed that there are no interfacial fractures.

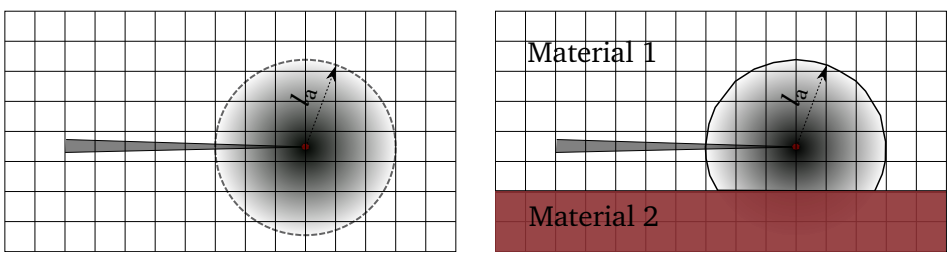

Figure 5.1: Stress averaging close to the fracture tip in a) Single material b) Multiple materials. The intensity of the shade within the characteristic zone indicates the weight functions associated with integration points

Using these averaged stresses in combination with the Camacho-Ortiz propagation criteria (Camacho and Ortiz, 1996), we determine the fracture propagation. The averaged stresses leads to slight delay in the fracture propagation. The fracture is assumed to propagate through an entire element for each propagation step. The elements that are crossed by fractures make use of an adopted integration scheme as proposed by Wells and Sluys (2001). For further details on the implementation of the numerical model we refer to Remmers et al. (2003) and Remmers (2006).

5.3 Numerical Example

We model this layered heterogeneity with the help of a rock structure containing five different layers as shown in Figure 5.2. Each rock layer is assumed to be homogeneous with a thickness of 1 m. The rock structure has free flow conditions at all the boundaries and is subjected to a uniform lithostatic stress of 20 MPa in both the horizontal and vertical directions. The porosity (n_f) and the permeability (κ) of the rock structure are assumed to be 0.1 and 10^{-19}m^2 respectively. A small initial fracture with a length of 0.2 m is initiated at the middle layer. Fracturing fluid with a viscosity of 0.01 Pa · s is injected into the middle of the fracture at the rate of 10^{-6}m^2/s for 40 seconds. The base values of the rock material properties are always present in the softer layers. The base Young's modulus is 10 GPa while the Poisson's ratio is 0.2. The base ultimate tensile strength is assumed to be 4 MPa.

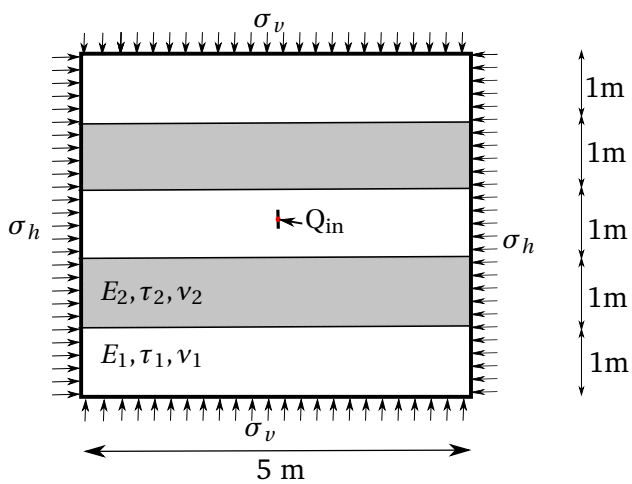

Figure 5.2: A layered rock with a fracture at the middle. The rock contains two alternating layers with distinct properties. The middle layer has properties $E_1, \tau_{\text{ult}_1}, \nu_1$ while the layers surrounding the middle layer has properties $E_2, \tau_{\text{ult}_2}, \nu_2$

We try to understand the fracture behaviour in such a layered rock and their variation in behaviour with contrast in material properties between the layers as well as the influence of other reservoir level properties. We have identified Young's modulus and ultimate tensile strength as two important variables in the model which have a major impact on hydraulic fracture propagation (Valliappan et al., 2017). Hence we have varied these two parameters over a wide range. The Young's modulus contrast ($C_E = E_2/E_1$) between the layers is varied from 1 to 12, i.e. the Young's modulus values of the stiffer layers (E_2) are varied from 10 GPa to 120 GPa while maintaining the Young's modulus of the

softer layer (E_1) to be 10 GPa. The ultimate tensile strength ($C_\tau = \tau_{\text{ult}_2}/\tau_{\text{ult}_1}$) contrast ratio is varied from 1 to 5. This set of tests are repeated for varying lithostatic stresses, layer thickness, bedding plane orientation.

In the reference case, we consider the fracture to originate in a soft layer (lower Young's modulus) and is bounded by stiffer layers (higher Young's modulus). The fracture behaviour for a set of varying Young's modulus and ultimate tensile strength is presented in Table 5.1. The different fracture behaviour patterns exhibited for the current case are: Crossing (denoted by C with white colour), Kinking (K with yellow colour), Deflection (D with green colour). These different phenomenon has been shown in Figure 5.3.

Table 5.1: Fracture behaviour in a layered rock when propagating from a soft (E_1 = 10MPa, τ_{ult_1} = 4MPa, $\nu_1 = 0.2$) to a hard layer with varying Young's modulus and ultimate tensile strength contrast. (C-crossing, D-Deflection, K-Kinking, A-Arrest)

		Young's modulus contrast (C_E)													
		1	2	2.5	3	3.5	4	4.5	5	6	7	8	9	10	12
τ_{ult} contrast	1	C	C	C	K	D	D	D	D	D	D	D	D	D	D
	2	C	C	C	K	K	K	D	D	D	D	D	D	D	D
	3	C	C	C	C	K	K	K	K	D	D	D	D	D	D
	4	C	C	C	C	K	K	K	K	D	D	D	D	D	D
	5	C	C	C	C	C	K	K	K	K	D	D	D	D	D

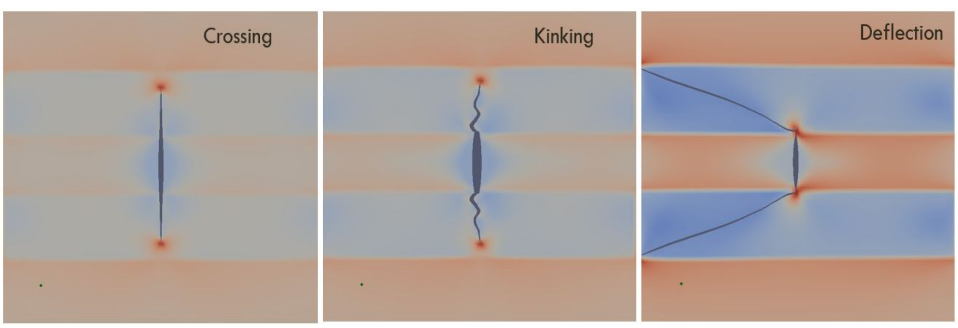

Figure 5.3: Different fracture behaviours when propagating from a softer layer to a stiffer layer. The fracture initiates from the middle layer which is softer (E_1 = 10MPa, τ_{ult_1} = 4MPa, $\nu_1 = 0.2$) and propagates to the surrounding stiffer layers.

We can clearly observe from Figure 5.3, that the fracture width becomes significantly narrower in the layer with a higher modulus and this also causes the fracture to propagate longer. These observations are in-line with the analytical models developed by Simonson et al. (1978) and numerical model developed

by Gu et al. (2006). We can see that the fracture always propagates from the softer into the stiffer layer but exhibits different behaviour in the stiffer layer depending on to the in-situ stress state.

5.3.1 Influence of material properties

In this sub-section we investigate the contrast in the various material properties and their influence on the fracture behaviour.

Young's modulus variation

The contrast in Young's modulus (C_{E}) between the layers has the most prominent effect on fracture behaviour in layered rocks as observed by Gu et al. (2006) and Smith et al. (2001). The common range of values for Young's modulus for rocks is 1 - 100 GPa (Hatheway and Kiersch, 1989; Afrouz, 1992). We vary the Young's modulus in the stiffer layer from 10 GPa to 120 GPa while keeping a constant Young's modulus of 10 GPa in the softer layer.

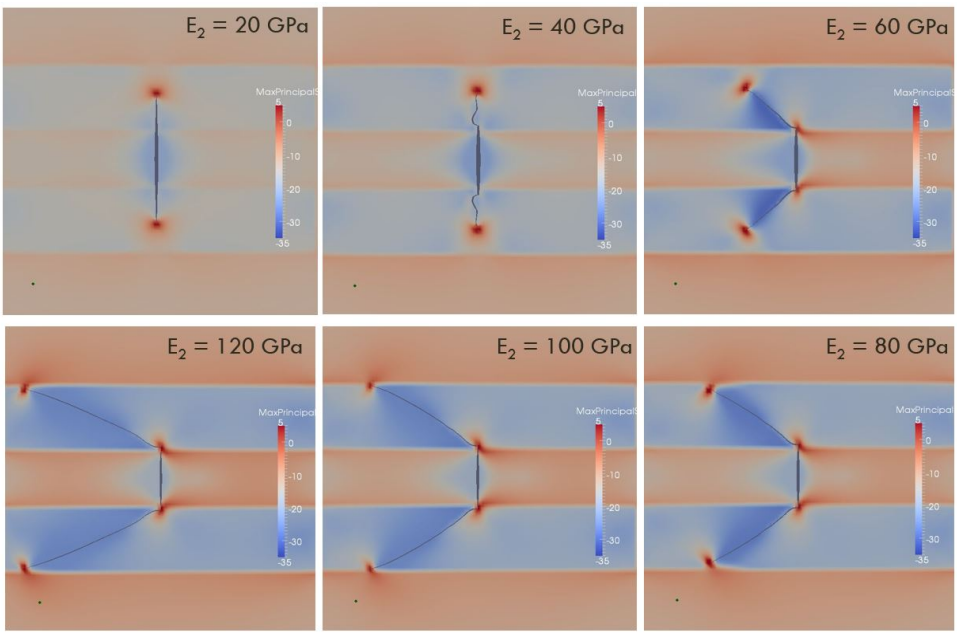

Figure 5.4: Effect of Young's modulus contrast on the fracture behaviour in a layered rock. The fracture initiates from the middle layer which is softer (E_1 = 10MPa, τ_{ult_1} = 4MPa, ν_1 = 0.2). The layer surrounding the mid layers are stiffer with varying Young's modulus as indicated on the figures.

From the reference case set presented in Table 5.1, for an ultimate tensile strength contrast (C_τ) of 3, we observe the variation in fracture propagation

with varying Young's modulus contrast in Figure 5.4. We observe that the fracture exhibits simple crossing across the layers for smaller contrast of Young's modulus and progresses to kink and deflect or turn for increasing contrasts. Another observation is that the fracture turning angle increases with the increase in the contrast.

In order to understand the reason for this behaviour we need to look at the in-situ stress state in each layer with varying contrast in Young's modulus. The stresses in the horizontal and the vertical directions at the centre of the layers are listed in Table 5.2.

Table 5.2: Stress state in each layer for varying contrast in Young's modulus

Young's modulus contrast (C_E)	Stress in Hard layer (in MPa)		Stress in Soft layer (in MPa)	
	σ_x	σ_y	σ_x	σ_y
1.0	-20.0	-20.0	-20.0	-20.0
2.0	-25.9	-21.3	-18.6	-20.8
3.0	-29.4	-21.9	-17.5	-21.1
4.0	-31.7	-22.2	-16.7	-21.2
5.0	-33.3	-22.4	-16.2	-21.3
6.0	-34.6	-22.6	-15.7	-21.3
7.0	-35.6	-22.7	-15.4	-21.3
8.0	-36.4	-22.8	-15.1	-21.4
9.0	-37.1	-22.9	-14.8	-21.4
10.0	-37.6	-22.9	-14.6	-21.4
12.0	-38.5	-23.0	-14.3	-21.4

The analogy for the layered rock formation can be a set of springs connected in parallel so that they have the same deflection but varying loads depending o the stiffness of each spring. When the layered rock formation is subjected to a compressive load in the horizontal direction, the softer layer compresses more compared to the stiffer layer. In-order to maintain continuity of strain across the layers, the softer layer develops an induced tensile stress while the stiffer layer develops an induced compressive stress. As the Young's modulus contrast increases, these induced stresses become more dominant. On the other hand, the loading in the vertical direction has very little effect on the in-situ stresses as it can be assumed to be set of springs connected in series. We can observe from Table 5.2, that the in-situ stress state developed due to a high Young's modulus contrast between layers, prefers the fractures in the hard layer to be oriented in the horizontal direction while those in the softer layer propagate along the vertical direction.

Ultimate tensile strength variation

The ultimate tensile strength in the stiffer layer(τ_{ult_2}) is varied from 4.0 MPa to 20.0 MPa causing a variation in the contrast from 1 to 5. Figure 5.5 represents the variation in fracture behaviour with varying ultimate tensile strength contrast (C_τ) while having a uniform Young's modulus contrast of 4. The variation of the ultimate tensile strength has no bearing on the stress state in the layers but simply delays the fracture turning process in the hard layer. This is due to the fact that in stiffer layers with a higher ultimate tensile strength, more stress difference is required to overcome the increased resistance and turn the fracture from its initial inertial direction.

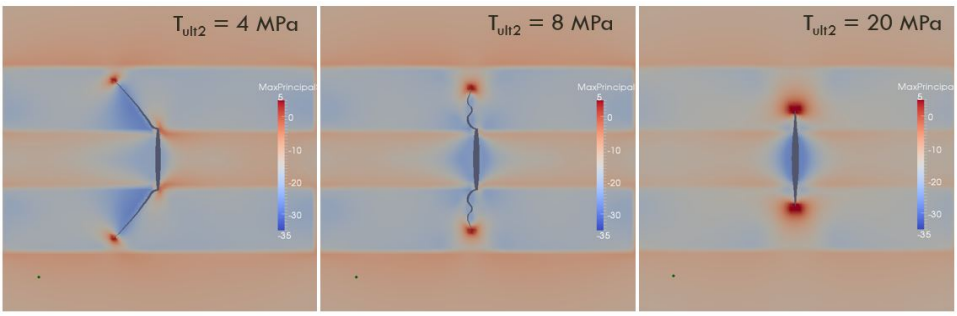

Figure 5.5: Effect of ultimate tensile strength modulus contrast on the fracture behaviour in a layered rock. The fracture initiates from the middle layer which is softer ($E_1 = 10\text{MPa}, \tau_{\text{ult}_1} = 4\text{MPa}, \nu_1 = 0.2$). The layer surrounding the mid layers are stiffer with varying ultimate tensile strength as indicated on the figures.

Poisson's ratio variation

Table 5.3: Fracture behaviour in a layered rock (with a Poisson's ratio of 0.1) propagating from a soft ($E_1 = 10\text{MPa}, \tau_{\text{ult}_1} = 4\text{MPa}, \nu_1 = 0.2$) to a hard layer with varying Young's modulus and ultimate tensile strength contrast. (C-crossing, D-Deflection, K-Kinking, A-Arrest)

		Young's modulus contrast (C_E)													
		1	2	2.5	3	3.5	4	4.5	5	6	7	8	9	10	12
τ_{ult} contrast	1	C	C	K	K	D	D	D	D	D	D	D	D	D	D
	2	C	C	C	K	K	K	D	D	D	D	D	D	D	D
	3	C	C	C	C	K	K	K	K	K	D	D	D	D	D
	4	C	C	C	C	K	K	K	K	K	D	D	D	D	D
	5	C	C	C	C	C	K	K	K	K	D	D	D	D	D

Table 5.4: Fracture behaviour in a layered rock (with a Poisson's ratio of 0.3) propagating from a soft ($E_1 = 10\text{MPa}, \tau_{\text{ult}_1} = 4\text{MPa}, \nu_1 = 0.2$) to a hard layer with varying Young's modulus and ultimate tensile strength contrast. (C-crossing, D-Deflection, K-Kinking, A-Arrest)

		Young's modulus contrast (C_E)													
		1	2	2.5	3	3.5	4	4.5	5	6	7	8	9	10	12
τ_{ult} contrast	1	C	C	K	D	D	D	D	D	D	D	D	D	D	D
	2	C	C	K	K	K	D	D	D	D	D	D	D	D	D
	3	C	C	C	K	K	K	D	D	D	D	D	D	D	D
	4	C	C	C	C	K	K	K	D	D	D	D	D	D	D
	5	C	C	C	C	K	K	K	K	D	D	D	D	D	D

The range of Poisson's ratio in sedimentary rocks is limited from 0.2 to 0.35 (Jumikis, 1979; Jaeger et al., 2009). To understand the effect of Poisson's ratio variation across layers on the fractures in a layered rock formation, we consider two cases with a Poisson's ratio of 0.1 and 0.3. From the results in Tables 5.3 and 5.4, we can observe that the Poisson's ratio variation has a very minor effect on the fracture behaviour. An increase in Poisson's ratio in the stiffer layer causes a decrease in the compressive strain in the horizontal direction in the stiffer layer. This in turn results in more induced horizontal stresses and prefers the fractures to orient much more in the horizontal direction, while the inverse is true for a reduced Poisson's ratio.

5.3.2 Influence of reservoir properties

Next we look at the influence of reservoir level properties (non-material properties) on the fracture orientation in layered reservoirs.

Layer thickness

Table 5.5: Fracture behaviour in a layered rock (Effect of a Thicker layer) propagating from a soft ($E_1 = 10\text{MPa}, \tau_{\text{ult}_1} = 4\text{MPa}, \nu_1 = 0.2$) to a hard layer with varying Young's modulus and ultimate tensile strength contrast. (C-crossing, D-Deflection, K-Kinking, A-Arrest)

		Young's modulus contrast (C_E)													
		1	2	2.5	3	3.5	4	4.5	5	6	7	8	9	10	12
τ_{ult} contrast	1	C	C	C	C	C	K	K	D	D	D	D	D	D	D
	2	C	C	C	C	C	C	C	K	K	D	D	D	D	D
	3	C	C	C	C	C	C	C	C	K	K	D	D	D	D
	4	C	C	C	C	C	C	C	C	C	K	K	D	D	D
	5	C	C	C	C	C	C	C	C	C	K	K	K	K	K

Table 5.6: Fracture behaviour in a layered rock (Effect of a Thin layer) propagating from a soft ($E_1 = 10\text{MPa}, \tau_{\text{ult}_1} = 4\text{MPa}, \nu_1 = 0.2$) to a hard layer with varying Young's modulus and ultimate tensile strength contrast. (C-crossing, D-Deflection, K-Kinking, A-Arrest)

		Young's modulus contrast (C_E)													
		1	2	2.5	3	3.5	4	4.5	5	6	7	8	9	10	12
τ_{ult} contrast	1	C	C	D	D	D	A	A	A	A	A	A	A	A	A
	2	C	C	D	D	D	D	D	D	A	A	A	A	A	A
	3	C	C	K	D	D	D	D	D	D	D	D	A	A	A
	4	C	C	C	K	D	D	D	D	D	D	D	D	A	A
	5	C	C	C	K	D	D	D	D	D	D	D	D	D	A

In all the previous cases, the rock formation had five layers with equal thickness. However in real fields, the thickness of the layers vary drastically depending on the mineral deposition timeline. We consider two different cases a) the softer layer with a thickness of 1 m is surrounded by stiffer layers of thickness of 2 m each b) the softer layer has two adjoining stiffer layers with a thickness of 0.4 m.

We can observe stark contrasts in the fracture behaviour with varying layer thickness (Tables 5.1, 5.5 and 5.6). In the first case with thicker stiffer layers, the overall stiffness of the layered rock formation is increased as a result, the combined compressive strain of the rock formation is closer to the strain in the stiffer layer. This results in a lowering of the induced compressive stresses in the stiffer layer while increasing the induced tensile stresses in the softer layer compared to the reference case. Hence the tendency of the fractures to turn in the stiffer layers is reduced.

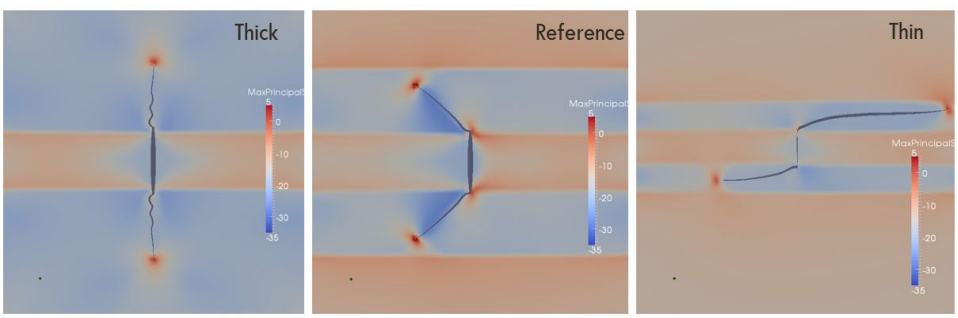

Figure 5.6: Effect of layer thickness on the fracture behaviour in a layered rock. Fracture initiates from the middle layer which is softer ($E_1 = 10\text{MPa}, \tau_{\text{ult}_1} = 4\text{MPa}, \nu_1 = 0.2$). The layer surrounding the mid layers are stiffer with a Young's modulus contrast of 6 and a ultimate tensile strength contrast of 2.

For a test case with thin stiff layers, the induced compressive stresses in the stiffer layers are much larger as the strain of the overall formation is closer to the strain of the softer layer. Hence the fracture completely turns and gets arrested in the thin stiff layers. This behaviour of fracture is depicted in Figure 5.6, which corresponds to a Young's modulus contrast (C_E) of 6 and a ultimate tensile strength contrast (C_τ) of 2.

Lithostatic stress

There are two different scenarios for analysing the effect of lithostatic stress on the fracture behaviour in layered rocks: a) Depth Effect: Variation of lithostatic stresses in both directions b) Anisotropy effect: Variation of lithostatic stress relative to one direction.

Table 5.7: Fracture behaviour in a layered rock (with a Lithostatic stress of 10 MPa) propagating from a soft ($E_1 = 10\text{MPa}, \tau_{\text{ult}_1} = 4\text{MPa}, \nu_1 = 0.2$) to a hard layer with varying Young's modulus and ultimate tensile strength contrast. (C-crossing, D-Deflection, K-Kinking, A-Arrest)

		Young's modulus contrast (C_E)													
		1	2	2.5	3	3.5	4	4.5	5	6	7	8	9	10	12
τ_{ult} contrast	1	C	C	C	K	K	D	D	D	D	D	D	D	D	D
	2	C	C	C	C	K	K	K	K	D	D	D	D	D	D
	3	C	C	C	C	C	C	K	K	K	D	D	D	D	D
	4	C	C	C	C	C	C	K	K	K	K	D	D	D	D
	5	C	C	C	C	C	C	C	C	K	K	K	K	D	D

Table 5.8: Fracture behaviour in a layered rock (with a Lithostatic stress of 30 MPa) propagating from a soft ($E_1 = 10\text{MPa}, \tau_{\text{ult}_1} = 4\text{MPa}, \nu_1 = 0.2$) to a hard layer with varying Young's modulus and ultimate tensile strength contrast. (C-crossing, D-Deflection, K-Kinking, A-Arrest)

		Young's modulus contrast (C_E)													
		1	2	2.5	3	3.5	4	4.5	5	6	7	8	9	10	12
τ_{ult} contrast	1	C	C	K	K	D	D	D	D	D	D	D	D	D	D
	2	C	C	K	K	K	D	D	D	D	D	D	D	D	D
	3	C	C	C	C	K	K	K	D	D	D	D	D	D	D
	4	C	C	C	C	K	K	K	D	D	D	D	D	D	D
	5	C	C	C	C	C	C	K	K	D	D	D	D	D	D

Depth effect To analyse the fracture behaviour with depth effect we consider two test cases with a uniform lithostatic stress of 10 MPa and 30 MPa in both

the directions which corresponds to depths of 400 m and 1200 m respectively. From Tables 5.7 and 5.8, we can observe that the fracture turning behaviour is predominant in deeper reservoirs. This is due to the fact that in shallow reservoirs the overburden stresses are lower, resulting in differences in the strain between the layers and hence lower induced stresses. This results in fractures remaining in its vertical plane until a much higher Young's modulus contrast between the layers.

Table 5.9: Fracture behaviour in a layered rock (with a Lithostatic stress contrast of 20%) propagating from a soft ($E_1 = 10\text{MPa}, \tau_{\text{ult}_1} = 4\text{MPa}, \nu_1 = 0.2$) to a hard layer with varying Young's modulus and ultimate tensile strength contrast. (C-crossing, D-Deflection, K-Kinking, A-Arrest)

		Young's modulus contrast (C_E)													
		1	2	2.5	3	3.5	4	4.5	5	6	7	8	9	10	12
τ_{ult} contrast	1	C	C	C	C	C	K	K	D	D	D	D	D	D	D
	2	C	C	C	C	C	K	K	K	K	D	D	D	D	D
	3	C	C	C	C	C	C	C	C	K	K	D	D	D	D
	4	C	C	C	C	C	C	C	C	K	K	K	D	D	D
	5	C	C	C	C	C	C	C	C	C	C	K	K	D	D

Table 5.10: Fracture behaviour in a layered rock (with a Lithostatic stress contrast of 50%) propagating from a soft ($E_1 = 10\text{MPa}, \tau_{\text{ult}_1} = 4\text{MPa}, \nu_1 = 0.2$) to a hard layer with varying Young's modulus and ultimate tensile strength contrast. (C-crossing, D-Deflection, K-Kinking, A-Arrest)

		Young's modulus contrast (C_E)													
		1	2	2.5	3	3.5	4	4.5	5	6	7	8	9	10	12
τ_{ult} contrast	1	C	C	C	C	C	C	C	C	C	C	C	C	C	C
	2	C	C	C	C	C	C	C	C	C	C	C	C	C	C
	3	C	C	C	C	C	C	C	C	C	C	C	C	C	C
	4	C	C	C	C	C	C	C	C	C	C	C	C	C	C
	5	C	C	C	C	C	C	C	C	C	C	C	C	C	C

Anisotropy effect The lithostatic stresses can also vary significantly in horizontal and vertical direction. In general the vertical overburden stress is slightly higher than the horizontal stresses. In this case, where the maximum compressive stress is along the vertical direction, the fracture has a greater tendency to align itself along the vertical direction. This phenomenon is shown in Tables 5.9 and 5.10. For significant anisotropies (>30%), i.e. when the differences in the lithostatic stresses between the directions is much greater than the induced stresses on the layers, the fractures always aligns in the vertical direction

irrespective of the layering effect and the contrast in mechanical properties.

Bedding plane orientation

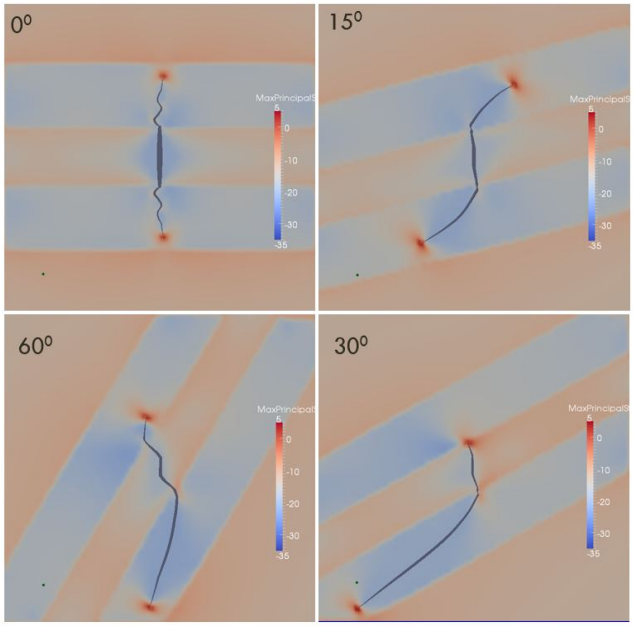

Figure 5.7: Effect of bedding plane orientation on the fracture behaviour in a layered rock.The fracture initiates from the middle layer which is softer ($E_1 = 10\text{MPa}, \tau_{\text{ult}_1} = 4\text{MPa}, \nu_1 = 0.2$).

In this subsection, we look at the effect of bedding plane orientation on the fracture behaviour. The bedding planes are oriented at 15°, 30°, 60° with respect to the horizontal direction. When a uniform lithostatic stress is applied in both the directions, the maximum compressive stress direction in the stiffer layer is along the bedding plane orientation. As the bedding plane angle increases, the fracture needs to turn by much smaller angles to align itself along the maximum compressive stress direction. Hence for layers with steep bedding plane orientation, the fractures are contained within the stiffer layer even for small contrast in the rock material properties as seen in Tables 5.11, 5.12 and 5.13.

5.3.3 Effect of fracture initiation location

We invert the reference case to understand the fracture behaviour with the change in the fracture initiation layer. In this test case, the fracture originates in a stiffer layer and is surrounded by softer layers. The different fracture

Table 5.11: Fracture behaviour in a layered rock (with a bedding plane orientation of 15°) propagating from a soft ($E_1 = 10\text{MPa}, \tau_{\text{ult}_1} = 4\text{MPa}, \nu_1 = 0.2$) to a hard layer with varying Young's modulus and ultimate tensile strength contrast. (C-crossing, D-Deflection, K-Kinking, A-Arrest)

		Young's modulus contrast (C_E)													
		1	2	2.5	3	3.5	4	4.5	5	6	7	8	9	10	12
τ_{ult} contrast	1	C	D	D	D	D	D	D	A	A	A	A	A	A	A
	2	C	D	D	D	D	D	D	D	D	A	A	A	A	A
	3	C	C	D	D	D	D	D	D	D	D	A	A	A	A
	4	C	C	D	D	D	D	D	D	D	D	A	A	A	A
	5	C	C	D	D	D	D	D	D	D	D	D	D	A	A

Table 5.12: Fracture behaviour in a layered rock (with a bedding plane orientation of 30°) propagating from a soft ($E_1 = 10\text{MPa}, \tau_{\text{ult}_1} = 4\text{MPa}, \nu_1 = 0.2$) to a hard layer with varying Young's modulus and ultimate tensile strength contrast. (C-crossing, D-Deflection, K-Kinking, A-Arrest)

		Young's modulus contrast (C_E)													
		1	2	2.5	3	3.5	4	4.5	5	6	7	8	9	10	12
τ_{ult} contrast	1	C	D	D	D	D	A	A	A	A	A	A	A	A	A
	2	C	D	D	D	D	D	D	D	A	A	A	A	A	A
	3	C	C	D	D	D	D	D	D	D	A	A	A	A	A
	4	C	C	D	D	D	D	D	D	D	D	A	A	A	A
	5	C	C	D	D	D	D	D	D	D	D	D	A	A	A

Table 5.13: Fracture behaviour in a layered rock (with a bedding plane orientation of 60°) propagating from a soft ($E_1 = 10\text{MPa}, \tau_{\text{ult}_1} = 4\text{MPa}, \nu_1 = 0.2$) to a hard layer with varying Young's modulus and ultimate tensile strength contrast. (C-crossing, D-Deflection, K-Kinking, A-Arrest)

		Young's modulus contrast (C_E)													
		1	2	2.5	3	3.5	4	4.5	5	6	7	8	9	10	12
τ_{ult} contrast	1	C	D	D	D	A	A	A	A	A	A	A	A	A	A
	2	C	D	D	D	D	D	D	A	A	A	A	A	A	A
	3	C	D	D	D	D	D	D	D	A	A	A	A	A	A
	4	C	D	D	D	D	D	D	D	D	D	A	A	A	A
	5	C	D	D	D	D	D	D	D	D	D	D	A	A	A

behaviours associated with this test case are: Crossing (denoted by C with white colour), Kinking (K with yellow colour), Arrest (A with red colour). This is represented in Table 5.14 and Figure 5.8.

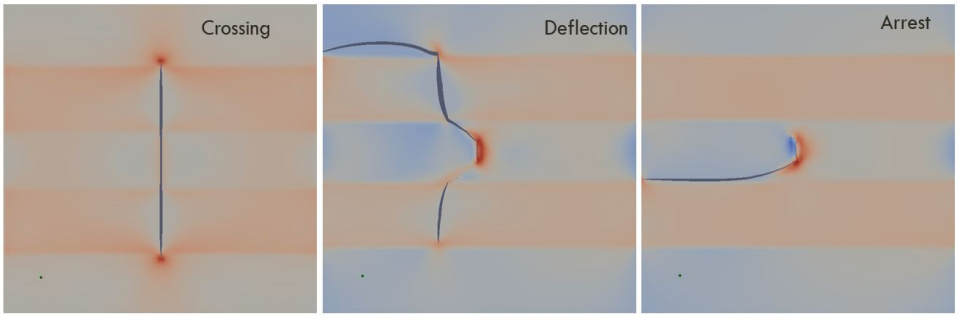

Figure 5.8: Different fracture behaviours when propagating from a harder layer to a softer layer. The fracture initiates from the middle layer which is stiffer and propagates to the surrounding softer layers ($E_1 = 10\text{MPa}, \tau_{\text{ult}_1} = 4\text{MPa}, \nu_1 = 0.2$).

Similar to the observations by Gu et al.(Gu et al., 2006), we can see from Table.5.14 that the fracture height containment in the harder layer when it is surrounded by the softer layers. This is because the induced stresses vary within each layer. There is a higher induced compressive stress in the horizontal direction closer to the interface on the side of the harder layer. Hence fracture propagation is much more favourable in the horizontal direction.

Table 5.14: Fracture behaviour in a layered rock when propagating from a hard layer with varying Young's modulus and ultimate tensile strength contrast to a soft layer($E_1 = 10\text{MPa}, \tau_{\text{ult}_1} = 4\text{MPa}, \nu_1 = 0.2$).(C-crossing, D-Deflection, K-Kinking, A-Arrest)

		Young's modulus contrast (C_E)													
		1	2	2.5	3	3.5	4	4.5	5	6	7	8	9	10	12
τ_{ult} contrast	1	C	C	C	C	C	C	C	C	C	D	D	D	A	A
	2	C	C	C	C	C	C	C	C	C	C	C	D	D	A
	3	C	C	C	C	C	C	C	C	C	C	C	C	C	D
	4	C	C	C	C	C	C	C	C	C	C	C	C	C	C
	5	C	C	C	C	C	C	C	C	C	C	C	C	C	C

5.3.4 Effect of a thin layered formation

In all of the above considered cases the layered heterogeneity is considered at a metre scale level. However experimental observations show layering effect even at centimetre and millimetre scale (Passey et al., 2010; Mokhtari et al., 2014). Hence in this example we consider fracture propagation in a reservoir with multiple layers with each layer having a thickness of 20 cm.

The strain across this thin layered formation is more continuous than the thick layered formation. This causes the strain differences and the induced

stresses between the layers appear to be significantly lower. As a result, the fracture turning process is delayed. But the continuous change from small deflection in the stiffer layer and crossing behaviour in the softer layer causes the fracture to have a deflection with several kinks. This becomes a critical issue for the transport of the proppants. Proppants need enough aperture for them to access the fracture tip from the point of injection. This is severely affected due to the presence of such large number of kinks.

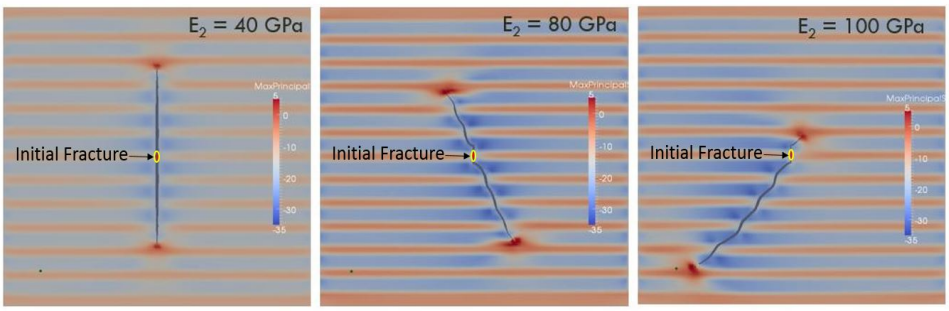

Figure 5.9: Fracture behaviours in a thin layered formation with each layer having a thickness of 20cm. The softer layers are with the following material properties $E_1 = 10\text{MPa}, \tau_{\text{ult}_1} = 4\text{MPa}, \nu_1 = 0.2$. While the stiffer layers have varying Young's modulus as indicated in the figures.

5.4 Comparison with experiments and field observations

It is difficult to validate these numerical models by comparing them to the field observations by any quantitative measure i.e. fracture length, fracture width. The real fields are formed through thousands of years which subject them to a variety of environmental conditions, resulting in different residual stresses, pre-existing fracture network all of which cannot be accounted for in a numerical model and predict an accurate quantitative measure. However it is possible to have a qualitative comparison of the numerical models with the experiments and the field observations. In the following example Brenner and Gudmundsson (2004) observed an outcrop from Kilve, UK with alternating layers of shale and limestone. The fracture network as interpreted by Boersma et al. (2019) shows that there are several fractures which originate inside the stiffer limestone layer do not propagate into the softer shale layers and tend to be arrested at the interface. The numerical models observe similar trends from Figure 5.8 and also from the Table 5.14. Although Table 5.14 predicts that the arrest occurs only at high mechanical contrasts between layers, it would be possible to have arrest at lower contrasts as well when the thickness of the

softer layer is much higher than the stiffer layer as is the case with this field observation.

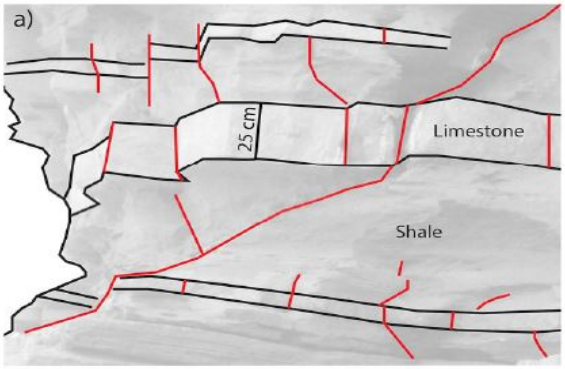

Figure 5.10: Interpreted fracture network on an outcrop in Kilve, UK consisting of alternating layers of stiff limestone and soft shales. Most of the fractures are found to be arrested in the boundary between the stiff and the soft layer.

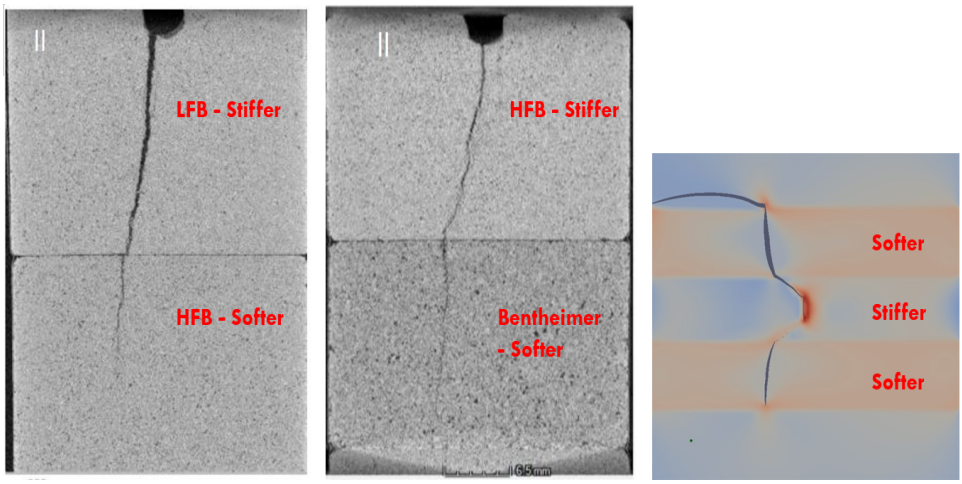

Figure 5.11: Comparison of numerical and experimental results of hydraulic fracture propagation in layered rocks from a stiffer layer into a softer layer. Propagation of hydraulic fracture from a) stiffer low porosity Fontaine Bleau (LFB) into softer high porosity Fontaine Bleau (HFB) b) stiffer HFB into softer Bentheimer Sandstone c) stiffer to softer layer in the MELP numerical model.

van Oosterhout (2019) has conducted hydraulic fracture experiments on artificially layered rocks with different mechanical contrasts. The hydraulic fractures are initiated at an indent on the top layer and propagated via water

injection in a triaxial cell. In Figure 5.11a, we observe a rock with alternating layers of stiffer low porosity Fontaine Bleau (LFB) and softer high porosity Fontaine Bleau (HFB) where the fractures initiate in the top LFB layer. The fractures are observed to deflect in the stiffer layer and become vertical in the softer layer. A similar behaviour of fracture is also observed in Figure 5.11b with alternating layers of stiffer high porosity Fontaine Bleau (HFB) and softer Bentheimer Sandstone. The numerical model shows a similar trend in Figure 5.11c, where the fracture initiated in the stiffer layer is deflected from the vertical direction in the stiffer layer but propagates in the vertical direction when they cross the interface into the softer layer.

5.5 Effect of Inclusions

Figure 5.12: (left) Inclusions in sandstone rocks from the upper part of of the Birket Qarun Formation at Gabal El-Lahun, Egypt. (Courtesy: Wanas Wanas (2008)). (right) Nodules developed in siltstone rocks of Talchir Formation in Dudhi Nala section, India. (Courtesy: Bhattacharya et al. Bhattacharya et al. (2002))

Inclusions are localised concentrations of authigenic mineral species (carbonate, silica, etc..) in a host rock Selles-Martinez (1996). These are commonly seen in the field observation of rocks as seen in Fig.5.12. Depending on the size, shape and composition of the inclusion bodies, they are classified as cementations, nodules, veins, inclusions. Due to the precipitation of minerals at specific locations in the rocks, they have a different composition and hence different material properties when compared to the surrounding rock material.

In this section, we try to model the behaviour of a hydraulic fracture in a rock with inclusions. We make use of a KGD like problem for this study as shown in Fig. 5.13. The host rock is assumed to have a Young's modulus of 40 GPa and a Poisson's ratio of 0.2. The ultimate tensile strength and toughness of the rock is 4 MPa and 120 N/m respectively. The porous rock is assumed to have a porosity of 0.1 and a permeability of 10^{-19}m^2. To represent the

inclusions we have varied the Young's modulus for certain patches in the rock as seen in Fig. 5.14. The formation is injected with a fluid having a viscosity of 0.01 Pa.s for 20 seconds.

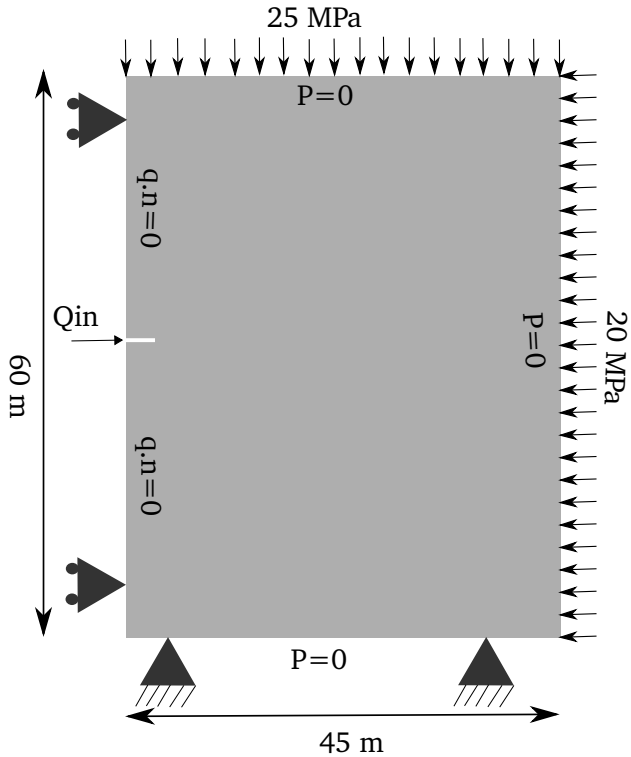

Figure 5.13: Hydraulic fracture problem with inclusions

Fig.5.14 a) illustrates the fracture propagation in an isotropic rock formation without any inclusions resulting in a fracture that propagates in the horizontal direction without any deflection. Fig.5.14 b) and c) shows the fracture propagation in the presence of inclusions which are harder than the rock formation. It can be seen that the fracture tends to move towards the inclusions and this tendency increases with the increase in the ratio of the Young's modulus. On the contrary Fig.5.14 d), e) and f) shows the fracture to move away from the the inclusions which are softer.

The reason for this nature in the behaviour of the fracture is due to the induced stresses developed in the two material system with contrasting Young's modulus. When the system with hard rock and a soft inclusion is subject to a compressive loading, the softer inclusions tend to compress much more relative to the rock due to its lower Young's modulus. But since the inclusions and the rock are interconnected, the rocks have to compress more than they compress in an isotropic scenario and the vice versa for inclusions. This causes

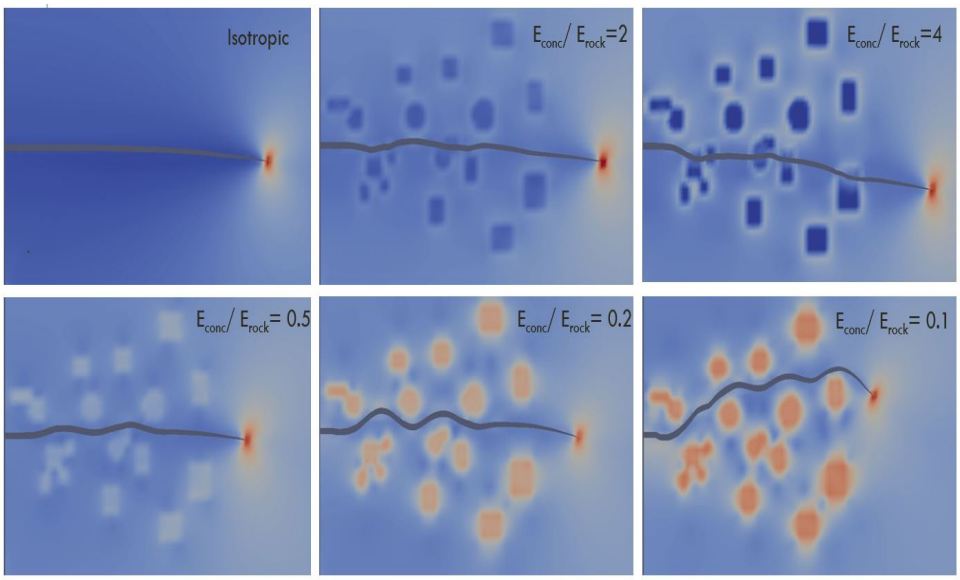

Figure 5.14: Behaviour of hydraulic fractures in the presence of inclusions.

an induced compressive stress in the rock in the region surrounding the inclusions. This additional induced compressive stress in the rock in the vicinity of a inclusion rock boundary creates a stress state that favours the fracture to go around the inclusions instead of propagating through them.

The presence of several inclusions in the rocks causes the fractures to have a torturous pathway which may result in difficulty in transport of proppants.

5.6 Multi-stage Hydraulic fracturing

The purpose of hydraulic fractures to enhance the permeability of unconventional reservoirs cannot be served with the help of a single fracture. In the engineering practice, the formation is drilled horizontally and with the help of plugs and perforatators tens to hundreds of fractures are created, clustered in several stages, to form a network of fractures which provide an alternate pathway for the flow of fluid. Each stage consists of a group of fractures which are spaced at regular intervals, where the growth of one fracture has an influence on the other due to stress redistributions. Hence it is vital to model this fracture network effect to understand the real implications of the presence of anisotropy and heterogeneity in the rocks.

In this example, we model a three stage hydraulic fracturing in a rock formation of 100 m × 100 m with a horizontal wellbore of diameter 1 m along the centre of the formation as seen in Fig.5.15 . Each stage consists of three fractures spaced 1 m apart from each other and the stages are separated by 5

m. Each fracture is injected with a fracturing fluid with a viscosity of 0.01 Pa.s for 20 seconds with a time step of 0.2 seconds. A compressive field of 20 MPa is applied in both the horizontal and the vertical directions. The formation has a Young's Modulus of 20 GPa and a Poisson's ration of 0.2, with a ultimate tensile strength of 6 MPa and a toughness of 120 N/m. The rock is assumed to have a porosity of 0.1 and a permeability of 10^{-19}m^2.

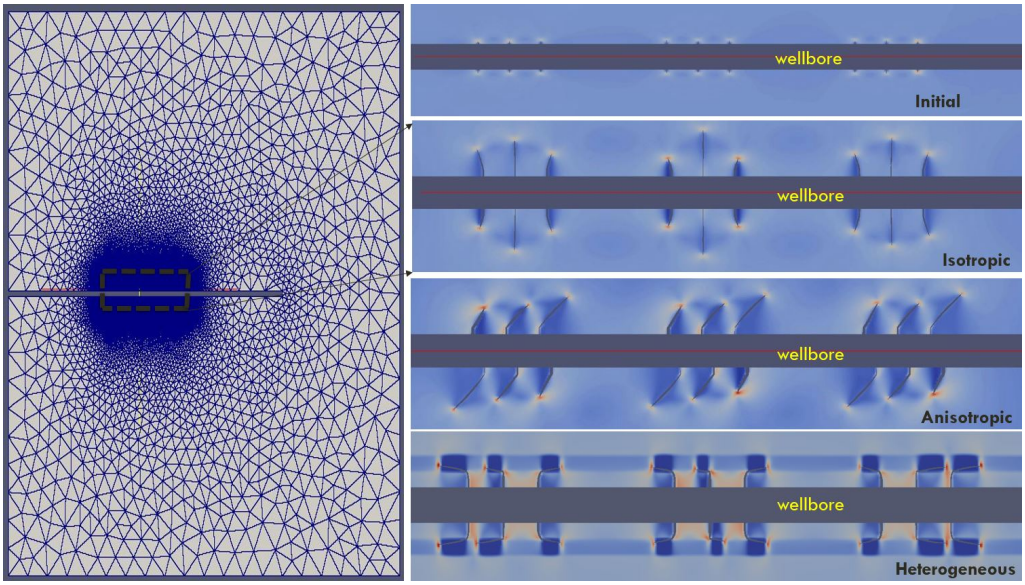

Figure 5.15: Three stage hydraulic fracture model with a well bore at the centre. On the right is a zoomed image of the region of interest showing the propagation of hydraulic fractures in isotropic, anisotropic and heterogeneous reservoir conditions

Under isotropic conditions, we observe a stress shadowing effect where the central fracture grows much longer compared to the outer fractures in every stage as seen in Fig.5.15. All three fractures in a single stage tend to grow simultaneously initially, after some time the expansion in the width of the two outer fractures causes the width of the central fracture to reduce. This thin width at the fracture mouth causes the fluid pressure, under constant injection rate, to raise which in turn helps the vertical growth of the central fracture. The effect of one stage on the other appears to be minimal since they are far apart from each other.

These isotropic conditions are perturbed to create an anisotropic field as described in Chapter 4. An anisotropy of 40% refers to condition when the value perpendicular to the grain orientation direction is 60% of the value parallel to the grain orientation direction. Similarly the current anisotropic problem is assumed to have an ultimate tensile strength anisotropy of 50% and a Young's modulus anisotropy of 50%. The grain orientation direction is assumed to be

40° to the horizontal. The anisotropy in the lithostatic stress field (vertical to horizontal) is assumed to be 20%. In Fig.5.15, we observe the behaviour of the multi-stage hydraulic fracture problem under these conditions. All the fractures tend to rotate and align themselves along the grain orientation direction, which inturn also diminishes the previously observed stress shadowing effect. Compared to an isotropic fracture network subject to same injection rates, we observe that the fractures achieve similar vertical heights but with increased length due to their orientation. But the turning nature of the fracture also leads to sharp kinks which would act as bottlenecks for fluid and proppant transport through the fracture.

The heterogeneity case is modelled with a stiff layer of 0.5 m thick and has a Young's modulus of 100 GPa and an ultimate tensile strength of 12 MPa. Although both the layers are homogeneous individually, this causes a heterogeneous reservoir condition. When the fracture network propagates in such heterogeneous conditions, all the fractures get arrested along the stiffer layer. This causes a hydraulic fracture height containment which cannot be understood by a model assuming isotropy. This arresting of fracture makes it impossible to extract oil and gas from the entire reservoir as all the fractures are concentrated in one single layer.

The objective of this example is to understand the behaviour of fracture networks and the effect of anisotropy and heterogeneity in the rocks. The real field scale scenario would have a much higher fracture spacing and stage spacing with a longer injection time making the fractures grow much longer. The scaled down version has been used since the cohesive-zone model is constrained by the fact that there needs to be at least 2-3 elements in the cohesive zone (∼157 mm) for its proper functioning. To be able to up-scale the simulation to the real field scale with the constraint on the mesh size, the code needs to be parallelised.

5.7 Conclusion

In this chapter, propagation of a hydraulic fracture in a reservoir with discrete and layered heterogeneity is studied. Fractures are observed to cross, kink, deflect or get arrested in a reservoir with strong layer interfaces. The Young's modulus contrast between the layers is the most important parameter in a layered reservoir with higher contrast causing the fracture to deviate from its initial path. This phenomenon is observed in an enhanced manner in deeper reservoirs with less stress anisotropy. Thin layers of stiff rock were observed to act as barriers for fracture propagation across layers. These barriers tend to become stronger with an increase in the bedding plane orientation. The inclusions which are stronger than the surrounding host rock tend to attract the fractures towards them whereas the softer inclusions were found to deflect

the fractures away from them. In the final example, a multi-stage hydraulic fracture network problem is investigated in an isotropic, anisotropic and heterogeneous layered reservoir.

Chapter 6

Conclusions

The objective of this thesis is to have a better understanding of hydraulic fracture propagation to create fractures in an efficient way which enhances the productivity of the reservoir and reduces the environmental impacts. To this extent, we have developed a numerical model which can simulate hydraulic fracturing in rocks which are anisotropic and heterogeneous in nature. The newly formulated model is based on the Enhanced Local Pressure (ELP) proposed by Remij et al. (2015a) but takes into account the reservoir pore pressure increase due to fracture leak-off. In this way a more realistic fracture model is obtained, especially for more permeable formations. The two-dimensional numerical model is based on extended finite element (XFEM) method and makes use of the Biot theory of poro-elasticity and Darcy's law for fluid flow through porous media.

6.1 Conclusions

In Chapter 2, a parametric study on the standard Khristianovich-Geertsma-de klerk (KGD) problem is conducted with the help of the ELP model. As expected the controllable parameters such as fracture fluid viscosity and the injection flow rate had a large influence on the fracture propagation. The parametric study was also conducted with several uncontrollable parameters which are based on the material properties of the rocks. Among them, Young's modulus and ultimate tensile strength were found out to be the most important parameters affecting fracture propagation. This study identified the dominant parameters which can be perturbed in the further chapters to understand the anisotropy and heterogeneity effects.

In Chapter 3, we propose a modified enhanced local pressure (MELP) model that can be used for the accurate modelling of the hydraulic fracturing process in permeable rocks, such as sandstones, while still retaining the advantages

proposed in the ELP model for modelling of near impermeable rocks, such as shales. The pressure gradient near the fracture surface is obtained analytically using Terzaghi's consolidation equation thereby eliminating the need of a fine mesh in the region. The MELP model accurately resolves the pore pressure distribution in the rock formation surrounding the fractures. This is demonstrated by comparing the MELP solution for a 1-D consolidation problem with the analytical approximation. The MELP model also significantly improves the leak-off prediction by coupling the fluid leak-off with the pressure in the formation. The effect of this improved leak-off model on a single fracture and a cluster of hydraulic fractures is demonstrated with the help of numerical examples. The MELP model is particularly advantageous for heterogeneous rocks with highly varying permeability layers and modelling of thief zones (i.e. thin layers of relatively high permeability) within the reservoir. In these scenarios, the MELP model can be used with a uniform mesh across the layers irrespective of the permeability differences.

Chapter 4 discusses the effect of anisotropy on hydraulic fractures. A new criterion for fracture propagation in anisotropic porous media is proposed by combining the Tsai-Hill failure criterion with the Camacho-Ortiz propagation criterion. The orientation of the grains along a plane caused by weathering, erosion was considered to be the source of anisotropy in the material properties. Introducing an anisotropic Young's modulus results in fractures orienting perpendicular to the grain orientation direction, while anisotropic ultimate tensile strength tends to orient the fractures along the grain orientation direction. The anisotropy in the in-situ stresses causes the fractures to propagate parallel to the maximum stress direction. The final orientation of the fracture is dependent on the different degree of anisotropies in all these parameters and also on the angle between the grain orientation direction and the initial fracture orientation. By varying the degree of anisotropy in each of these parameters along with the grain orientation direction, different regimes were identified in which the anisotropy in the material properties influence the fracture orientation more than the in-situ stress anisotropy.

In Chapter 5, we model the propagation of hydraulic fractures in layered heterogeneous reservoirs. The model assumes that the bonds between the different layers are strong enough to ensure that interfacial fractures are not initiated. The layered nature of the reservoir causes the fracture either to cross, kink, deflect or arrest when it encounters an interface. Out of these four phenomena, the specific behaviour of a fracture is dependent on the differences in the material properties (Young's modulus and ultimate tensile strength) between the layers and also on the reservoir properties (layer thickness, in-situ stresses and bedding plane orientation). An increase in the contrast in Young's modulus causes the fractures to increasingly deflect or get arrested in the stiffer layers. This phenomenon is enhanced when the relatively stiffer layers are thin-

ner and present in deeper reservoirs (higher in-situ stresses). The fracture path is modelled in the presence of inclusions which are local concentrations of minerals. The fractures were observed to move towards these inclusions when they are harder than the rock formation and move away from the inclusions which were softer. These localised effects are observed only when the fracture tip is in the vicinity of an inclusion. We also simulate a multi-stage hydraulic fracture scenario in isotropic, anisotropic and heterogeneous reservoir conditions to exhibit the versatility of the model. We observe that both the individual fracture propagation as well as the fracture network formation is significantly affected by the presence of anisotropy and heterogeneity.

6.2 Outlook

While the current work makes progress towards simulating hydraulic fracturing in realistic reservoir-like conditions, there are still several significant challenges. The first and foremost being extending the current two-dimensional model to a three dimensional framework. Complications arise in tracking of the fracture surfaces and the fracture propagation front when extending an extended finite element model to a 3-D framework. Several works (Sethian, 1996; Moës et al., 2002; Sukumar et al., 2003) make use of level sets to overcome this problem. 3D hydraulic fracture models with various constraints were proposed by Gupta and Duarte (2016), Remij (2017) and Dontsov and Peirce (2017). Modelling of the flow within the 3-D volume of the fracture with moving boundaries has been challenging due to the presence of kinks which needed to be smoothened (Gupta and Duarte, 2016). Constraints on the mesh size are imposed by the cohesive zone model which requires at least two to three elements in the cohesive zone region (Barenblatt, 1962). In order to overcome this constraint and up-scale the model, we need to parallelize the code to obtain the simulations results in a reasonable computational time.

The effects of anisotropy and heterogeneity on hydraulic fractures were studied in Chapter 4 and 5 respectively. The current study was conducted on a parametric space by perturbing the isotropic values observed in whitby mudstone. It would be helpful to extend the study for other reservoirs like Marcellus, Bakken, Barnett shale (Vermylen, 2011; Druyff, 1990; Sone and Zoback, 2013). In the future work, the model can be used in combination with experimental data of the rock material properties which are anisotropic and heterogeneous instead of perturbing isotropic values. The challenge lies in the fact all the required experimental data for the simulation cannot be obtained from one single study. We have to collate the data for a specific rock type from various literatures.

Observing the hydraulic fracture patterns in a layered reservoir in Chapter 5 leads to interesting observations. While we can explain the phenomena

of crossing, deflection and arrest, the reason for the kinking patterns remain unexplained. It is always observed in the transition from fracture crossing to fracture deflection. One explanation could be that the stress field is simply not strong enough to deflect the fracture and determine its direction, so that a wavy pattern occurs. The study could be extended to weakly bonded layers by adding another possible fracture propagation path along the interfaces of the layers. It is also extremely important to validate these observations from the numerical models by comparing them with experimental work.

A better fluid flow model in the fracture tip vicinity along with investigation on the presence of a fluid lag near the tip is vital to get an accurate hydraulic fracture model. The current model makes use of a cubic law to describe the flow in the fracture. This does not hold well in the cohesive zone region near the fracture tip. The current model assumes single fluid flow, but multi fluid (fracking fluid, pore fluid) flow could be included in future work.

Appendix A

Expression for matrices in the MELP solution

In this appendix we present computation of the matrices used in the final solution (Eq. 3.45)

$$\boldsymbol{J}_{\hat{\mathrm{u}}\hat{\mathrm{u}}} = \int_{\Omega_\mathrm{e}} \boldsymbol{B}^\mathrm{T}\boldsymbol{C}\boldsymbol{B}\ d\Omega_\mathrm{e} \qquad \boldsymbol{J}_{\hat{\mathrm{u}}\tilde{\mathrm{u}}} = \int_{\Omega_\mathrm{e}} H_{\Gamma_\mathrm{d}}\boldsymbol{B}^\mathrm{T}\boldsymbol{C}\boldsymbol{B}\ d\Omega_\mathrm{e}$$

$$\boldsymbol{J}_{\hat{\mathrm{u}}\hat{\mathrm{p}}} = -\int_{\Omega_\mathrm{e}} \alpha\boldsymbol{B}^\mathrm{T}\boldsymbol{m}\boldsymbol{H}\ d\Omega_\mathrm{e} \qquad \boldsymbol{J}_{\hat{\mathrm{u}}\tilde{\mathrm{p}}} = -\int_{\Omega_\mathrm{e}} \alpha H_{\Gamma_\mathrm{d}}\boldsymbol{B}^\mathrm{T}\boldsymbol{m}\boldsymbol{H}\ d\Omega_\mathrm{e}$$

$$\boldsymbol{J}_{\tilde{\mathrm{u}}\tilde{\mathrm{u}}} = \int_{\Omega_\mathrm{e}} H_{\Gamma_\mathrm{d}}^2\boldsymbol{B}^\mathrm{T}\boldsymbol{C}\boldsymbol{B}\ d\Omega_\mathrm{e} + \int_{\Gamma_\mathrm{d}} h^2\boldsymbol{N}^T\boldsymbol{T}_d\boldsymbol{N}d\Gamma_\mathrm{d} \qquad \boldsymbol{J}_{\hat{\mathrm{u}}\mathrm{p}_\mathrm{d}} = 0$$

$$\boldsymbol{J}_{\tilde{\mathrm{u}}\hat{\mathrm{u}}} = \int_{\Omega_\mathrm{e}} H_{\Gamma_\mathrm{d}}\boldsymbol{B}^\mathrm{T}\boldsymbol{C}\boldsymbol{B}\ d\Omega_\mathrm{e} \qquad \boldsymbol{J}_{\tilde{\mathrm{u}}\hat{\mathrm{p}}} = -\int_{\Omega_\mathrm{e}} \alpha H_{\Gamma_\mathrm{d}}\boldsymbol{B}^\mathrm{T}\boldsymbol{m}\boldsymbol{H}\ d\Omega_\mathrm{e}$$

$$\boldsymbol{J}_{\tilde{\mathrm{u}}\tilde{\mathrm{p}}} = -\int_{\Omega_\mathrm{e}} \alpha H_{\Gamma_\mathrm{d}}^2\boldsymbol{B}^\mathrm{T}\boldsymbol{m}\boldsymbol{H}\ d\Omega_\mathrm{e} \qquad \boldsymbol{J}_{\tilde{\mathrm{u}}\mathrm{p}_\mathrm{d}} = -\int_{\Gamma_\mathrm{d}} h\boldsymbol{N}^\mathrm{T}\boldsymbol{n}_\mathrm{d}\boldsymbol{V}\ d\Gamma_\mathrm{d}$$

$$\boldsymbol{J}_{\hat{\mathrm{p}}\hat{\mathrm{u}}} = -\int_{\Omega_\mathrm{e}} \alpha\boldsymbol{H}^\mathrm{T}\boldsymbol{m}^\mathrm{T}\boldsymbol{B}\ d\Omega_\mathrm{e} \qquad \boldsymbol{J}_{\hat{\mathrm{p}}\tilde{\mathrm{u}}} = -\int_{\Omega_\mathrm{e}} \alpha H_{\Gamma_\mathrm{d}}\boldsymbol{H}^\mathrm{T}\boldsymbol{m}^\mathrm{T}\boldsymbol{B}\ d\Omega_\mathrm{e}$$

$$\boldsymbol{J}_{\hat{\mathrm{p}}\hat{\mathrm{p}}} = \theta\triangle t(\boldsymbol{J}^{(1)}_{\hat{\mathrm{p}}\hat{\mathrm{p}}} + \boldsymbol{J}^{(3)}_{\hat{\mathrm{p}}\hat{\mathrm{p}}}) + \boldsymbol{J}^{(2)}_{\hat{\mathrm{p}}\hat{\mathrm{p}}} \qquad \boldsymbol{J}^{(1)}_{\hat{\mathrm{p}}\hat{\mathrm{p}}} = -\int_{\Omega_\mathrm{e}} \nabla\boldsymbol{H}^\mathrm{T}\frac{\boldsymbol{\kappa}}{\mu}\nabla\boldsymbol{H}\ d\Omega_\mathrm{e}$$

$$\boldsymbol{J}^{(2)}_{\hat{\mathrm{p}}\hat{\mathrm{p}}} = -\frac{1}{M}\int_{\Omega_\mathrm{e}} \boldsymbol{H}^\mathrm{T}\boldsymbol{H}\ d\Omega_\mathrm{e} \qquad \boldsymbol{J}^{(3)}_{\hat{\mathrm{p}}\hat{\mathrm{p}}} = -2C_\mathrm{a}\int_{\Gamma_d} \boldsymbol{H}^\mathrm{T}\boldsymbol{H}\ d\Gamma_\mathrm{d}$$

$$\boldsymbol{J}_{\hat{\mathrm{p}}\tilde{\mathrm{p}}} = \theta\triangle t(\boldsymbol{J}^{(1)}_{\hat{\mathrm{p}}\tilde{\mathrm{p}}} + \boldsymbol{J}^{(3)}_{\hat{\mathrm{p}}\tilde{\mathrm{p}}}) + \boldsymbol{J}^{(2)}_{\hat{\mathrm{p}}\tilde{\mathrm{p}}} \qquad \boldsymbol{J}^{(1)}_{\hat{\mathrm{p}}\tilde{\mathrm{p}}} = -\int_{\Omega_\mathrm{e}} H_{\Gamma_\mathrm{d}}\nabla\boldsymbol{H}^\mathrm{T}\frac{\boldsymbol{\kappa}}{\mu}\nabla\boldsymbol{H}\ d\Omega_\mathrm{e}$$

$$\boldsymbol{J}^{(2)}_{\hat{\mathrm{p}}\tilde{\mathrm{p}}} = -\frac{1}{M}\int_{\Omega_\mathrm{e}} H_{\Gamma_\mathrm{d}}\boldsymbol{H}^\mathrm{T}\boldsymbol{H}\ d\Omega_\mathrm{e} \qquad \boldsymbol{J}^{(3)}_{\hat{\mathrm{p}}\tilde{\mathrm{p}}} = -C_\mathrm{a}\int_{\Gamma_d} (H_{\Gamma_{\mathrm{d}^+}} + H_{\Gamma_{\mathrm{d}^-}})\boldsymbol{H}^\mathrm{T}\boldsymbol{H}\ d\Gamma_\mathrm{d}$$

$$\boldsymbol{J}_{\hat{\mathrm{p}}\mathrm{p}_\mathrm{d}} = 2C_\mathrm{a}\int_{\Gamma_d} \boldsymbol{H}^\mathrm{T}\boldsymbol{V}\ d\Gamma_\mathrm{d} \qquad \boldsymbol{J}_{\tilde{\mathrm{p}}\mathrm{p}_\mathrm{d}} = C_\mathrm{a}\int_{\Gamma_d} (H_{\Gamma_{\mathrm{d}^+}} + H_{\Gamma_{\mathrm{d}^-}})\boldsymbol{H}^\mathrm{T}\boldsymbol{V}\ d\Gamma_\mathrm{d}$$

$$\boldsymbol{J}_{\tilde{\mathrm{p}}\hat{\mathrm{u}}} = -\int_{\Omega_\mathrm{e}} \alpha H_{\Gamma_\mathrm{d}}\boldsymbol{H}^\mathrm{T}\boldsymbol{m}^\mathrm{T}\boldsymbol{B}\ d\Omega_\mathrm{e} \qquad \boldsymbol{J}_{\tilde{\mathrm{p}}\tilde{\mathrm{u}}} = -\int_{\Omega_\mathrm{e}} \alpha H^2_{\Gamma_\mathrm{d}}\boldsymbol{H}^\mathrm{T}\boldsymbol{m}^\mathrm{T}\boldsymbol{B}\ d\Omega_\mathrm{e}$$

$$\boldsymbol{J}_{\tilde{\mathrm{p}}\hat{\mathrm{p}}} = \theta\triangle t(\boldsymbol{J}^{(1)}_{\tilde{\mathrm{p}}\hat{\mathrm{p}}} + \boldsymbol{J}^{(3)}_{\tilde{\mathrm{p}}\hat{\mathrm{p}}}) + \boldsymbol{J}^{(2)}_{\tilde{\mathrm{p}}\hat{\mathrm{p}}} \qquad \boldsymbol{J}^{(1)}_{\tilde{\mathrm{p}}\hat{\mathrm{p}}} = -\int_{\Omega_\mathrm{e}} H_{\Gamma_\mathrm{d}}\nabla\boldsymbol{H}^\mathrm{T}\frac{\boldsymbol{\kappa}}{\mu}\nabla\boldsymbol{H}\ d\Omega_\mathrm{e}$$

$$\boldsymbol{J}^{(2)}_{\tilde{\mathrm{p}}\hat{\mathrm{p}}} = -\frac{1}{M}\int_{\Omega_\mathrm{e}} H_{\Gamma_\mathrm{d}}\boldsymbol{H}^\mathrm{T}\boldsymbol{H}\ d\Omega_\mathrm{e} \qquad \boldsymbol{J}^{(3)}_{\tilde{\mathrm{p}}\hat{\mathrm{p}}} = -C_\mathrm{a}\int_{\Gamma_d} (H_{\Gamma_{\mathrm{d}^+}} + H_{\Gamma_{\mathrm{d}^-}})\boldsymbol{H}^\mathrm{T}\boldsymbol{H}\ d\Gamma_\mathrm{d}$$

$$\boldsymbol{J}_{\tilde{\mathrm{p}}\tilde{\mathrm{p}}} = \theta\triangle t(\boldsymbol{J}^{(1)}_{\tilde{\mathrm{p}}\tilde{\mathrm{p}}} + \boldsymbol{J}^{(3)}_{\tilde{\mathrm{p}}\tilde{\mathrm{p}}}) + \boldsymbol{J}^{(2)}_{\tilde{\mathrm{p}}\tilde{\mathrm{p}}} \qquad \boldsymbol{J}^{(1)}_{\tilde{\mathrm{p}}\tilde{\mathrm{p}}} = -\int_{\Omega_\mathrm{e}} H^2_{\Gamma_\mathrm{d}}\nabla\boldsymbol{H}^\mathrm{T}\frac{\boldsymbol{\kappa}}{\mu}\nabla\boldsymbol{H}\ d\Omega_\mathrm{e}$$

$$\boldsymbol{J}^{(2)}_{\tilde{\mathrm{p}}\tilde{\mathrm{p}}} = -\frac{1}{M}\int_{\Omega_\mathrm{e}} H^2_{\Gamma_\mathrm{d}}\boldsymbol{H}^\mathrm{T}\boldsymbol{H}\ d\Omega_\mathrm{e} \qquad \boldsymbol{J}^{(3)}_{\tilde{\mathrm{p}}\tilde{\mathrm{p}}} = -C_\mathrm{a}\int_{\Gamma_d} (H^2_{\Gamma_{\mathrm{d}^+}} + H^2_{\Gamma_{\mathrm{d}^-}})\boldsymbol{H}^\mathrm{T}\boldsymbol{H}\ d\Gamma_\mathrm{d}$$

$$\boldsymbol{J}_{\mathrm{p_d}\hat{\mathrm{p}}} = -2C_\mathrm{a}\int_{\Gamma_d} \boldsymbol{V}^\mathrm{T}\boldsymbol{H}d\Gamma_\mathrm{d} \qquad \boldsymbol{J}_{\mathrm{p_d}\tilde{\mathrm{p}}} = -C_\mathrm{a}\int_{\Gamma_d} (H_{\Gamma_{\mathrm{d}^+}} + H_{\Gamma_{\mathrm{d}^-}})\boldsymbol{V}^\mathrm{T}\boldsymbol{H}d\Gamma_\mathrm{d}$$

$$\boldsymbol{J}_{\mathrm{p_d}\tilde{\mathrm{u}}} = \boldsymbol{J}^{(1)}_{\mathrm{p_d}\tilde{\mathrm{u}}} + \theta\boldsymbol{J}^{(2)}_{\mathrm{p_d}\tilde{\mathrm{u}}} + \boldsymbol{J}^{(3)}_{\mathrm{p_d}\tilde{\mathrm{u}}} + \boldsymbol{J}^{(4)}_{\mathrm{p_d}\tilde{\mathrm{u}}} + (\boldsymbol{J}^{(5)}_{\mathrm{p_d}\tilde{\mathrm{u}}} + \boldsymbol{J}^{(6)}_{\mathrm{p_d}\tilde{\mathrm{u}}} + \boldsymbol{J}^{(7)}_{\mathrm{p_d}\tilde{\mathrm{u}}})\theta\triangle t$$

$$\boldsymbol{J}^{(2)}_{\mathrm{p_d}\tilde{\mathrm{u}}} = \int_{\Gamma_d} h\boldsymbol{V}^\mathrm{T}\boldsymbol{n}_\mathrm{d}\boldsymbol{N}(\hat{\boldsymbol{U}}^{\mathrm{t}+\triangle\mathrm{t}}_{\mathrm{j}-1} - \hat{\boldsymbol{U}}^\mathrm{t})\boldsymbol{t}_\mathrm{s}\frac{\partial\boldsymbol{N}}{\partial s}d\Gamma_\mathrm{d} \qquad \boldsymbol{J}^{(1)}_{\mathrm{p_d}\tilde{\mathrm{u}}} = \int_{\Gamma_d} h\boldsymbol{V}^\mathrm{T}\boldsymbol{n}_\mathrm{d}\boldsymbol{N}d\Gamma_\mathrm{d}$$

$$\boldsymbol{J}^{(3)}_{\mathrm{p_d}\tilde{\mathrm{u}}} = \int_{\Gamma_d} v_\mathrm{n}(H_{\Gamma_{\mathrm{d}^+}} + H_{\Gamma_{\mathrm{d}^-}})\boldsymbol{V}^\mathrm{T}\boldsymbol{t}_\mathrm{s}\frac{\partial\boldsymbol{N}}{\partial s}d\Gamma_\mathrm{d} \qquad \boldsymbol{J}^{(5)}_{\mathrm{p_d}\tilde{\mathrm{u}}} = h\int_{\Gamma_d} \frac{v_\mathrm{n}^2}{4\mu_\mathrm{d}}\frac{\partial\boldsymbol{V}^\mathrm{T}}{\partial s}\frac{\partial\boldsymbol{V}}{\partial s}\boldsymbol{P}_\mathrm{d}\boldsymbol{n}_\mathrm{d}\boldsymbol{N}d\Gamma_\mathrm{d}$$

$$\boldsymbol{J}^{(4)}_{\mathrm{p_d}\tilde{\mathrm{u}}} = \int_{\Gamma_d} (H_{\Gamma_{\mathrm{d}^+}} + H_{\Gamma_{\mathrm{d}^-}})\boldsymbol{V}^\mathrm{T}\boldsymbol{n}_\mathrm{d}\boldsymbol{N}\tilde{\boldsymbol{U}}\boldsymbol{t}_\mathrm{s}\frac{\partial\boldsymbol{N}}{\partial s}d\Gamma_\mathrm{d} \qquad \boldsymbol{J}^{(6)}_{\mathrm{p_d}\tilde{\mathrm{u}}} = h\int_{\Gamma_d} \frac{v_\mathrm{n}^2}{4\mu_\mathrm{d}}\boldsymbol{V}^\mathrm{T}\frac{\partial\boldsymbol{V}}{\partial s}\boldsymbol{P}_\mathrm{d}\boldsymbol{n}_\mathrm{d}\frac{\partial\boldsymbol{N}}{\partial s}d\Gamma_\mathrm{d}$$

$$\boldsymbol{J}^{(7)}_{\mathrm{p_d}\tilde{\mathrm{u}}} = h\int_{\Gamma_d} \frac{h}{K_\mathrm{f}}\boldsymbol{V}(\boldsymbol{P}^{\mathrm{t}+\triangle\mathrm{t}}_{\mathrm{d}_{\mathrm{j}-1}} - \boldsymbol{P}^\mathrm{t}_\mathrm{d})\boldsymbol{V}^\mathrm{T}\boldsymbol{n}_\mathrm{d}\boldsymbol{N}d\Gamma_\mathrm{d} \qquad \boldsymbol{J}_{\mathrm{p_d}\hat{\mathrm{u}}} = \int_{\Gamma_d} v_\mathrm{n}\boldsymbol{V}^\mathrm{T}\boldsymbol{t}_\mathrm{s}^\mathrm{T}\frac{\partial\boldsymbol{N}}{\partial s}d\Gamma_\mathrm{d}$$

$$\boldsymbol{J}_{\mathrm{p_d}\mathrm{p_d}} = (\boldsymbol{J}^{(1)}_{\mathrm{p_d}\mathrm{p_d}} + \boldsymbol{J}^{(3)}_{\mathrm{p_d}\mathrm{p_d}} + \boldsymbol{J}^{(4)}_{\mathrm{p_d}\mathrm{p_d}})\theta\triangle t + \boldsymbol{J}^{(2)}_{\mathrm{p_d}\mathrm{p_d}} \qquad \boldsymbol{J}^{(1)}_{\mathrm{p_d}\mathrm{p_d}} = 2C_\mathrm{a}\int_{\Gamma_d} \boldsymbol{V}^\mathrm{T}\boldsymbol{V}d\Gamma_\mathrm{d}$$

$$\boldsymbol{J}^{(2)}_{\mathrm{p_d}\mathrm{p_d}} = \int_{\Gamma_d} \frac{v_\mathrm{n}}{K_\mathrm{f}}\boldsymbol{V}^\mathrm{T}\boldsymbol{V}d\Gamma_\mathrm{d} \qquad \boldsymbol{J}^{(3)}_{\mathrm{p_d}\mathrm{p_d}} = \int_{\Gamma_d} \frac{v_\mathrm{n}^3}{12\mu_\mathrm{d}}\frac{\partial\boldsymbol{V}^\mathrm{T}}{\partial s}\frac{\partial\boldsymbol{V}}{\partial s}d\Gamma_\mathrm{d}$$

$$\boldsymbol{J}^{(4)}_{\mathrm{p_d}\mathrm{p_d}} = h\int_{\Gamma_d} \frac{v_\mathrm{n}^2}{4\mu_\mathrm{d}}\boldsymbol{V}^\mathrm{T}\frac{\partial\boldsymbol{V}^\mathrm{T}}{\partial s}\boldsymbol{P}_\mathrm{d}\boldsymbol{n}_\mathrm{d}\frac{\partial\boldsymbol{N}}{\partial s}d\Gamma_\mathrm{d}$$

$$\boldsymbol{f}_{\hat{\mathrm{u}}}^{\mathrm{ext}} = \int_{\Gamma_{\mathrm{t}}} \boldsymbol{N}^T \boldsymbol{t}_{\mathrm{p}}^{\mathrm{t}+\triangle\mathrm{t}} \, d\Gamma_{\mathrm{t}} \qquad \boldsymbol{f}_{\tilde{\mathrm{u}}}^{\mathrm{ext}} = \int_{\Gamma_{\mathrm{t}}} H_{\Gamma_{\mathrm{d}}} \boldsymbol{N}^T \boldsymbol{t}_{\mathrm{p}}^{\mathrm{t}+\triangle\mathrm{t}} \, d\Gamma_{\mathrm{t}}$$

$$\boldsymbol{f}_{\hat{\mathrm{p}}}^{\mathrm{ext}} = \int_{\Gamma_{\mathrm{q}}} \boldsymbol{H}^T \triangle t(\theta q_{\mathrm{p}_{\mathrm{j}-1}}^{\mathrm{t}+\triangle\mathrm{t}} + (1-\theta) q_{\mathrm{p}}^{\mathrm{t}}) d\Gamma_{\mathrm{q}} \qquad \boldsymbol{f}_{\tilde{\mathrm{p}}}^{\mathrm{ext}} = \int_{\Gamma_{\mathrm{q}}} H_{\Gamma_{\mathrm{d}}} \boldsymbol{H}^T \triangle t(\theta q_{\mathrm{p}_{\mathrm{j}-1}}^{\mathrm{t}+\triangle\mathrm{t}} + (1-\theta) q_{\mathrm{p}}^{\mathrm{t}}) d\Gamma_{\mathrm{q}}$$

$$\boldsymbol{f}_{\mathrm{p_d}}^{\mathrm{ext}} = \boldsymbol{V} Q_{\mathrm{in}}$$

$$\begin{aligned}\boldsymbol{f}_{\hat{\mathrm{u}}}^{\mathrm{int}} =& \boldsymbol{J}_{\hat{\mathrm{u}}\hat{\mathrm{u}}}(\theta \hat{\boldsymbol{u}}_{\mathrm{j}-1}^{\mathrm{t}+\triangle\mathrm{t}} + (1-\theta)\hat{\boldsymbol{u}}^{\mathrm{t}}) + \boldsymbol{J}_{\hat{\mathrm{u}}\tilde{\mathrm{u}}}(\theta \tilde{\boldsymbol{u}}_{\mathrm{j}-1}^{\mathrm{t}+\triangle\mathrm{t}} + (1-\theta)\tilde{\boldsymbol{u}}^{\mathrm{t}}) + \boldsymbol{J}_{\hat{\mathrm{u}}\hat{\mathrm{p}}}(\theta \hat{\boldsymbol{p}}_{\mathrm{j}-1}^{\mathrm{t}+\triangle\mathrm{t}} + (1-\theta)\hat{\boldsymbol{p}}^{\mathrm{t}}) \\ &+ \boldsymbol{J}_{\hat{\mathrm{u}}\tilde{\mathrm{p}}}(\theta \tilde{\boldsymbol{p}}_{\mathrm{j}-1}^{\mathrm{t}+\triangle\mathrm{t}} + (1-\theta)\tilde{\boldsymbol{p}}^{\mathrm{t}}) + \boldsymbol{J}_{\hat{\mathrm{u}}\mathrm{p_d}}(\theta \boldsymbol{p}_{\mathrm{d}_{\mathrm{j}-1}}^{\mathrm{t}+\triangle\mathrm{t}} + (1-\theta)\boldsymbol{p}_{\mathrm{d}}^{\mathrm{t}})\end{aligned}$$

$$\begin{aligned}\boldsymbol{f}_{\tilde{\mathrm{u}}}^{\mathrm{int}} =& \boldsymbol{J}_{\tilde{\mathrm{u}}\hat{\mathrm{u}}}(\theta \hat{\boldsymbol{u}}_{\mathrm{j}-1}^{\mathrm{t}+\triangle\mathrm{t}} + (1-\theta)\hat{\boldsymbol{u}}^{\mathrm{t}}) + \boldsymbol{J}_{\tilde{\mathrm{u}}\tilde{\mathrm{u}}}(\theta \tilde{\boldsymbol{u}}_{\mathrm{j}-1}^{\mathrm{t}+\triangle\mathrm{t}} + (1-\theta)\tilde{\boldsymbol{u}}^{\mathrm{t}}) + \boldsymbol{J}_{\tilde{\mathrm{u}}\hat{\mathrm{p}}}(\theta \hat{\boldsymbol{p}}_{\mathrm{j}-1}^{\mathrm{t}+\triangle\mathrm{t}} + (1-\theta)\hat{\boldsymbol{p}}^{\mathrm{t}}) \\ &+ \boldsymbol{J}_{\tilde{\mathrm{u}}\tilde{\mathrm{p}}}(\theta \tilde{\boldsymbol{p}}_{\mathrm{j}-1}^{\mathrm{t}+\triangle\mathrm{t}} + (1-\theta)\tilde{\boldsymbol{p}}^{\mathrm{t}}) + \boldsymbol{J}_{\tilde{\mathrm{u}}\mathrm{p_d}}(\theta \boldsymbol{p}_{\mathrm{d}_{\mathrm{j}-1}}^{\mathrm{t}+\triangle\mathrm{t}} + (1-\theta)\boldsymbol{p}_{\mathrm{d}}^{\mathrm{t}})\end{aligned}$$

$$\begin{aligned}\boldsymbol{f}_{\hat{\mathrm{p}}}^{\mathrm{int}} =& \boldsymbol{J}_{\hat{\mathrm{p}}\hat{\mathrm{u}}}(\hat{\boldsymbol{u}}_{\mathrm{j}-1}^{\mathrm{t}+\triangle\mathrm{t}} - \hat{\boldsymbol{u}}^{\mathrm{t}}) + \boldsymbol{J}_{\hat{\mathrm{p}}\tilde{\mathrm{u}}}(\tilde{\boldsymbol{u}}_{\mathrm{j}-1}^{\mathrm{t}+\triangle\mathrm{t}} - \tilde{\boldsymbol{u}}^{\mathrm{t}}) + (\boldsymbol{J}_{\hat{\mathrm{p}}\hat{\mathrm{p}}}^{(1)} + \boldsymbol{J}_{\hat{\mathrm{p}}\hat{\mathrm{p}}}^{(3)})\triangle t(\theta \hat{\boldsymbol{p}}_{\mathrm{j}-1}^{\mathrm{t}+\triangle\mathrm{t}} + (1-\theta)\hat{\boldsymbol{p}}^{\mathrm{t}}) \\ &+ \boldsymbol{J}_{\hat{\mathrm{p}}\hat{\mathrm{p}}}^{(2)}(\hat{\boldsymbol{p}}_{\mathrm{j}-1}^{\mathrm{t}+\triangle\mathrm{t}} - \hat{\boldsymbol{p}}^{\mathrm{t}}) + (\boldsymbol{J}_{\hat{\mathrm{p}}\tilde{\mathrm{p}}}^{(1)} + \boldsymbol{J}_{\hat{\mathrm{p}}\tilde{\mathrm{p}}}^{(3)})(\theta \tilde{\boldsymbol{p}}_{\mathrm{j}-1}^{\mathrm{t}+\triangle\mathrm{t}} + (1-\theta)\tilde{\boldsymbol{p}}^{\mathrm{t}})\triangle t + \boldsymbol{J}_{\hat{\mathrm{p}}\tilde{\mathrm{p}}}^{(2)}(\tilde{\boldsymbol{p}}_{\mathrm{j}-1}^{\mathrm{t}+\triangle\mathrm{t}} - \tilde{\boldsymbol{p}}^{\mathrm{t}}) \\ &+ \boldsymbol{J}_{\hat{\mathrm{p}}\mathrm{p_d}}(\theta \boldsymbol{p}_{\mathrm{d}_{\mathrm{j}-1}}^{\mathrm{t}+\triangle\mathrm{t}} + (1-\theta)\boldsymbol{p}_{\mathrm{d}}^{\mathrm{t}})\triangle t\end{aligned}$$

$$\begin{aligned}\boldsymbol{f}_{\tilde{\mathrm{p}}}^{\mathrm{int}} =& \boldsymbol{J}_{\tilde{\mathrm{p}}\hat{\mathrm{u}}}(\hat{\boldsymbol{u}}_{\mathrm{j}-1}^{\mathrm{t}+\triangle\mathrm{t}} - \hat{\boldsymbol{u}}^{\mathrm{t}}) + \boldsymbol{J}_{\tilde{\mathrm{p}}\tilde{\mathrm{u}}}(\tilde{\boldsymbol{u}}_{\mathrm{j}-1}^{\mathrm{t}+\triangle\mathrm{t}} - \tilde{\boldsymbol{u}}^{\mathrm{t}}) + (\boldsymbol{J}_{\tilde{\mathrm{p}}\hat{\mathrm{p}}}^{(1)} + \boldsymbol{J}_{\tilde{\mathrm{p}}\hat{\mathrm{p}}}^{(3)})\triangle t(\theta \hat{\boldsymbol{p}}_{\mathrm{j}-1}^{\mathrm{t}+\triangle\mathrm{t}} + (1-\theta)\hat{\boldsymbol{p}}^{\mathrm{t}}) \\ &+ \boldsymbol{J}_{\tilde{\mathrm{p}}\hat{\mathrm{p}}}^{(2)}(\hat{\boldsymbol{p}}_{\mathrm{j}-1}^{\mathrm{t}+\triangle\mathrm{t}} - \hat{\boldsymbol{p}}^{\mathrm{t}}) + (\boldsymbol{J}_{\tilde{\mathrm{p}}\tilde{\mathrm{p}}}^{(1)} + \boldsymbol{J}_{\tilde{\mathrm{p}}\tilde{\mathrm{p}}}^{(3)})(\theta \tilde{\boldsymbol{p}}_{\mathrm{j}-1}^{\mathrm{t}+\triangle\mathrm{t}} + (1-\theta)\tilde{\boldsymbol{p}}^{\mathrm{t}})\triangle t + \boldsymbol{J}_{\tilde{\mathrm{p}}\tilde{\mathrm{p}}}^{(2)}(\tilde{\boldsymbol{p}}_{\mathrm{j}-1}^{\mathrm{t}+\triangle\mathrm{t}} - \tilde{\boldsymbol{p}}^{\mathrm{t}}) \\ &+ \boldsymbol{J}_{\tilde{\mathrm{p}}\mathrm{p_d}}(\theta \boldsymbol{p}_{\mathrm{d}_{\mathrm{j}-1}}^{\mathrm{t}+\triangle\mathrm{t}} + (1-\theta)\boldsymbol{p}_{\mathrm{d}}^{\mathrm{t}})\triangle t\end{aligned}$$

$$\begin{aligned}\boldsymbol{f}_{\mathrm{p_d}}^{\mathrm{int}} =& \boldsymbol{J}_{\mathrm{p_d}\hat{\mathrm{u}}}(\hat{\boldsymbol{u}}_{\mathrm{j}-1}^{\mathrm{t}+\triangle\mathrm{t}} - \hat{\boldsymbol{u}}^{\mathrm{t}}) + (\boldsymbol{J}_{\mathrm{p_d}\tilde{\mathrm{u}}}^{(1)} + \boldsymbol{J}_{\mathrm{p_d}\tilde{\mathrm{u}}}^{(3)} + \boldsymbol{J}_{\mathrm{p_d}\tilde{\mathrm{u}}}^{(4)})(\tilde{\boldsymbol{u}}_{\mathrm{j}-1}^{\mathrm{t}+\triangle\mathrm{t}} - \tilde{\boldsymbol{u}}^{\mathrm{t}}) + \boldsymbol{J}_{\mathrm{p_d}\hat{\mathrm{p}}}(\theta \hat{\boldsymbol{p}}_{\mathrm{j}-1}^{\mathrm{t}+\triangle\mathrm{t}} + (1-\theta)\hat{\boldsymbol{p}}^{\mathrm{t}})\triangle t \\ &+ ((\boldsymbol{J}_{\mathrm{p_d}\tilde{\mathrm{u}}}^{(5)} + \boldsymbol{J}_{\mathrm{p_d}\tilde{\mathrm{u}}}^{(6)})\triangle t + \boldsymbol{J}_{\mathrm{p_d}\tilde{\mathrm{u}}}^{(7)} + \boldsymbol{J}_{\mathrm{p_d}\tilde{\mathrm{u}}}^{(2)})(\theta \tilde{\boldsymbol{u}}_{\mathrm{j}-1}^{\mathrm{t}+\triangle\mathrm{t}} + (1-\theta)\tilde{\boldsymbol{u}}^{\mathrm{t}}) + \boldsymbol{J}_{\mathrm{p_d}\tilde{\mathrm{p}}}(\theta \tilde{\boldsymbol{p}}_{\mathrm{j}-1}^{\mathrm{t}+\triangle\mathrm{t}} + (1-\theta)\tilde{\boldsymbol{p}}^{\mathrm{t}})\triangle t \\ &+ (\boldsymbol{J}_{\mathrm{p_d}\mathrm{p_d}}^{(1)} + \boldsymbol{J}_{\mathrm{p_d}\mathrm{p_d}}^{(3)} + \boldsymbol{J}_{\mathrm{p_d}\mathrm{p_d}}^{(4)})(\theta \boldsymbol{p}_{\mathrm{d}_{\mathrm{j}-1}}^{\mathrm{t}+\triangle\mathrm{t}} + (1-\theta)\boldsymbol{p}_{\mathrm{d}}^{\mathrm{t}})\triangle t + \boldsymbol{J}_{\mathrm{p_d}\mathrm{p_d}}^{(2)}(\boldsymbol{p}_{\mathrm{d}_{\mathrm{j}-1}}^{\mathrm{t}+\triangle\mathrm{t}} - \boldsymbol{p}_{\mathrm{d}}^{\mathrm{t}})\end{aligned}$$

Appendix B

Final fracture orientation angles for varying anisotropy ratios

In this appendix we provide the final fracture orientation angle with respect to the horizontal (x-axis) due to various anisotropies, which was used in the contour plots.

Table B.1: Degree of material anisotropy Vs Degree of stress anisotropy (for Grain orientation:0°).

		Material DOA (in %)															
		0	5	10	15	20	25	30	35	40	45	50	55	60	65	70	75
Stress DOA (in %)	0	90	90	90	90	90	90	90	90	90	90	11	13	13	11	10	10
	5	90	90	90	90	90	90	90	90	90	90	17	18	17	17	17	13
	10	90	90	90	90	90	90	90	90	90	90	90	26	26	22	21	21
	15	90	90	90	90	90	90	90	90	90	90	90	90	31	31	32	31
	20	90	90	90	90	90	90	90	90	90	90	90	90	88	88	88	88
	25	90	90	90	90	90	90	90	90	90	90	90	90	90	89	88	87
	30	90	90	90	90	90	90	90	90	90	90	90	90	90	90	89	89
	35	90	90	90	90	90	90	90	90	90	90	90	90	90	90	90	89
	40	90	90	90	90	90	90	90	90	90	90	90	90	90	90	90	89
	45	90	90	90	90	90	90	90	90	90	90	90	90	90	90	90	89
	50	90	90	90	90	90	90	90	90	90	90	90	90	90	90	89	89

Table B.2: Degree of material anisotropy Vs Degree of stress anisotropy (for Grain orientation:30°).

		Material DOA (in %)															
		0	5	10	15	20	25	30	35	40	45	50	55	60	65	70	75
Stress DOA (in %)	0	90	115	115	37	37	36	36	35	34	33	33	33	32	32	31	32
	5	90	114	115	115	40	40	40	39	40	39	38	38	37	36	36	34
	10	90	113	113	113	45	45	45	45	45	45	44	45	43	43	42	44
	15	90	111	112	112	112	48	49	49	49	49	51	52	51	51	52	50
	20	90	111	111	111	111	111	54	54	56	55	56	56	57	58	58	62
	25	90	109	110	110	110	110	110	109	109	109	109	57	62	63	63	64
	30	90	109	109	109	109	109	109	109	109	109	109	109	60	64	65	66
	35	90	108	108	108	108	108	109	109	109	109	108	108	108	66	68	68
	40	90	108	108	108	108	108	108	108	108	108	108	108	108	80	88	88
	45	90	107	107	107	107	107	97	97	97	97	107	107	107	101	84	83
	50	90	107	106	107	97	97	97	97	97	97	107	107	99	99	82	83

Table B.3: Degree of material anisotropy Vs Degree of stress anisotropy (for Grain orientation:60°).

		Material DOA (in %)															
		0	5	10	15	20	25	30	35	40	45	50	55	60	65	70	75
Stress DOA (in %)	0	90	65	65	65	65	65	65	66	66	66	66	67	67	67	67	69
	5	90	66	66	67	66	67	67	67	67	67	68	68	68	68	69	69
	10	90	67	68	68	68	68	68	68	68	69	69	69	69	70	72	72
	15	90	70	69	69	69	69	69	69	70	70	70	70	70	72	72	77
	20	90	69	69	70	70	70	71	71	71	72	71	72	74	74	74	74
	25	90	70	71	71	72	71	71	72	72	72	73	74	74	74	77	75
	30	90	71	71	72	72	72	72	73	73	74	74	74	74	74	75	76
	35	90	72	72	72	72	73	74	74	74	74	72	72	75	75	76	77
	40	90	72	73	73	73	74	74	74	74	75	75	75	76	76	76	77
	45	90	73	73	73	74	74	74	75	75	75	76	76	76	77	77	77
	50	90	73	74	74	74	74	74	74	75	76	76	76	77	77	77	77

Table B.4: Degree of Young's modulus anisotropy Vs Degree of ultimate tensile strength anisotropy (for Grain orientation:0°).

		Young's modulus DOA (in %)															
		0	5	10	15	20	25	30	35	40	45	50	55	60	65	70	75
Ultimate tensile strength DOA (in %)	0	90	90	90	90	90	90	90	90	90	90	90	89	89	89	89	89
	5	90	90	90	90	90	90	90	90	90	90	90	89	89	89	89	89
	10	90	90	90	90	90	90	90	90	90	90	90	89	89	89	89	89
	15	90	90	90	90	90	90	90	90	90	90	90	89	89	89	89	89
	20	90	90	90	90	90	90	90	90	90	90	90	89	89	89	89	89
	25	90	90	90	90	90	90	90	90	90	90	90	90	90	89	89	89
	30	90	90	90	90	90	90	90	90	90	90	90	90	90	90	89	89
	35	90	90	90	90	90	90	90	90	90	90	90	90	90	90	90	89
	40	90	90	90	90	90	90	90	90	90	90	90	90	90	90	90	89
	45	90	90	90	90	90	90	90	90	90	90	90	90	11	11	11	89
	50	16	12	12	12	15	15	15	15	15	11	11	11	11	11	11	11
	55	15	12	15	15	15	15	15	15	12	12	12	13	11	11	13	13
	60	13	12	12	12	12	12	12	12	12	12	12	12	13	12	11	12
	65	13	12	12	12	12	12	13	12	12	12	11	11	11	11	12	12
	70	13	11	12	12	12	12	13	12	12	11	11	11	11	12	10	10
	75	12	12	12	12	12	12	12	12	12	12	12	13	10	11	11	10

Table B.5: Degree of Young's modulus anisotropy Vs Degree of ultimate tensile strength anisotropy (for Grain orientation:30°).

		Young's Modulus DOA (in %)															
		0	5	10	15	20	25	30	35	40	45	50	55	60	65	70	75
Ultimate tensile strength DOA (in %)	0	90	115	115	116	118	118	119	119	120	120	121	122	123	123	126	127
	5	90	115	115	116	118	118	119	119	120	120	121	122	123	123	126	127
	10	90	115	115	116	116	118	119	119	120	120	121	122	123	123	125	127
	15	38	37	37	37	36	36	118	119	120	120	121	122	122	123	125	127
	20	38	37	37	37	37	36	35	34	34	120	37	121	122	123	125	127
	25	38	37	37	37	37	36	35	34	34	33	33	33	122	123	125	127
	30	38	38	37	37	37	36	36	35	34	33	33	33	122	123	125	126
	35	39	38	37	37	37	36	36	35	34	34	33	33	33	123	124	125
	40	39	38	37	37	37	36	36	35	34	33	33	33	33	33	123	125
	45	39	38	37	36	37	36	36	35	34	33	33	33	33	33	123	124
	50	39	38	37	37	37	36	36	35	34	34	33	33	33	33	122	123
	55	39	38	37	37	37	36	36	34	34	34	33	33	33	32	32	31
	60	39	38	37	37	37	36	36	35	35	34	33	33	32	32	31	31
	65	39	38	37	37	37	36	35	36	34	34	33	33	33	32	32	31
	70	39	39	38	37	37	36	35	36	35	34	34	33	32	33	31	31
	75	38	38	37	37	36	36	36	35	35	34	34	33	33	33	31	32

Table B.6: Degree of Young's modulus anisotropy Vs Degree of ultimate tensile strength anisotropy (for Grain orientation:60°).

		Young's Modulus DOA (in %)															
		0	5	10	15	20	25	30	35	40	45	50	55	60	65	70	75
Ultimate tensile strength DOA (in %)	0	90	90	90	90	90	90	90	90	90	90	147	147	149	149	149	149
	5	65	65	65	65	65	65	65	65	65	65	66	66	149	149	150	150
	10	65	65	65	65	65	65	65	65	65	65	66	66	66	68	68	68
	15	65	65	65	65	65	65	65	65	65	66	66	67	67	68	68	68
	20	65	65	65	65	65	65	65	65	66	66	66	67	67	67	68	68
	25	65	66	65	65	65	65	65	65	66	65	66	67	68	68	68	73
	30	66	66	66	66	65	65	65	66	65	65	65	66	66	67	68	76
	35	66	65	65	65	65	65	65	66	66	65	66	66	66	67	71	71
	40	66	66	66	65	65	65	65	66	66	66	65	67	66	67	68	68
	45	66	66	66	66	66	66	66	66	66	66	65	66	66	67	68	69
	50	65	65	66	66	66	65	66	66	65	65	66	67	66	67	68	69
	55	65	66	66	66	66	66	65	66	66	66	67	67	66	67	68	69
	60	66	66	66	66	65	66	65	65	66	66	67	66	67	66	68	69
	65	66	66	66	66	66	65	66	66	66	66	68	66	68	67	67	69
	70	66	66	66	66	66	65	66	66	67	68	67	67	68	71	67	69
	75	67	66	67	66	66	66	67	66	68	67	66	67	67	73	73	69

Table B.7: Degree of material anisotropy Vs Grain orientation.

		Material DOA (in %)															
		0	5	10	15	20	25	30	35	40	45	50	55	60	65	70	75
Grain orientation	0	90	90	90	90	90	90	90	90	90	90	11	13	13	11	10	10
	10	90	99	99	99	99	99	99	20	20	20	20	16	17	18	17	17
	20	90	107	107	107	23	26	26	26	26	26	26	26	26	25	25	23
	30	90	115	115	37	37	36	36	35	34	33	33	33	32	32	31	32
	40	90	46	46	45	45	45	44	44	43	44	43	42	42	42	42	45
	50	90	55	55	55	56	56	55	55	54	54	55	56	56	56	56	58
	60	90	65	65	65	65	65	65	66	66	66	66	67	67	67	67	69
	70	90	74	73	73	73	74	74	74	74	74	74	75	77	77	77	81
	80	90	82	82	82	82	83	83	83	83	83	84	84	84	85	85	86
	90	90	90	90	90	90	90	90	90	90	90	90	90	90	90	90	90

Bibliography

Y. Abousleiman, A.-D. Cheng, L. Cui, E. Detournay, and J.-C. Roegiers. Mandel's problem revisited. *Geotechnique*, 46(2):187–195, 1996. (Cited on pages 48 and 56.)

Y. N. Abousleiman, M. H. Tran, S. Hoang, et al. Laboratory characterization of anisotropy and fluid effects on shale mechanical properties using inclined direct shear testing device idstd. In *The 42nd US Rock Mechanics Symposium (USRMS)*. American Rock Mechanics Association, 2008. (Cited on page 48.)

J. Adachi and E. Detournay. Plane strain propagation of a hydraulic fracture in a permeable rock. *Engineering Fracture Mechanics*, 75(16):4666–4694, 2008. (Cited on pages 10 and 24.)

A. Afrouz. *Practical handbook of rock mass classification systems and modes of ground failure*. CRC Press, 1992. (Cited on page 80.)

A. Al-Busaidi, J. Hazzard, and R. Young. Distinct element modeling of hydraulically fractured lac du bonnet granite. *Journal of geophysical research: solid earth*, 110(B6), 2005. (Cited on page 10.)

X. Bao and D. W. Eaton. Fault activation by hydraulic fracturing in western canada. *Science*, 354(6318):1406–1409, 2016. (Cited on page 6.)

G. I. Barenblatt. The mathematical theory of equilibrium cracks in brittle fracture. In *Advances in applied mechanics*, volume 7, pages 55–129. Elsevier, 1962. (Cited on pages 10, 28, 76, and 101.)

N. Barton. *Rock quality, seismic velocity, attenuation and anisotropy*. CRC press, 2007. (Cited on page 48.)

S. Bhattacharya, P. Ghosh, and A. Chakrabarti. Isotopic analysis of permo-carboniferous talchir sediments from east-central india: signature of glacial

melt-water lakes. *Chemical Geology*, 188(3-4):261–274, 2002. (Cited on page 92.)

M. A. Biot. General theory of three-dimensional consolidation. *Journal of applied physics*, 12(2):155–164, 1941. (Cited on pages 49 and 75.)

H. Blatt, G. V. Middleton, and R. C. Murray. Origin of sedimentary rocks. 1972. (Cited on page 74.)

Q. D. Boersma, L. A. Douma, G. Bertotti, and A. Barnhoorn. Mechanical controls on horizontal stresses and fracture behaviour in layered rocks: A numerical sensitivity analysis. *Journal of Structural Geology*, page 103907, 2019. (Cited on page 90.)

T. J. Boone and A. R. Ingraffea. A numerical procedure for simulation of hydraulically-driven fracture propagation in poroelastic media. *International Journal for Numerical and Analytical Methods in Geomechanics*, 14(1):27–47, 1990. (Cited on pages 10 and 48.)

S. L. Brantley, D. Yoxtheimer, S. Arjmand, P. Grieve, R. Vidic, J. Pollak, G. T. Llewellyn, J. Abad, and C. Simon. Water resource impacts during unconventional shale gas development: The pennsylvania experience. *International Journal of Coal Geology*, 126:140–156, 2014. (Cited on page 74.)

S. L. Brenner and A. Gudmundsson. Arrest and aperture variation of hydrofractures in layered reservoirs. *Geological Society, London, Special Publications*, 231(1):117–128, 2004. (Cited on page 90.)

D. W. Brown, D. V. Duchane, G. Heiken, and V. T. Hriscu. *Mining the earth's heat: hot dry rock geothermal energy*. Springer Science & Business Media, 2012. (Cited on page 4.)

A. P. Bunger, E. Detournay, and D. I. Garagash. Toughness-dominated hydraulic fracture with leak-off. *International journal of fracture*, 134(2):175–190, 2005. (Cited on pages 24 and 60.)

S. Burden, M. Fleming, J. Frithsen, L. Hills, K. Klewicki, C. Knightes, et al. Hydraulic fracturing for oil and gas: Impacts from the hydraulic fracturing water cycle on drinking water resources in the united states. *Washington, DC: US EPA*, 2016. (Cited on page 6.)

G. T. Camacho and M. Ortiz. Computational modelling of impact damage in brittle materials. *International Journal of solids and structures*, 33(20-22): 2899–2938, 1996. (Cited on pages 52 and 77.)

B. Carrier and S. Granet. Numerical modeling of hydraulic fracture problem in permeable medium using cohesive zone model. *Engineering fracture mechanics*, 79:312–328, 2012. (Cited on pages 10, 24, and 48.)

H. Carslaw and J. Jaeger. *Conduction of heat in solids: Oxford Science Publications*. Oxford, England, 1959. (Cited on page 37.)

M. Centeno Lobão, R. Eve, D. Owen, and E. A. de Souza Neto. Modelling of hydro-fracture flow in porous media. *Engineering Computations*, 27(1): 129–154, 2010. (Cited on page 10.)

Z. Chen. Finite element modelling of viscosity-dominated hydraulic fractures. *Journal of Petroleum Science and Engineering*, 88:136–144, 2012. (Cited on page 48.)

Z. Chen, A. Bunger, X. Zhang, and R. G. Jeffrey. Cohesive zone finite element-based modeling of hydraulic fractures. *Acta Mechanica Solida Sinica*, 22(5): 443–452, 2009. (Cited on page 10.)

A. H.-D. Cheng. Material coefficients of anisotropic poroelasticity. *International Journal of Rock Mechanics and Mining Sciences*, 34(2):199–205, 1997. (Cited on pages 48 and 55.)

D. A. Chuprakov, R. Prioul, et al. Hydraulic fracture height containment by weak horizontal interfaces. In *SPE Hydraulic Fracturing Technology Conference*. Society of Petroleum Engineers, 2015. (Cited on page 75.)

A. Daneshy et al. Hydraulic fracture propagation in layered formations. *Society of Petroleum Engineers Journal*, 18(01):33–41, 1978. (Cited on page 74.)

Department of mines, industry regulation and safety, Government of Western Australia. Hydraulic fracture stimulation. `https://www.dmp.wa.gov.au/Petroleum/Hydraulic-fracture-stimulation-20018.aspx`, 2018. Online; accessed 20-August-2019. (Cited on page 3.)

E. Detournay. Propagation regimes of fluid-driven fractures in impermeable rocks. *International Journal of Geomechanics*, 4(1):35–45, 2004. (Cited on page 10.)

E. Detournay and A. H.-D. Cheng. Fundamentals of poroelasticity. *Comprehensive rock engineering: principles, practice and projects*, 2:113–171, 1993. (Cited on pages 29 and 31.)

E. Dontsov. An approximate solution for a plane strain hydraulic fracture that accounts for fracture toughness, fluid viscosity, and leak-off. *International Journal of Fracture*, 205(2):221–237, 2017. (Cited on page 10.)

E. Dontsov and A. Peirce. A multiscale implicit level set algorithm (ilsa) to model hydraulic fracture propagation incorporating combined viscous, toughness, and leak-off asymptotics. *Computer Methods in Applied Mechanics and Engineering*, 313:53–84, 2017. (Cited on page 101.)

L. Druyff. Reservoir properties of the bakken shale. 1990. (Cited on page 101.)

D. S. Dugdale. Yielding of steel sheets containing slits. *Journal of the Mechanics and Physics of Solids*, 8(2):100–104, 1960. (Cited on page 10.)

M. Economides and K. Nolte. *Reservoir Stimulation*. Wiley, 2000. ISBN 9780471491927. (Cited on pages 4 and 74.)

Y. Fan, M. J. Economides, et al. Fracturing fluid leakoff and net pressure behavior in frac & pack stimulation. In *International Meeting on Petroleum Engineering*. Society of Petroleum Engineers, 1995. (Cited on pages 24 and 46.)

M. K. Fisher, N. R. Warpinski, et al. Hydraulic fracture-height growth: real data. In *SPE Annual Technical Conference and Exhibition*. Society of Petroleum Engineers, 2011. (Cited on page 74.)

M. K. Fisher, N. R. Warpinski, et al. Hydraulic-fracture-height growth: Real data. *SPE Production & Operations*, 27(01):8–19, 2012. (Cited on page 4.)

S. A. Flewelling, M. P. Tymchak, and N. Warpinski. Hydraulic fracture height limits and fault interactions in tight oil and gas formations. *Geophysical Research Letters*, 40(14):3602–3606, 2013. (Cited on page 74.)

D. Garagash and E. Detournay. The tip region of a fluid-driven fracture in an elastic medium. *Journal of applied mechanics*, 67(1):183–192, 2000. (Cited on page 10.)

X. Garcia, N. Nagel, F. Zhang, M. Sanchez-Nagel, B. Lee, et al. Revisiting vertical hydraulic fracture propagation through layered formations–a numerical evaluation. In *47th US Rock Mechanics/Geomechanics Symposium*. American Rock Mechanics Association, 2013. (Cited on page 75.)

J. Geertsma and F. De Klerk. A rapid method of predicting width and extent of hydraulically induced fractures. *Journal of Petroleum Technology*, 21(12): 1571–1581, 1969. (Cited on pages 10, 11, and 58.)

Geology.com. `https://geology.com/rocks/`, 2018. Online; accessed 20-August-2019. (Cited on page 5.)

E. Gordeliy and A. Peirce. Coupling schemes for modeling hydraulic fracture propagation using the xfem. *Computer Methods in Applied Mechanics and Engineering*, 253:305–322, 2013a. (Cited on page 48.)

E. Gordeliy and A. Peirce. Implicit level set schemes for modeling hydraulic fractures using the xfem. *Computer Methods in Applied Mechanics and Engineering*, 266:125–143, 2013b. (Cited on page 48.)

E. Gordeliy and A. Peirce. Enrichment strategies and convergence properties of the xfem for hydraulic fracture problems. *Computer Methods in Applied Mechanics and Engineering*, 283:474–502, 2015. (Cited on page 48.)

H. Gu, E. Siebrits, et al. Effect of formation modulus contrast on hydraulic fracture height containment. In *International Oil & Gas Conference and Exhibition in China*. Society of Petroleum Engineers, 2006. (Cited on pages 75, 80, and 89.)

P. Gupta and C. A. Duarte. Coupled formulation and algorithms for the simulation of non-planar three-dimensional hydraulic fractures using the generalized finite element method. *International Journal for Numerical and Analytical Methods in Geomechanics*, 40(10):1402–1437, 2016. (Cited on page 101.)

A. Hatheway and G. Kiersch. Engineering properties of rock. *Practical Handbook of Physical Properties of Rocks and Minerals*, pages 672–715, 1989. (Cited on page 80.)

Y. Heider and B. Markert. A phase-field modeling approach of hydraulic fracture in saturated porous media. *Mechanics Research Communications*, 80: 38–46, 2017. (Cited on page 10.)

M. M. Hossain and M. Rahman. Numerical simulation of complex fracture growth during tight reservoir stimulation by hydraulic fracturing. *Journal of Petroleum Science and Engineering*, 60(2):86–104, 2008. (Cited on page 48.)

G. C. Howard and C. Fast. Optimum fluid characteristics for fracture extension. In *Drilling and production practice*. American Petroleum Institute, 1957. (Cited on page 24.)

M. K. Hubbert and D. G. Willis. Mechanics of hydraulic fracturing. *AAPG Special Volumes*, pages 239–257, 1972. (Cited on page 4.)

International Energy Agency. Global Energy and CO2 Status Report. `https://www.iea.org/geco/emissions/`, 2018a. Online; accessed 20-August-2019. (Cited on page 2.)

International Energy Agency. World Energy Outlook. `https://www.iea.org/weo/weo2018/secure/`, 2018b. Online; accessed 20-August-2019. (Cited on page 1.)

F. Irzal, J. J. Remmers, J. M. Huyghe, and R. de Borst. A large deformation formulation for fluid flow in a progressively fracturing porous material. *Computer Methods in Applied Mechanics and Engineering*, 256:29–37, 2013. (Cited on pages 31 and 76.)

J. C. Jaeger, N. G. Cook, and R. Zimmerman. *Fundamentals of rock mechanics*. John Wiley & Sons, 2009. (Cited on pages 48 and 83.)

M. Jirasek. Embedded crack models for concrete fracture. In *Computational Modelling of Concrete Structures, EURO C-98*, volume 1, pages 291–300, 1998. (Cited on pages 52 and 77.)

R. M. Jones. *Mechanics of composite materials*. CRC press, 1998. (Cited on page 53.)

A. R. Jumikis. Rock mechanics: Series on rock and soil mechanics (v. 3). *Trans Tech publications, USA*, 1979. (Cited on page 83.)

E. A. Kaarsberg. Introductory studies of natural and artificial argillaceous aggregates by sound-propagation and x-ray diffraction methods. *The Journal of Geology*, pages 447–472, 1959. (Cited on page 48.)

S. Khristianovic and Y. Zheltov. Formation of vertical fractures by means of highly viscous liquid. *Proceedings of the Fourth World Petroleum Congress, Rome*, pages 579—-586, 1955. (Cited on page 11.)

G. E. King et al. Thirty years of gas shale fracturing: What have we learned? In *SPE Annual Technical Conference and Exhibition*. Society of Petroleum Engineers, 2010. (Cited on page 3.)

Y. Kovalyshen. *Fluid-driven fracture in poroelastic medium*. PhD thesis, University of Minnesota, 2010. (Cited on page 10.)

B. Lecampion. An extended finite element method for hydraulic fracture problems. *International Journal for Numerical Methods in Biomedical Engineering*, 25(2):121–133, 2009. (Cited on page 10.)

Y.-K. Lee and S. Pietruszczak. Tensile failure criterion for transversely isotropic rocks. *International Journal of Rock Mechanics and Mining Sciences*, 79:205–215, 2015. (Cited on pages 53 and 54.)

B. Legarth, E. Huenges, and G. Zimmermann. Hydraulic fracturing in a sedimentary geothermal reservoir: Results and implications. *International Journal of Rock Mechanics and Mining Sciences*, 42(7-8):1028–1041, 2005. (Cited on page 4.)

M. W. McClure and R. N. Horne. An investigation of stimulation mechanisms in enhanced geothermal systems. *International Journal of Rock Mechanics and Mining Sciences*, 72:242–260, 2014. (Cited on page 10.)

J. M. Melenk and I. Babuška. The partition of unity finite element method: basic theory and applications. *Computer methods in applied mechanics and engineering*, 139(1-4):289–314, 1996. (Cited on pages 34 and 76.)

G. Meschke and D. Leonhart. A generalized finite element method for hydro-mechanically coupled analysis of hydraulic fracturing problems using space-time variant enrichment functions. *Computer Methods in Applied Mechanics and Engineering*, 290:438–465, 2015. (Cited on pages 11 and 48.)

S. Mighani, C. H. Sondergeld, C. S. Rai, et al. Observations of tensile fracturing of anisotropic rocks. *SPE Journal*, 2016. (Cited on pages 48 and 54.)

A. Mikelic, M. F. Wheeler, and T. Wick. A phase-field method for propagating fluid-filled fractures coupled to a surrounding porous medium. *Multiscale Modeling & Simulation: A SIAM Interdisciplinary Journal, Society for Industrial and Applied Mathematics*, 13(1):367–398, 2015. (Cited on pages 10 and 48.)

A. Mikelić, M. F. Wheeler, and T. Wick. Phase-field modeling of a fluid-driven fracture in a poroelastic medium. *Computational Geosciences*, 19(6):1171–1195, 2015. (Cited on pages 10 and 48.)

A. Mikelić, M. Wheeler, and T. Wick. Phase-field modeling through iterative splitting of hydraulic fractures in a poroelastic medium. *GEM-International Journal on Geomathematics*, 10(1):2, 2019. (Cited on page 10.)

J. L. Miskimins, R. D. Barree, et al. Modeling of hydraulic fracture height containment in laminated sand and shale sequences. In *SPE Production and Operations Symposium*. Society of Petroleum Engineers, 2003. (Cited on page 75.)

N. Moës, A. Gravouil, and T. Belytschko. Non-planar 3d crack growth by the extended finite element and level sets—part i: Mechanical model. *International journal for numerical methods in engineering*, 53(11):2549–2568, 2002. (Cited on page 101.)

T. Mohammadnejad and A. Khoei. An extended finite element method for hydraulic fracture propagation in deformable porous media with the cohesive crack model. *Finite Elements in Analysis and Design*, 73:77–95, 2013. (Cited on pages 10, 24, 46, and 48.)

M. Mokhtari, M. M. M. Honarpour, A. N. Tutuncu, G. N. Boitnott, et al. Acoustical and geomechanical characterization of eagle ford shale-anisotropy, heterogeneity and measurement scale. In *SPE Annual Technical Conference and Exhibition*. Society of Petroleum Engineers, 2014. (Cited on page 89.)

National Renewable Energy Laboratory, U.S. Department of Energy. `https://www.nrel.gov/geothermal/sedimentary-egs.html`, 2018. Online; accessed 20-August-2019. (Cited on page 5.)

A. Needleman. A continuum model for void nucleation by inclusion debonding. *Journal of applied mechanics*, 54(3):525–531, 1987. (Cited on page 28.)

K. G. Nolte, M. B. Smith, et al. Interpretation of fracturing pressures. In *SPE Annual Technical Conference and Exhibition*. Society of Petroleum Engineers, 1979. (Cited on page 74.)

R. Nordgren. Propagation of a vertical hydraulic fracture. *Society of Petroleum Engineers Journal*, 12(04):306–314, 1972. (Cited on page 10.)

S. Oterkus, E. Madenci, and E. Oterkus. Fully coupled poroelastic peridynamic formulation for fluid-filled fractures. *Engineering Geology*, 225:19–28, 2017. (Cited on page 10.)

H. Ouchi, A. Katiyar, J. York, J. T. Foster, and M. M. Sharma. A fully coupled porous flow and geomechanics model for fluid driven cracks: a peridynamics approach. *Computational Mechanics*, 55(3):561–576, 2015. (Cited on page 10.)

H. Ouchi, J. T. Foster, and M. M. Sharma. Effect of reservoir heterogeneity on the vertical migration of hydraulic fractures. *Journal of Petroleum Science and Engineering*, 151:384–408, 2017. (Cited on page 75.)

Q. R. Passey, K. Bohacs, W. L. Esch, R. Klimentidis, S. Sinha, et al. From oil-prone source rock to gas-producing shale reservoir-geologic and petrophysical characterization of unconventional shale gas reservoirs. In *International oil and gas conference and exhibition in China*. Society of Petroleum Engineers, 2010. (Cited on page 89.)

A. Peirce and E. Detournay. An implicit level set method for modeling hydraulically driven fractures. *Computer Methods in Applied Mechanics and Engineering*, 197(33-40):2858–2885, 2008. (Cited on page 10.)

G. S. Penny, M. W. Conway, W. Lee, et al. Control and modeling of fluid leakoff during hydraulic fracturing. *Journal of petroleum technology*, 37(06):1–071, 1985. (Cited on page 6.)

T. Perkins and L. Kern. Widths of hydraulic fractures. *Journal of Petroleum Technology*, 13(09):937–949, 1961. (Cited on page 10.)

Z. Rahim, H. A. Al-anazi, A. Kanaan, A. H. Habbtar, A. M. Omair, N. H. Senturk, D. A. Kalinin, et al. Productivity increase through hydraulic fracturing in conventional and tight gas reservoirs-expectation versus reality. In *SPE Middle East Unconventional Gas Conference and Exhibition*. Society of Petroleum Engineers, 2012. (Cited on page 4.)

E. Remij. *Fluid driven and mechanically induced fracture propagation: theory and numerical simulations*. PhD thesis, Eindhoven University of Technology, Eindhoven, The Netherlands, 2017. (Cited on page 101.)

E. Remij, J. Remmers, J. Huyghe, and D. Smeulders. The enhanced local pressure model for the accurate analysis of fluid pressure driven fracture in porous materials. *Computer Methods in Applied Mechanics and Engineering*, 286:293–312, 2015a. (Cited on pages 10, 11, 24, 26, 31, 40, 46, 48, 49, 51, 56, 59, 76, and 99.)

E. W. Remij, J. J. Remmers, F. Pizzocolo, D. M. Smeulders, and J. M. Huyghe. A partition of unity-based model for crack nucleation and propagation in porous media, including orthotropic materials. *Transport in Porous Media*, 106(3):505–522, 2015b. (Cited on pages 48, 53, and 54.)

J. Remmers, R. d. Borst, and A. Needleman. A cohesive segments method for the simulation of crack growth. *Computational mechanics*, 31(1):69–77, 2003. (Cited on pages 36, 52, and 77.)

J. J. C. Remmers. *Discontinuities in materials and structures—a unifying computational approach*. PhD thesis, Delft University of Technology, Delft, The Netherlands, 2006. (Cited on pages 36, 52, and 77.)

D. J. Rozell and S. J. Reaven. Water pollution risk associated with natural gas extraction from the marcellus shale. *Risk Analysis: An International Journal*, 32(8):1382–1393, 2012. (Cited on page 74.)

C. Sayers. The elastic anisotrophy of shales. *Journal of Geophysical Research: Solid Earth*, 99(B1):767–774, 1994. (Cited on page 48.)

B. A. Schrefler, S. Secchi, and L. Simoni. On adaptive refinement techniques in multi-field problems including cohesive fracture. *Computer methods in applied mechanics and engineering*, 195(4-6):444–461, 2006. (Cited on page 10.)

S. Secchi, L. Simoni, and B. A Schrefler. Mesh adaptation and transfer schemes for discrete fracture propagation in porous materials. *International journal*

for numerical and analytical methods in geomechanics, 31(2):331–345, 2007. (Cited on page 10.)

J. Segura and I. Carol. Coupled hm analysis using zero-thickness interface elements with double nodes—part ii: Verification and application. *International journal for numerical and analytical methods in geomechanics*, 32(18): 2103–2123, 2008a. (Cited on page 10.)

J. M. Segura and I. Carol. Coupled hm analysis using zero-thickness interface elements with double nodes. part i: Theoretical model. *International journal for numerical and analytical methods in geomechanics*, 32(18):2083–2101, 2008b. (Cited on page 10.)

J. Selles-Martinez. Concretion morphology, classification and genesis. *Earth-Science Reviews*, 41(3-4):177–210, 1996. (Cited on page 92.)

J. A. Sethian. A fast marching level set method for monotonically advancing fronts. *Proceedings of the National Academy of Sciences*, 93(4):1591–1595, 1996. (Cited on page 101.)

A. Settari et al. A new general model of fluid loss in hydraulic fracturing. *Society of Petroleum Engineers Journal*, 25(04):491–501, 1985. (Cited on page 24.)

E. Simonson, A. Abou-Sayed, R. Clifton, et al. Containment of massive hydraulic fractures. *Society of Petroleum Engineers Journal*, 18(01):27–32, 1978. (Cited on pages 4, 74, and 79.)

M. Smith, A. Bale, L. Britt, H. Klein, E. Siebrits, and X. Dang. Layered modulus effects on fracture propagation, proppant placement, and fracture modeling. paper spe 71654 presented at the spe annual technical conference and exhibition, new orleans, 30 september–3 october, 2001. (Cited on pages 75 and 80.)

B. Sobhaniaragh, W. Mansur, and F. Peters. On the stress-shadow effects of multiple-stage hydraulic fracturing in unconventional reservoirs by using cohesive phantom node method. In *SEG Technical Program Expanded Abstracts 2016*, pages 3422–3427. Society of Exploration Geophysicists, 2016. (Cited on page 43.)

H. Sone and M. D. Zoback. Mechanical properties of shale-gas reservoir rocks—part 1: Static and dynamic elastic properties and anisotropy. *Geophysics*, 78(5):D381–D392, 2013. (Cited on page 101.)

N. Sukumar, D. L. Chopp, and B. Moran. Extended finite element method and fast marching method for three-dimensional fatigue crack propagation. *Engineering Fracture Mechanics*, 70(1):29–48, 2003. (Cited on page 101.)

R. Taherdangkoo, A. Tatomir, R. Taylor, and M. Sauter. Numerical investigations of upward migration of fracking fluid along a fault zone during and after stimulation. *Energy Procedia*, 125:126–135, 2017. (Cited on page 4.)

K. Terzaghi. *Erdbaumechanik and bodenphysikalischer grundlage*. Lpz. Deuticke, 1925. (Cited on pages 24, 29, 37, 49, and 76.)

L. W. Teufel and N. R. Warpinski. An assessment of the factors affecting hydraulic fracture containment in layered rock: Observations from a mineback experiment. In *Hydraulic fracturing and geothermal energy*, pages 251–265. Springer, 1983. (Cited on page 74.)

U.S. Energy Information Administration. International Energy Outlook. `https://www.eia.gov/todayinenergy/detail.php?id=32912`, 2017. Online; accessed 20-August-2019. (Cited on page 1.)

P. Valkó, M. Economides, et al. Fluid leakoff delineation in high-permeability fracturing. In *SPE Production Operations Symposium*. Society of Petroleum Engineers, 1997. (Cited on page 24.)

V. Valliappan, J. Remmers, A. Barnhoorn, and D. Smeulders. A numerical study on the effect of anisotropy on hydraulic fractures. *Rock Mechanics and Rock Engineering*, pages 1–19, 2017. (Cited on page 78.)

C. J. Van Duijn, A. Mikelić, and T. Wick. A monolithic phase-field model of a fluid-driven fracture in a nonlinear poroelastic medium. *Mathematics and Mechanics of Solids*, 24(5):1530–1555, 2019. (Cited on page 10.)

P. J. van Oosterhout. The influence of mechanical contrast on industrial and natural hydraulic fracturing. Master's thesis, Delft University of Technology, Delft, The Netherlands, 2019. (Cited on page 91.)

P. Vermeer and A. Verruijt. An accuracy condition for consolidation by finite elements. *International Journal for numerical and analytical methods in geomechanics*, 5(1):1–14, 1981. (Cited on pages 38 and 46.)

J. P. Vermylen. *Geomechanical studies of the Barnett shale, Texas, USA*. Stanford University, 2011. (Cited on page 101.)

H. Wanas. Calcite-cemented concretions in shallow marine and fluvial sandstones of the birket qarun formation (late eocene), el-faiyum depression, egypt: field, petrographic and geochemical studies: implications for formation conditions. *Sedimentary Geology*, 212(1-4):40–48, 2008. (Cited on page 92.)

N. R. Warner, R. B. Jackson, T. H. Darrah, S. G. Osborn, A. Down, K. Zhao, A. White, and A. Vengosh. Geochemical evidence for possible natural migration of marcellus formation brine to shallow aquifers in pennsylvania. *Proceedings of the National Academy of Sciences*, 109(30):11961–11966, 2012. (Cited on page 74.)

N. R. Warpinski, J. A. Clark, R. A. Schmidt, and C. W. Huddle. Laboratory investigation on the effect of in situ stresses on hydraulic fracture containment. Technical report, Sandia National Labs., Albuquerque, NM (USA), 1981. (Cited on page 74.)

N. R. Warpinski, R. A. Schmidt, D. A. Northrop, et al. In-situ stresses: the predominant influence on hydraulic fracture containment. *Journal of Petroleum Technology*, 34(03):653–664, 1982. (Cited on page 74.)

G. N. Wells and L. Sluys. A new method for modelling cohesive cracks using finite elements. *International Journal for Numerical Methods in Engineering*, 50(12):2667–2682, 2001. (Cited on pages 36 and 77.)

Z. A. Wilson and C. M. Landis. Phase-field modeling of hydraulic fracture. *Journal of the Mechanics and Physics of Solids*, 96:264–290, 2016. (Cited on page 10.)

P. A. Witherspoon, J. S. Wang, K. Iwai, and J. E. Gale. Validity of cubic law for fluid flow in a deformable rock fracture. *Water resources research*, 16(6): 1016–1024, 1980. (Cited on page 28.)

World Energy Council. Unconventional gas, a global phenomenon. `https://www.worldenergy.org/assets/downloads/World-map-Unconventional-gas-a-global-phenomenon-World-Energy-Resources.jpg`, 2016. Online; accessed 20-August-2019. (Cited on page 2.)

K. Wu, J. E. Olson, et al. Simultaneous multifracture treatments: fully coupled fluid flow and fracture mechanics for horizontal wells. *SPE journal*, 20(02): 337–346, 2015. (Cited on page 10.)

P. Xing, A. Bunger, K. Yoshioka, J. Adachi, A. El-Fayoumi, et al. Experimental study of hydraulic fracture containment in layered reservoirs. In *50th US Rock Mechanics/Geomechanics Symposium*. American Rock Mechanics Association, 2016. (Cited on page 74.)

Y. Yang, H. Jiang, M. Li, S. Yang, and G. Chen. A mathematical model of fracturing fluid leak-off based on dynamic discrete grid system. *Journal of Petroleum Exploration and Production Technology*, 6(3):343–349, 2016. (Cited on pages 24 and 46.)

T. Yi, J. Peden, et al. A comprehensive model of fluid loss in hydraulic fracturing. *SPE Production & Facilities*, 9(04):267–272, 1994. (Cited on page 24.)

C. Yu, A. Pandolfi, M. Ortiz, D. Coker, and A. Rosakis. Three-dimensional modeling of intersonic shear-crack growth in asymmetrically loaded unidirectional composite plates. *International Journal of Solids and Structures*, 39 (25):6135–6157, 2002. (Cited on page 53.)

Q. Zhao, A. Lisjak, O. Mahabadi, Q. Liu, and G. Grasselli. Numerical simulation of hydraulic fracturing and associated microseismicity using finite-discrete element method. *Journal of Rock Mechanics and Geotechnical Engineering*, 6 (6):574–581, 2014. (Cited on page 10.)

A. Zhubayev, M. E. Houben, D. M. Smeulders, and A. Barnhoorn. Ultrasonic velocity and attenuation anisotropy of shales, whitby, united kingdom. *Geophysics*, 81(1):D45–D56, 2015. (Cited on page 48.)

Acknowledgements

I would like to take this opportunity to thank all the people who have contributed towards this dissertation and also people who helped me create memories during my stay in the Netherlands.

First of all, I would like to thank my supervisors David, Joris, Auke for giving me this wonderful opportunity to pursue my PhD under their guidance. I am particularly grateful to them for the degree of freedom to conduct research with very little restrictions. Auke with his enthusiasm was a real source of inspiration during the hard times. His excellent insights and constructive comments really helped in shaping up my thesis. I would like to thank Joris for his support and guidance to work with the very elegant 'DAWN' software package and David for facilitating all the connections/collaborations, navigating through the procedures. I would also take this opportunity to thank the committee members for taking their time in reading the thesis and sharing their feedback.

I would like to thank (former) Foundation for Fundamental Research on Matter (FOM), (now) a part of the Netherlands Organization for Scientific Research (NWO), for co-financing this PhD project, together with Shell Global Solutions International B.V. I would also like to thank Shell India Markets Pvt Ltd for facilitating regular interactions with the team in Bengaluru, thereby providing a viable career option after the PhD. I am also especially thankful to Kunj and the DRIA team in Bengaluru for their understanding and help during the final few months of my PhD and later.

I am grateful to the Eindhoven University of Technology and in particular the Energy technology group for providing a very conducive environment for research. It would be incomplete without thanking Linda Essink for all the support that I received through my PhD. I would like to thank all my fellow colleagues in the group for the several engaging discussions that we have had. I would especially thank Ernst for all the help I received during the initial years of my PhD.

Stephen, Koondi, Jinquian: I hope that the strong friendship that I have developed with you guys during the PhD continues for my lifetime. Anwesha, Pranav, Tarun, Vishnu, Sai, Abhineet the memories that we created during the

several vacations and parties would always be cherished.

It would be impossible to conclude without thanking my family (parents, Lakshmi, Dhruv) who were always there to support me in my endeavours. I would not have been able to achieve of any of this in my life without the support and strength provided by my mother through all my times. Especially those long Skype conversations, early morning wake-up calls helped me to cope up with life away from family. I am grateful to my sister for keeping me happy with all the fun and craziness.

Valliappan Valliappan
Doha, November 2019

Curriculum Vitae

Valliappan Valliappan was born on 16-06-1990 in Madurai, India. He finished his schooling from A.V. Meiyappan higher secondary school, Chennai, India. He subsequently obtained his bachelor's degree in Aeronautical Engineering in 2011 from the Madras Institute of Technology, Chennai, India. He graduated with a Master's degree in Aerospace Engineering in 2013 from the Indian Institute of Science, Bangalore, India. In 2014 he started his PhD project in the Energy Technology group in the Department of Mechanical Engineering at the Eindhoven University of Technology. His PhD project, entitled "A numerical study on the effect of anisotropy and heterogeneity on hydraulic fractures", was supervised by prof.dr.ir. D.M.J. Smeulders, dr.ir. J.J.C. Remmers and dr.ir. A. Barnhoorn. Since February, 2019 he is employed as a researcher at Shell Technology Centre, Bangalore, India.

List of Publications

Journals

- Valliappan, V., Remmers, J. J. C., Barnhoorn, A., & Smeulders, D. M. J., A Numerical Study on the Effect of Anisotropy on Hydraulic Fractures. *Rock Mechanics and Rock Engineering*, 52(2), pp.591-609, 2019.

- Valliappan, V., Remmers, J. J. C., Barnhoorn, A., & Smeulders, D. M. J., A fully coupled hydraulic fracturing model with accurate analysis of the leak-off phenomenon in porous rocks. *International Journal for Numerical and Analytical Methods in Geomechanics*, submitted, 2019.

- Valliappan, V., Remmers, J. J. C., Barnhoorn, A., & Smeulders, D. M. J., Hydraulic fracture propagation in heterogeneous reservoirs. *Journal of Petroleum Science and Engineering*, in preparation.

Conference publications

- Valliappan, V., Remmers, J. J. C., Barnhoorn, A., & Smeulders, D. M. J., Modelling of hydraulic fracturing in an anisotropic and heterogeneous media, *6th Biot conference on poromechanics*, Paris, France, 9- 13 July 2017, pp. 2035-2040.